AN ABSTRACT OF THE THESIS OF

Amy J. Stevermer for the degree of Master of Science in Atmospheric Sciences presented on August 14, 1997.

Title: Identification of Layered Cloud Occurrences from the Lidar In-Space Technology Experiment and Advanced Very High Resolution Radiometer Imagery

Abstract Approved: Redacted for Privacy

Realistic assessment of the vertical distribution of clouds, particularly the occurrence of multi-layered systems, is critical for accurate calculations of radiative transfer in general circulation models. Such information is also useful in the design and improvement of satellite retrieval techniques. Current methods for retrieving cloud properties from satellite data assume that the clouds reside in single-layered systems. These methods are not expected to be successful for multi-layered systems.

Attempts to specifically address the question of cloud layering have thus far been limited, due in part to the difficulties of inferring vertical cloud structure from either surface or satellite data. *In situ* observations, such as those provided by aircraft, are available only for localized regions and are limited in time. This study uses data from a lidar instrument flown onboard the space shuttle and satellite imagery data to identify the frequencies of occurrence of layered cloud systems at different spatial scales over various regions of the globe.

The Lidar In-Space Technology Experiment (LITE) was flown on Space Shuttle Discovery in September 1994 and provided global-scale, high vertical resolution profiles of the earth's troposphere and lower stratosphere. Analysis of the LITE observations requires distinguishing clouds residing in organized, well-defined layers from clouds that

are distributed in altitude throughout the troposphere. The analysis employs a histogram technique in which peaks having some critical number of observations are considered to correspond to observations belonging to well-defined cloud layers.

Advanced Very High Resolution Radiometer (AVHRR) data for the 11–day duration of the LITE mission are analyzed using the spatial coherence method. This method identifies regions of locally uniform emission which are associated either with cloud-free pixels or with overcast pixels corresponding to clouds in a single layer at a well-defined altitude. The number of layers present is determined by the number of overcast radiances associated with pixel arrays exhibiting locally uniform emission within the region.

Layer statistics are compiled for the Pacific, Atlantic, and Indian Oceans and the North and South American, African, European, Asian, and Australian continents using horizontal scales of 60 and 250 km. The results indicate a strong dependence on the spatial scale chosen for the analysis, with two- and three-layered systems more prevalent at the 250–km scale. Analysis of cloud-top altitudes from LITE and AVHRR show that low-level cloud systems comprise the majority of the observations over both ocean and land.

Identification of Layered Cloud Occurrences from the Lidar In-Space Technology Experiment and Advanced Very High Resolution Radiometer Imagery

by

Amy J. Stevermer

A THESIS

submitted to

Oregon State University

in partial fulfillment of
the requirements for the
degree of

Master of Science

Presented August 14, 1997

Commencement June 1998

Master of Science thesis of Amy J. Stevermer presented on August 14, 1997

APPROVED:

Redacted for Privacy

Major Professor, representing Atmospheric Sciences

Redacted for Privacy

Dean of College of Oceanic and Atmospheric Sciences

Redacted for Privacy

Dean of Graduate School

I understand that my thesis will become part of the permanent collection of Oregon State University libraries. My signature below authorizes release of my thesis to any reader upon request.

Redacted for privacy

Amy J. Stevermer, Author

ACKNOWLEDGMENTS

Tremendous thanks to:

My advisor, Dr. James A. Coakley, Jr., for his guidance and support throughout this venture. It has been a wonderful opportunity and true privilege to work with someone so vastly knowledgeable and genuinely enthusiastic about science.

Dr. David M. Winker and NASA Langley Research Center for providing the LITE data and collaboration in this study, and to Mark A. Vaughan for his involvement in processing the lidar return signals, David Simas for the programming contributions, and John Wong for the computer support.

Fellow students, colleagues, and friends who contributed in various ways, with particular appreciation to Bill Tahnk for the many, many helpful discussions, Andy Kowalski for the good advice, and to Fu-Lung Chang and Sheila O'Keefe. Special thanks to Susan Howard, who has been a major source of support and inspiration, and to my husband, Derren Duburguet, whose patience, sacrifice, and counsel helped make this possible. I've learned an incredible amount during my time here, and it hasn't all been about clouds.

Support for this work was provided by NASA LITE NAS1–19952 and the NASA Space Grant program.

TABLE OF CONTENTS

TABLE OF CONTENTS (Continued)

LIST OF FIGURES

LIST OF FIGURES (Continued)

LIST OF FIGURES (Continued)

LIST OF TABLES

LIST OF APPENDIX FIGURES

LIST OF APPENDIX TABLES

Identification of Layered Cloud Occurrences from the Lidar In-space Technology Experiment and Advanced Very High Resolution Radiometer Imagery

Chapter 1. Introduction

1.1 Motivation

Observation shows that clouds tend to occur in distinct layers in the atmosphere. At a given location, all clouds might occur at only one altitude, indicating a single-layered system, or two or more different cloud types may occur simultaneously at different altitudes. These occurrences are referred to as multilayered cloud systems and are prevalent in frontal regions where upper-level cloud such as cirrus may overlie lower-level stratus or convective cloud. Vertically-developed systems extend upward through a large altitude range. Clouds associated with such systems tend not to be found in distinct layers but are instead considered to be distributed in altitude.

The Lidar In-space Technology Experiment (LITE) flew in 1994 and provided high resolution profiles of the earth's troposphere. These data, along with Advanced Very High Resolution Radiometer satellite imagery, are used to identify cloud systems composed of one, two, or more layers as well as those associated with clouds distributed in altitude. The frequencies of occurrence of layered cloud systems at spatial scales of 60 and 250 km are obtained from both the lidar data and the satellite imagery for comparison of the two sensing techniques as well as the results of the analysis methods. At 60 km, information on cloud layering is necessary for the improvement of satellite cloud retrieval techniques, which currently assume the presence of a single cloud layer only. At scales of

250 km, the information is relevant to the development of accurate cloud parameterizations for general circulation models.

1.1.1 Satellite Cloud Retrieval Techniques

A number of techniques have been developed to estimate cloud cover, cloud-top height, cloud optical depth, and cloud microphysical properties from satellite data. All retrievals of cloud properties depend in some way on radiative transfer calculations, most of which are based on the presence of a single cloud layer. Use of this single layer assumption is necessitated by the limited information available from satellite-measured radiances. The finite number of wavelengths sensed by current instruments do not provide adequate information for the retrieval of cloud properties even for single-layered systems, let alone for those consisting of multiple layers. The problem of retrieving cloud properties from remotely sensed data concerns the large number of unknowns as compared to the small number of measured quantities. The radiance emitted by clouds in a single layer depends on 1) the altitude of the layer, 2) the areal extent of the layer, 3) droplet microphysical structure, 4) the optical properties, single scattering albedo, and scattering phase function of the droplets or ice particles, 5) the optical thickness of the layer, 6) the three-dimensional structure of the clouds, and 7) the sun-target-satellite viewing geometry, among other things.

Radiances measured by a satellite radiometer depend on the physical properties of the clouds, aerosols, and surface, as well as on the atmospheric composition, primarily the vertical distributions of water vapor and temperature. Satellite radiance measurements are

available for only a limited number of spectral regions and are not available at every place at every time. Estimates of cloud properties, such as fractional cloud cover or cloud optical thickness, must be inferred from the limited number of observed quantities available and thus require the incorporation of some simplifying assumptions. Use of the single layer assumption is given as an example below.

For radiances emitted by a single layered cloud, the upward radiance at the top of the atmosphere is the sum of the radiances for the cloud-free portion of the field of view and the radiances for the overcast portion weighted by the fractional cloud cover. The sum is given by

$$I^{+} = (1 - A_c)B_s + A_c B_s T + A_c B_c \varepsilon \qquad (1.1)$$

where A_c is the fractional cloud cover, B_s is the radiance associated with the cloud-free portion of the region being observed and B_c is the radiance that would be observed for the overcast portion if the clouds were opaque. T represents the cloud transmissivity, and ε is the cloud emissivity.

For two-layered systems, such as cirrus cloud partially overlying a lower-level stratus layer, the top-of-the-atmosphere emitted radiance is given by

$$I^{+} = (1 - A_c)B_s + A_{cstr} B_s T_{str}[(1 - A_{ccir}) + A_{ccir} T_{ccir}] + A_{cstr} B_{str} \varepsilon_{str}[(1 - A_{ccir}) + A_{ccir} T_{cir}] + A_{ccir} B_{cir} \varepsilon_{cir}, \qquad (1.2)$$

where Term 1 represents the cloud-free emission and Term 2 corresponds to the cloud-free emission transmitted through the stratus alone and through the stratus and cirrus layers together. The third term represents emission from the stratus layer and includes contributions for both the overlapped and non-overlapped portions of the stratus deck.

Term 4 corresponds to emission from the upper-level cirrus. Here the overlap of the stratus by the cirrus is taken to be random. The total cloud cover is given by

$$A_c = A_{cstr} + A_{ccir.} \quad (1.3)$$

and the fractional region of the stratus not overlapped by the cirrus is given by $1\text{-}A_{ccir.}$

Cloud transmissivities and emissivities depend on microphysical properties such as droplet size and phase and amounts of liquid and ice water. Inference of these properties from satellite-measured radiances requires solution of a system of equations like (1.1) and (1.2). Ideally the number of measured radiances bearing independent information on cloud properties would be at least as large as the total number of unknowns. Since satellites currently operate with only a few suitable, independent channels, it becomes clear that retrieval of cloud properties for multilayered systems poses the problem of too many unknowns and too few measured parameters. For this reason, retrieval techniques currently in use are restricted to cloud residing in a single, well-defined layer.

Methods for retrieving cloud properties from satellite can be grouped into three classes, a) those using a temperature or radiance threshold to detect cloudy pixels, such as the approach taken by the International Satellite Cloud Climatology Project (ISCCP) algorithm; b) those depending on the identification of clusters or patterns in the distribution of measured radiances; and c) multispectral techniques such as those of Reynolds and Vonder Haar (1977) and Arking and Childs (1985), relying on radiance measurements at two or more wavelengths. These techniques all rely on the assumption of a single cloud layer. An assessment of the degree to which this assumption is satisfied would therefore prove useful to the development and refinement of these techniques.

1.1.2 Clouds and Climate

Cloud layer statistics should also prove useful in assessing the fidelity of parameterization schemes in general circulation models. Clouds exert a direct and significant effect on climate by reflecting shortwave radiation back to space and by emitting longwave radiation back to the earth's surface. The influence of clouds on the overall radiation budget depends on both the height and type of cloud present. Cirrus and other high clouds composed of ice crystals significantly affect the radiation budget by preventing infrared radiation from escaping to space. The high liquid water content of low-level stratus, on the other hand, can increase the cloud's albedo to near 0.90, causing a very high percentage of the incoming solar radiation to be reflected back to space and dramatically reducing the amount of solar energy incident on the earth's surface.

The net balance between the incoming solar and outgoing thermal radiation is referred to as the earth's radiation budget. In updated estimates of the global annual mean energy budget, Kiehl and Trenberth (1997) report that 22.5% or 77 W m^{-2} of the incoming solar radiation is reflected back to space by clouds, aerosols and molecular gases. Another 67 W m^{-2}, or about 20% of the total, is absorbed by the atmosphere so that only 49%, or 168 W m^{-2}, of the 342 W m^{-2} incident solar flux reaches the earth's surface. Approximately 18%, or 30 W m^{-2}, of the radiation reaching the surface is reflected back to space. The surface emits about 390 W m^{-2} of longwave radiation, 90% of which is absorbed by clouds and greenhouse gases. A significant portion of this longwave radiation, 324 W m^{-2}, is then emitted back downward to the earth's surface, and is due to

downward emission by clouds as well as emission by water vapor in the lower troposphere. The corresponding clear sky downward emittance is 278 W m^{-2}.

Numerous studies have explored contributions of shortwave reflectance and longwave emission by cloud. Cloud radiative forcing refers to the effect of clouds on the radiation balance at the top of the atmosphere. Clouds act to reduce longwave emission to space, implying an increase in the amount of radiation absorbed in cloudy regions. The global mean clear sky outgoing flux is given by Kiehl and Trenberth as 265 W m^{-2}, while the cloudy sky top of the atmosphere flux is 235 W m^{-2}. This value is obtained using a single column model with three cloud layers: a low-level layer at 1-2 km with fractional cloud cover of 49%; a midlevel layer at 5-6 km comprising 6% fractional cloud cover; and upper-level cloud at 10-11 km with fractional cloud cover of 20%. The model takes the cloud layers to be randomly overlapped, implying a total cloud cover of 62%. Combination of the shortwave and longwave contributions results in a net cooling effect on climate of -20 W m^{-2} due to clouds. Quantitative estimates of cloud radiative forcing were also obtained from the Earth Radiation Budget Experiment (ERBE) and indicate a similar net cooling effect due to clouds (Ramanathan et al., 1989). The magnitude of the cloud forcing is dependent on latitude as well as on the type of cloud present. Hartmann et al. (1992) show that while low clouds compose only 40% of the total cloud cover, they account for 60% of the cloud forcing. This is due both to their large areal extent and their high reflectivities. This effect is particularly large at mid and high latitudes where low-level marine stratus clouds are prevalent. High optically thick clouds are the largest contributors to longwave forcing, but this effect is typically offset by the very high cloud albedos. This combination of longwave and shortwave forcing can significantly perturb

the distributions of atmospheric and surface radiative heating and cooling in the earth's tropical regions.

Because of the complicated effects of clouds on the overall radiation budget, realistic parameterizations of cloud amounts and cloud properties are essential for accurate radiative transfer calculations and climate simulations. Using results from ISCCP and ERBE, Hartmann et al. (1992) show that total cloud cover is greater than 90% in high latitude stratus regimes and in Northern hemisphere storm tracks where high optically thick clouds dominate. High thin clouds are common over all regions of the globe, while mid-level thin clouds tend to occur in convective regions and mid-level thick clouds are distributed over high latitudes. One or more cloud types may contribute to the total cloud amount at a given location, particularly in high latitude and convective regions. Prediction of these multilayered cloud systems is especially difficult in climate models. Smith and Vonder Haar (1991) used Earth radiation budget observations and satellite cloud amount estimates to validate a long-term climate simulation from the National Center for Atmospheric Research Community Climate Model. Their results showed discrepancies between the model and observations for the solar component of the radiation budget, thought to be due to difficulties in the prediction and treatment of multilayered clouds and their interactions.

Techniques currently in use attempt to calculate cloud cover from other model-derived quantities, such as relative humidity (Smith, 1990). The parameterizations vary greatly and lead to considerable differences in model results. Cess et al. (1989) have provided evidence that the 3.2°C range in the surface warming predicted by climate models for a doubling of CO_2 is attributable to differences in cloud parameterization

schemes. Of particular concern is adequate simulation of cloud distribution in the vertical. Slingo et al. (1989) discuss a cloud scheme which incorporates an 11-layer atmosphere and three cloud categories: low, middle and high. Their study cites many of the difficulties encountered in such an undertaking and compares model results with satellite measurements. Their results show improved agreement over earlier techniques for the longwave part of spectrum, although emission at high latitudes for both hemispheres tends to be underestimated. For the shortwave part of the spectrum, the United Kingdom Meteorological Office model used by Slingo et al. shows albedo maxima in the stratocumulus regimes, although the meridional extent is smaller than that indicated by observations. High latitude albedos tend to be large, indicative of excessive cloud cover poleward of 50°. These errors at high latitudes have a strong effect on the global mean values, resulting in an annual mean longwave emission that is 11.6 W m^{-2} less than ERBE values and a mean albedo of 33.0%, which is larger than the observed value of 30.2%. Predictions of climate are thus highly sensitive to radiative interactions and require the best possible simulations of cloud type and distribution.

1.2 Background: Evidence of Cloud Layering

Despite the importance of vertical cloud distribution to accurate calculations of radiative heating, relatively few observational studies have been undertaken. Hahn et al. (1982 and 1984) used conditional probabilities and area-weighted averages of surface and ship observations to estimate the co-occurrence of 27 cloud types grouped into 6 major categories. Using 14 days of observations at a 5°-latitude × 5°-longitude resolution, their

time-averaged results show a very high coincidence between the occurrence of high clouds like cirrus, cirrostratus or cirrocumulus and mid-level clouds such as cumulus, cumulonimbus, altostratus or altocumulus. The likelihood of stratus or cirrostratus layers co-occurring with nimbostratus was also high, on the order of 60-70% over the world's continents. Multiple cloud layers are especially likely to occur in midlatitude frontal zones, where high clouds such as cirrus immediately precede a warm front, and low or mid-level stratus mark the advance of a front.

The U.S. Air Force Three-Dimensional Nephanalysis, begun in 1972, combined surface, aircraft, and satellite data to provide observations of total cloud cover, base and top heights, and cloud type and amount at 15 vertical levels. Tian and Curry (1989) analyzed this 3DNEPH data for a two-week period in January 1979. At a 45-km grid size for a region of the North Atlantic Ocean from 40 to 60°N and 10 to 50°W, the frequency of occurrence of single-layered systems was found to be 56.1%, with two-layered systems occurring 24.3% of the time. Three cloud layers were reported 7.9% of the time, and the occurrence of more than three layers was found to be only 0.5%.

The studies by Tian and Curry as well as by Hahn et al. illustrate the prevalence of multilevel cloud systems in surface observations. Due to the unavailability of data for many parts of the globe and the difficulty of determining high and middle cloud amounts in the presence of low-level layers, surface observations can provide only limited information at the levels of cloud occurrence. Wang and Rossow (1995) analyzed one year (June 1983 - July 1984) of upper-air sounding for 30 sites, primarily in the North Pacific and North Atlantic Oceans. The rawinsonde observations provide a vertical resolution of 50 mb near the surface and 10 mb in the upper atmosphere, and correspond to a horizontal

distance of 10 to 30 km. For cloudy situations, single-level clouds were reported approximately 20% of the time, while multilayered systems were present in 56% of the observations. Multilayered clouds tended to be most prevalent in the tropics, with two-layered systems comprising the majority of the observations.

With the return of the first TIROS-1 images in 1960, satellite technology became an important tool in the study of global cloud patterns. Measurements from space can pick out high clouds often missed in surface reports, and provide day and night observations over the entire globe. And yet, assessment of multilayered cloud systems from satellite observations remains a difficult problem (Baum et al., 1994; Coakley, 1983; Stone et al., 1994; Baum and Wielicki, 1994; Rossow and Schiffer, 1991).

Analysis of NOAA-7 Advanced Very High Resolution Radiometer data by Coakley and Baldwin (1984) found that layered systems account for a significant portion of the overall cloud cover over the Pacific Basin. The time-averaged likelihoods from three days and nights of observations at a $(250\ km)^2$ scale were approximately 25-40% for single-layered systems, 20-30% for two-layered systems, and 15-35% for three-layered systems.

Other attempts to discern multilayered cloud from satellite include Jin and Rossow's (1997) analysis of multispectral High Resolution Infrared Radiation Sounder (HIRS) data. Studies of the global cloudiness distribution on a $2.5° \times 2.5°$ latitude/longitude grid show frequencies of two-layer cloudiness of 16.9 percent over land and 25.5 percent over ocean for July 1989. For January 1990, the frequencies of two-layer occurrences are 12.4 percent over land and 20.4 percent over ocean. Such studies support the results of surface observations and indicate that multilayered cloud systems

occur relatively frequently and will be an essential component in the determination of cloud properties and cloud radiative effects.

1.3 Description of Present Study

Data from the Lidar In-space Technology Experiment along with Advanced Very High Resolution Radiometer imagery are used to obtain quantitative assessments of layer statistics for the entire globe between 50°S and 50°N. Such an analysis is warranted by the lack of any focused studies of the occurrence of cloud layering for more than a single region and by the importance of such information to improved satellite retrieval methods and treatment of clouds in general circulation models.

Lidar measurements offer very high vertical resolution profiles of the earth's troposphere and lower stratosphere, allowing identification of optically thin or underlying cloud layers typically missed by passive sensors. The data are analyzed by identifying peaks in the frequency distribution of cloud-top altitudes corresponding to distinct cloud layers. The global-scale observations provide an unprecedented data set with which to compare results obtained from satellite retrieval methods.

AVHRR imagery for the 11 days corresponding to the LITE mission provides a global data set for comparison with the lidar data. Cloud layer statistics are computed from the results of spatial coherence analysis, which identifies pixel arrays with low standard deviations in their emitted radiances as either cloud-free or belonging to distinct cloud layers. This method differs from the ISCCP algorithm, which does not assume that clouds reside in layers but instead considers all pixels that pass a radiance threshold test to

correspond to cloud. The spatial coherence method has been shown to be especially adept at identifying multiple cloud layers (Coakley, 1983). Detailed descriptions of the lidar and satellite analysis techniques follow in Chapters 2 and 3.

Chapter 2. Analysis of Lidar Data

2.1 LITE Instrumentation and Data

The LITE instrument is a direct detection lidar system consisting of a laser transmitter module, receiving telescope and aft optics assembly, instrument controller, data handling units, and other electronic subsystems mounted on a 3-m pallet. A complete description is provided by Winker et al. (1996) and McCormick et al. (1993). The primary components are the transmitter and receiver. The transmitter consists of two Neodymium:YAG (yttrium aluminium garnet) lasers with a fundamental wavelength of 1064 nm. Only one laser can be operated at a time; the second is for redundancy. Incorporation of doubling and tripling crystals allows conversion of the beam to second and third harmonics at 532 and 355 nm and provides simultaneous output at the three wavelengths. The receiver includes a Ritchey-Cretien telescope and support structure surrounding an aft optics area. The 38-inch diameter primary mirror of the telescope collects the laser light backscattered by the atmosphere and directs it into the optics assembly. Here the backscattered light is separated into its three colors, with the 1064 nm beam directed to an avalanche photodiode and the 355 nm and 532 nm beams routed to photomultiplier tubes. Also included in this assembly is the aperture wheel used to reconfigure the instrument for either day (beam diameter of 1.1 mrad) or night (3.5 mrad) operation.

The lidar instrument was flown aboard Space Shuttle *Discovery* (STS-64), launched at 22:22 GMT on September 9, 1994. This late afternoon launch near the

equinox in combination with a 57° orbital inclination placed the terminator crossings near the northern and southern turning points to maximize nighttime latitudinal coverage. Orbit ground tracks for which high gain cloud return data were available for this analysis are shown in Figure 2.1. Table 2.1 summarizes the number of independent passes and total days of observations for each latitude zone within each of the ocean regions. The shuttle was flown at an altitude of 260 km until the last few days of the mission when the altitude was decreased to 240 km. Given an orbital altitude of 260 km, the corresponding instrument footprint at 1.1 mrad is 290 m for the 1064 nm beam. Accounting for the 7.4 km sec^{-1} orbital velocity and 10 shot per second sampling rate, the distance between two consecutive laser footprints is 740 m, defining the horizontal resolution of the instrument.

Lidar is an acronym for "light detection and ranging" and can be thought of as the optical analogue of radar. The high frequency laser pulses generated by the transmitter travel through the atmosphere until coming into contact with a scattering surface, such as a cloud droplet, aerosol particle, or the ground. The beam is backscattered to the instrument and collected by the receiver. The range, corresponding to the altitude of the scattering object, is determined by the time of the return. The amount of power backscattered to the receiver depends on the size and shape of the object responsible for the scattering. This dependence is described by the backscattering cross section of the object. The cross section is the area that the object presents to the beam and is proportional to the amount of energy removed from the original beam as a result of the backscattering by the object.

Molecular scattering cross sections are inversely proportional to the fourth power of the wavelength. For aerosols, the scattering cross-sections fall off as $1/\lambda$ and for cloud

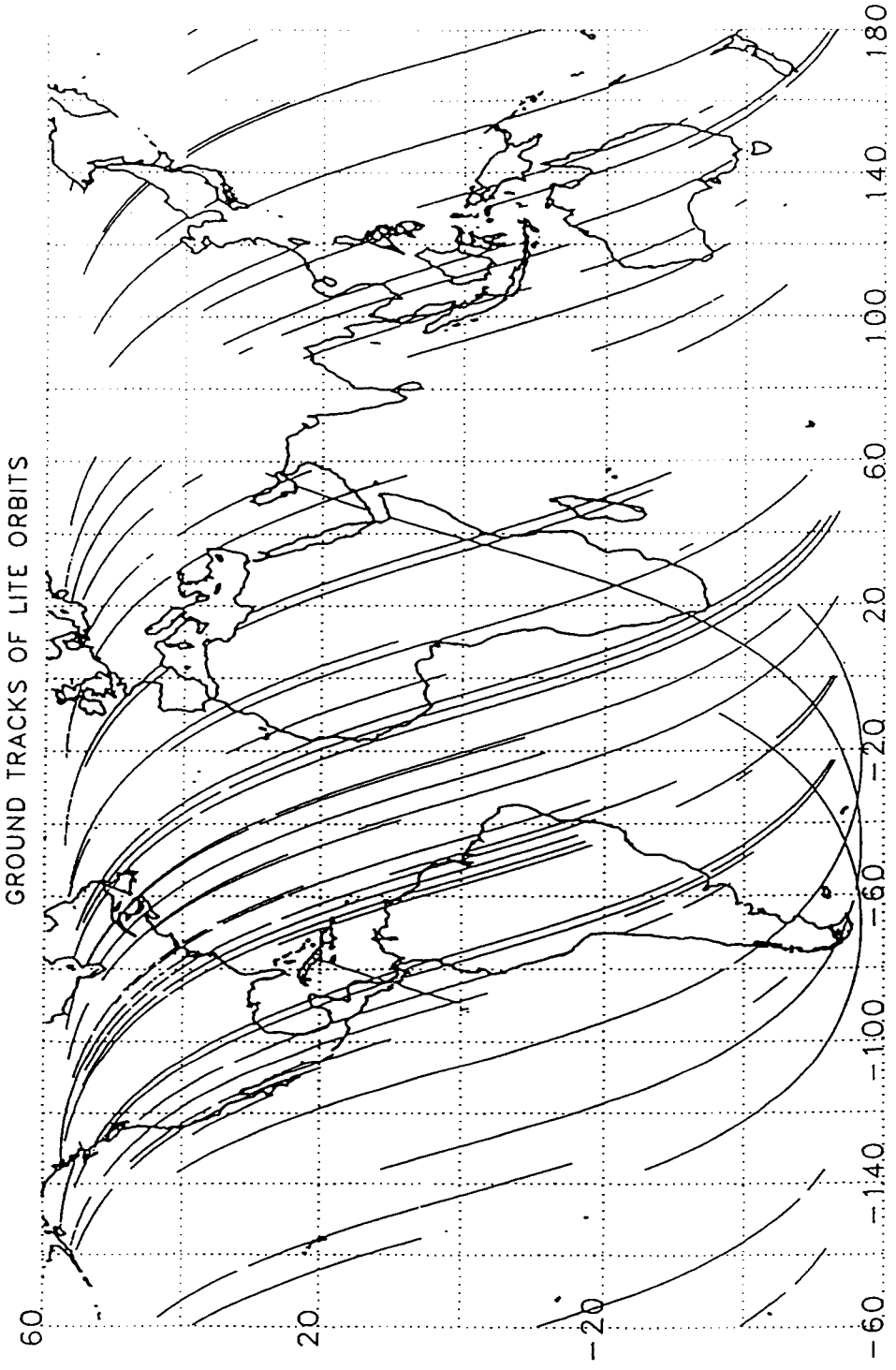

Figure 2.1 Orbit ground tracks corresponding to high gain cloud return data for LITE mission.

Region		Days	Indpt. Passes
Pacific Ocean	25 - 50 N	7	12
	0 - 25 N	7	14
	0 - 25 S	5	9
	25 - 50 S	4	9
Atlantic Ocean	25 - 50 N	6	21
	0 - 25 N	5	14
	0 - 25 S	5	9
	25 - 50 S	5	14
Indian Ocean		6	13
North & South America		6	20
Africa/Europe		5	13
Asia		3	8
Australia		5	5

Table 2.1 LITE coverage by geographic and latitude region over duration of mission.

droplets the scattering cross-sections are nearly independent of wavelength. Consequently, the 355-nm channel provides the largest return signal from high altitudes but experiences the greatest attenuation for lower altitudes. Penetration to lower altitudes is best achieved at the longer 532 and 1064-nm wavelengths where both molecular and aerosol scattering effects are a minimum.

Attenuation of a beam of light is a result of both scattering and absorption, thus both the scattering cross-section and absorption cross-section of an object must be considered. The sum of these cross-sections is termed the extinction cross-section. When multiplied by the particle number density, the result is an extinction coefficient which has units of inverse length. This coefficient represents the fraction of the area of the incident beam blocked per unit length of the medium.

Cloud droplets and ice particles interact strongly with the beam. Because ice and water are nonabsorbing at the wavelengths of observation and because droplet and particle sizes are much greater than the wavelengths of interest, their interactions with the beam are independent of wavelength. Atmospheric aerosols have radii on the order of 0.1 to 1 μm, which are comparable with the wavelengths of the LITE instrument. Their interactions with the beam are expected to depend on the wavelength of the radiation. Although the aerosol cross-sections are small relative to cloud droplets, they are still large enough and the aerosol concentrations are likewise sufficient to cause noticeable interaction with the beam.

2.2 Derivation of the Basic Lidar Equation

Consider a sample of cloud particles with a size spectrum given by

$$\frac{dn(r)}{dr} \qquad (2.1)$$

where r is the droplet radius and $n(r)$ describes the number of particles per unit volume ranging in size from r_1 to r_2. The total number of particles per unit volume is given by

$$N = \int_{r_1}^{r_2} \frac{dn(r)}{dr} dr . \qquad (2.2)$$

Using σ_s to denote the scattering cross section, the volume scattering coefficient is given by

$$\beta_s = \int_{r_1}^{r_2} \sigma_s(r) \frac{dn(r)}{dr} dr . \qquad (2.3)$$

Dividing the volume scattering coefficient by the particle number density, N, gives an average scattering cross section, $\overline{\sigma_s}$, for the sample. Define the range, R, as the distance from the lidar at which the scattering takes place and A_r as the area of the collecting aperture. The basic lidar equation provides an expression for the averaged backscattered power, given by Liou (1980) as

$$\overline{P} = P_t \frac{A_r}{R^2} \frac{P(180°)}{4\pi} \beta_s(\frac{\Delta h}{2}) \exp\left[-2\int_0^R \beta_e(R')dR'\right], \qquad (2.4)$$

where Δh is the pulse length transmitted into the medium by the lidar instrument and $\beta_s(\frac{\Delta h}{2})$ denotes the average attenuation due to backscattering based on the single scattering approximation. This approximation assumes that the attenuation is proportional to the distance into the medium. P_t in the above equation indicates the transmitted power,

$P(180°)$ denotes the phase function describing the fraction of radiation backscattered and β_e is the volume extinction coefficient outside of the cloud and includes effects due to both scattering and absorption. The exponential term in the above equation represents the attenuation of the pulse energy according to the Beer-Bouguer-Lambert law, which states that the radiant energy traversing a medium will decrease exponentially according to the integral of the extinction coefficient over the length of the medium.

2.3 Determination of Return Altitudes

The strength of the backscattered signal can be used to differentiate between Mie scattering in cloud or aerosol layers and scattering by gas molecules. The time of the return is used to estimate the altitude of the scattering object, which in the case of clouds provides an estimate of the cloud-top height. The backscattered signal of a lidar system falls off as the square of the range through the gaseous atmosphere for both surface-based and spaceborne observations. Cloud-top altitudes can be determined by monitoring the rate of change of the return signal with distance. For a surface-based lidar system, the return signal will decrease exponentially with altitude due to the decrease in atmospheric density. Cloud droplets enhance the amount of the beam backscattered to the receiver, resulting in an increase in the return signal relative to that from the gaseous atmosphere. The position at which the rate of change of signal with distance from the lidar first changes sign from negative to positive marks the boundary between clear air and cloud. In the case of LITE, atmospheric density increases as the signal penetrates to lower levels. The boundary between clear air and cloud is marked by an increase in the slope of the return

signal profile as the strongly scattering cloud is encountered. Figure 2.1 shows simulated backscatter profiles for surface and space-borne lidar systems. The boundaries between clear air and cloud can be easily distinguished.

Providing the optical attenuation of the cloud is not too large, the lidar beam will completely penetrate the cloud layer. Signal returns measured from beneath the cloud are the result of Rayleigh scattering by gas molecules, scattering by aerosols, and scattering by droplets and particles in lower-level cloud systems.

Return signals for the LITE mission are processed at NASA Langley Research Center in cooperation with Dr. David M. Winker. For each set of 10 consecutive laser firings, the maximum and minimum cloud altitudes, and mean, standard deviation, uniformity and porosity of the 10 shots are retained. In some cases, a surface flag corresponding to cloud-free returns is included; for others, the fraction of shots containing cloud is retained. These composites represent a temporal resolution of 1 second and spatial resolution of 7.4 km.

2.4 Analysis of Altitude Observations

Cloud layer information is extracted from the LITE data using the composite data described above. Frequency distributions of the composite observations are calculated for each 1000-km orbital segment using a fixed bin size of 0.5 km over a range of 0-18 km. The size of the bins is driven by the total number and range of the observations. The 0.5-km bin size was found to be just large enough to account for the variability in the 10-shot composite observations, but not so large as to result in cloud layers being combined into

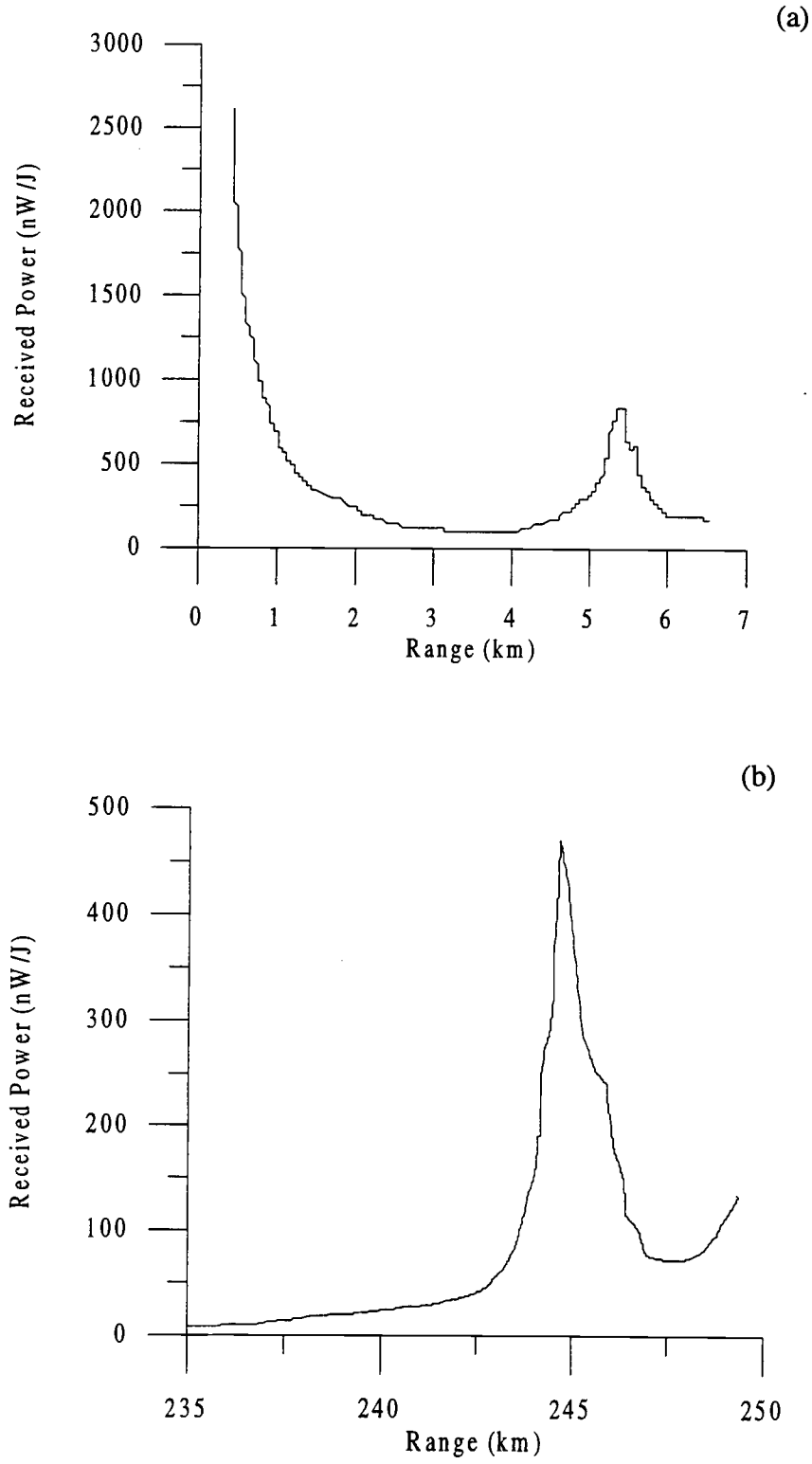

Figure 2.2 Simulated 0.532-μm lidar backscatter profiles for altocumulus cloud observed by (a) surface-based lidar and (b) shuttle-borne lidar. Based on Platt et al., 1993.

"blocks" of cloud spanning several kilometers in altitude. Smaller bin sizes resulted in too-few observations per bin and for low-level cloud led to a relatively uniform distribution of observations across consecutive bins.

Cloud layers can be identified by isolating multiple observations occurring at similar altitudes from the remaining observations scattered less densely over the entire range of altitudes. The null hypothesis assumes that clouds are distributed randomly and uniformly in altitude without any distinct layering structure. Observations belonging to a single cloud layer are considered to be normally distributed within a given altitude interval on the frequency distribution plot. The mean and standard deviation of the observations within this interval are $\bar{x}$ and σ, respectively.

Each peak in the frequency distribution of the N points is tested for significance as follows. First, the bin containing the peak and the adjacent bins on either side of the peak are taken as an initial, trial estimate of the domain spanned by the peak. The actual domain of the peak is the 4σ-interval over which 95% of the points in the normal distribution representing the peak would be located, given by $x_1 \leq \bar{x} - 2\sigma$ and $x_2 \geq \bar{x} + 2\sigma$. If the limits of the domain fail to satisfy

$$x_2 - x_1 \geq 4\sigma, \qquad (2.5)$$

or if the number of points in this domain is less than 10, then the trial domain is expanded by adding to the domain the next adjacent bin containing the largest number of points, as long as the number of points in the adjacent bin is not larger than that found in the peak itself. If the bins on either side of the trial domain contain the same number of points, then both bins are added to the domain. Adjacent bins are added sequentially until 1) a bin is

encountered that has a larger number of points than are in the peak, 2) the domain for the peak equals the entire domain L, or 3) the condition above is satisfied.

If (2.5) is satisified, the domain is further expanded until a new domain satisfying

$$x_2' - x_1' \geq 8\sigma \qquad (2.6)$$

is found. As before, if a bin with a number of points greater than that in the peak is encountered, then the test for the particular peak is stopped. Once the second domain is established, the number of points m within the first domain $[x_1,x_2]$ and the number of points n within the second domain, $[x_1',x_2']$, are used to calculate the number of points p in the normal distribution used to represent the peak, and the number of points q corresponding to the uniformily distributed background noise within the larger of the two domains. Values for p and q are obtained by solving

$$m = 0.95p + \frac{l}{k}q \qquad (2.7)$$

and

$$n = p + q \qquad (2.8)$$

where l is number of bins in the $\pm 2\sigma$ domain, and k is number of bins corresponding to the $\pm 4\sigma$ domain. Ninety-five percent of the points in the normal distribution are assumed to fall within $\pm 2\sigma$ of the mean and nearly all the points fall within $\pm 4\sigma$. For a peak to be significant, both p and q must be greater than zero and

$$m \geq \frac{l}{k}q + 3\sigma_v. \qquad (2.9)$$

Here σ_υ is the standard deviation of the number of points expected to be found in the $[x_1,x_2]$ domain, if the q points are randomly and uniformly distributed over all the bins within the larger domain $[x_1',x_2']$. The standard deviation is given by

$$\sigma_\upsilon = \frac{1}{k}\sqrt{\frac{q(k-1)}{l}}. \qquad (2.10)$$

Figure 2.3a-d shows the frequency distributions of altitudes for four 1000-km orbital segments over the Atlantic Ocean, each corresponding to a total of approximately 135 single-second composites. The marked bins indicate peaks which passed the significance test described above and are taken to correspond to observations belonging to distinct cloud layers. The altitude observations comprising the distribution are shown in Figure 2.2e-h, with composited returns belonging to the identified layers indicated by symbols. The altitude interval and observations associated with each significant peak at the 1000 km scale are retained and used to identify cloud layers present within 60 and 250 km regions.

Measurements of cloud-top altitudes below 100 m are taken to correspond to surface clutter or ground haze and are removed from this analysis. These observations are counted as cloud-free. Cloud-free or overcast observations can also be identified from the surface flag, indicating the lowermost return for the 10-shot composite. A surface flag of 0 indicates that there was no penetration to lower levels and the observation is considered to be overcast. A surface flag of 1 indicates a surface return and the observation is considered to be cloud-free since the maximum return altitude is below the 100-m cut-off. Allowable values of the surface flag are summarized in Table 2.2. A region is defined as overcast or cloud-free if at least 90% of the observations for that region are overcast or

cloud-free. Layered cloud systems within 60-km and 250-km scales are identified from the layer counts and altitude information retained from the analysis of the 1000-km orbital segments. Observations at the 60- and 250-km scales that do not correspond to any of the layers isolated at the 1000-km scale represent contributions of local phenomena that are classified as unidentified cloud. Such returns typically occur at mid to upper levels. The layer categories for the LITE observations are the same as those defined for the AVHRR data, shown in Table 3.1.

Surface Flag	Indicates
0	Completely attenuating cloud; failure to reach surface
1	The maximum altitude corresponds to a surface return
2	a low-lying cloud with base indistinguishable from the surface
3	Otherwise

Table 2.2 Values of surface flag for LITE returns.

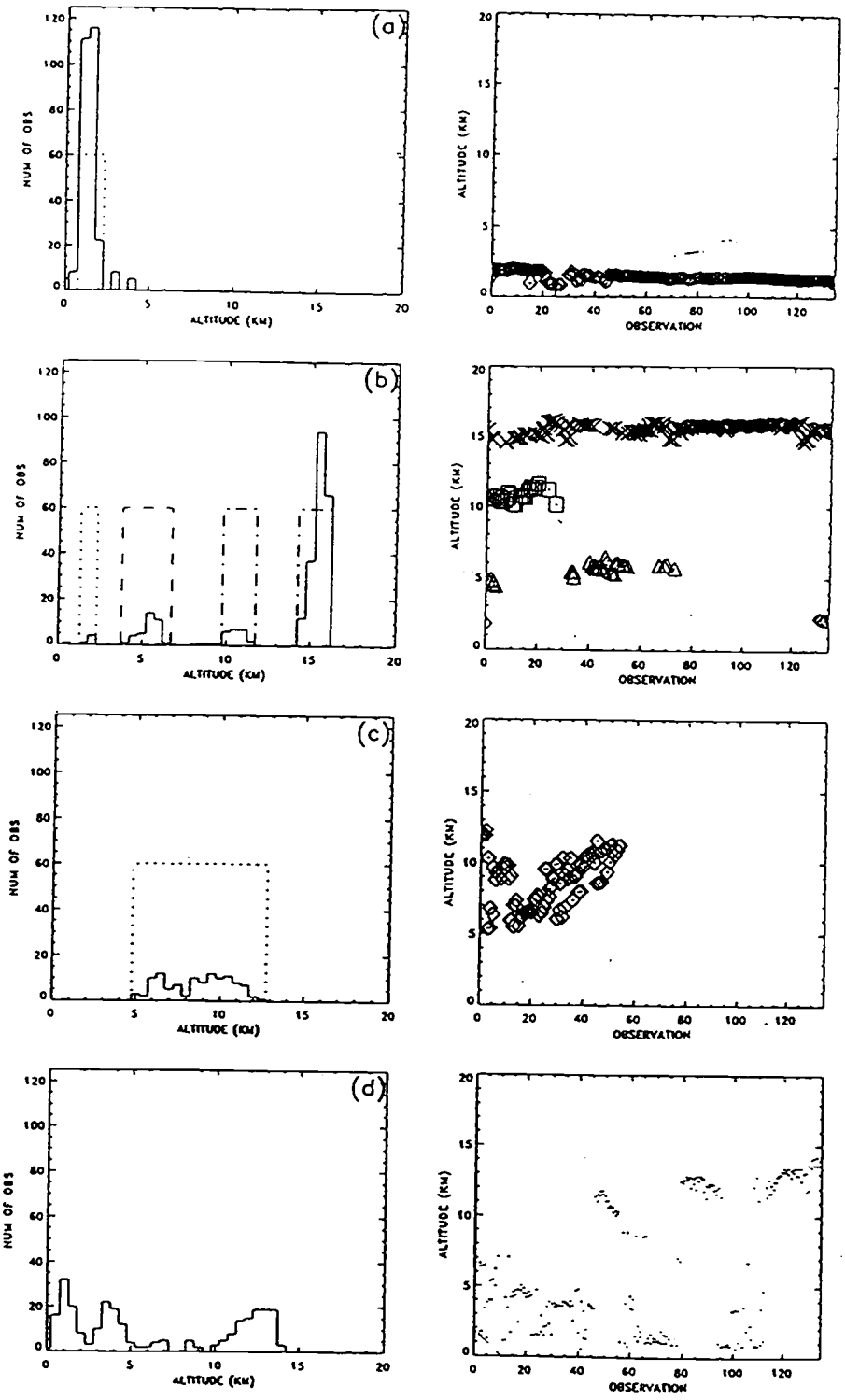

Figure 2.3 Frequency distributions and lidar cloud altitudes for four 1000-km orbital segments over the Atlantic Ocean: (a) single cloud layer, (b) multiple cloud layers, (c) clouds distributed in altitude but identified as a distinct layer, (d) clouds distributed in altitude with no layers identified.

Chapter 3. Analysis of AVHRR Data

3.1 AVHRR Instrumentation and Data

The NOAA-12 Advanced Very High Resolution Radiometer (AVHRR) is a scanning radiometer operating with channels for reflected sunlight at 0.63 μm and 0.89 μm, a near-infrared channel at 3.7 μm, and infrared channels at 11 and 12 μm. The instrument consists of an elliptical scan mirror, rotating continuously at 12π rad/sec or 360 rev/min. Scenes are sampled at a 40-kHz rate, equivalent to 1 pixel/25 μs, along a scan line +/- 55.4° from nadir. The AVHRR travels aboard NOAA's polar-orbiting satellites at an altitude of approximately 850 km and has a field of view of 1.3 +/- 0.1 mrad, corresponding to a scan spot size of $(1.1\ \text{km})^2$ at nadir. The satellite samples 2048 spots along a 110.8° path. Because of the change in viewing angle, pixels at the limb of the scan have a size closer to 6.4 km × 2.3 km.

AVHRR global area coverage (GAC) data is constructed from the $(1.1\ \text{km})^2$ resolution data as described by Schwalb (1978). Along a scan line, the average radiance is computed from four scan spots, then a scan spot is skipped. The next two scan lines are skipped, and the process is repeated on the fourth scan line. The result is a subsatellite point resolution of approximately 5 km × 3 km. Because 15 km^2 is approximately equal to $(4\ \text{km})^2$, the resolution of GAC data is usually described as 4 km. The spatial coherence method of cloud retrieval discussed in the next section makes use primarily of 11-μm (Channel 4) radiance measurements. NOAA specifications for channels 3-5 require the equivalent blackbody temperature of a 300 K scene to be determined to within ± 0.12 K

(Kidder and VonderHaar, 1995), equivalent to a radiance error of 0.2 mW m^{-2} sr^{-1} cm at 11 μm.

3.2 Spatial Coherence Analysis

NOAA-12 AVHRR GAC data for the days corresponding to the LITE mission are analyzed using the spatial coherence method (Coakley and Bretherton, 1982; Coakley and Baldwin, 1984). Based on the assumption that clouds reside in distinct well-defined layers and that clouds are optically thick at infrared wavelengths, this automated procedure uses the statistical properties of radiances for small (8 km)^2 regions, corresponding to 2 × 2 arrays of 4-km GAC pixels, to determine cloud amount and height within regions approximatey (60 km)^2 and (250 km)^2 in size. The method is expected to identify overcast and cloud-free pixels provided layered clouds and cloud-free portions of a scene extend over several adjacent pixels.

The first pass of spatial coherence processing uses a rudimentary pattern recognition scheme to analyze the means and standard deviations of the emitted radiances for the 2 × 2 pixel arrays. The means and standard deviations of the 11-μm infrared radiances for 1024 2 × 2 arrays of 4-km GAC pixels are calculated for each ~(250 km)^2 region. Pixel arrays having low standard deviations are regions of locally uniform emission and are considered to be either cloud-free or overcast by layered clouds. If all of the overcast pixels in a region exhibit the same 11-μm emission, and if the emitted radiances for the overcast and cloud-free pixels bound the range of radiances for the region, then the region is presumed to have one cloud layer. Mean radiances falling

between these cloud-free and overcast values are considered to correspond to pixels only partially covered by a single-layered cloud system. For each $(250\ km)^2$ frame, a frequency distribution of the radiances is constructed, with the bin interval determined according to the radiances expected for low-level cloud systems and dependent on whether the background is land or ocean. A standard deviation cutoff, also determined by the land or ocean background, is applied to the pixel arrays and a frequency histogram is formed representing the radiances associated with the pixels that exhibit locally uniform emission. Peaks of this distribution represent areas of locally uniform emission and correspond to the feet of the arches of a spatial coherence plot. One such plot, which shows the local standard deviations plotted against the local means, is shown in Figure 3.1. The warmest of the feet represents a potentially cloud-free radiance; other feet correspond to contributions from overcast cloud layers. Locations of the pixel-scale arrays belonging to the feet of an arch are retained and results are written to binary file as an array containing the latitude and longitude, and mean, cloud-free, overcast, and 10th and 90th percentile radiances for $(60\ km)^2$ subframes composed of 16 scan lines $\times$ 16 scan spots of GAC data.

Compositing several days of first pass results for a region allows reliable estimation of cloud-free radiances. This "clear-sky" climatology can then be incorporated into the second pass processing to assure that pixels belonging to subframes in which there are no cloud-free pixels are properly identified as overcast, and not as cloud-free.

Determination of the cloud-free radiances, fractional cloud cover, and cloud properties is completed during second pass processing. This step of the analysis combines instantaneous cloud-free estimates for $(60\ km)^2$ subframe regions with the cloud-free radiance climatology. Cloud-free radiances are classified at the $(250\ km)^2$ frame scale.

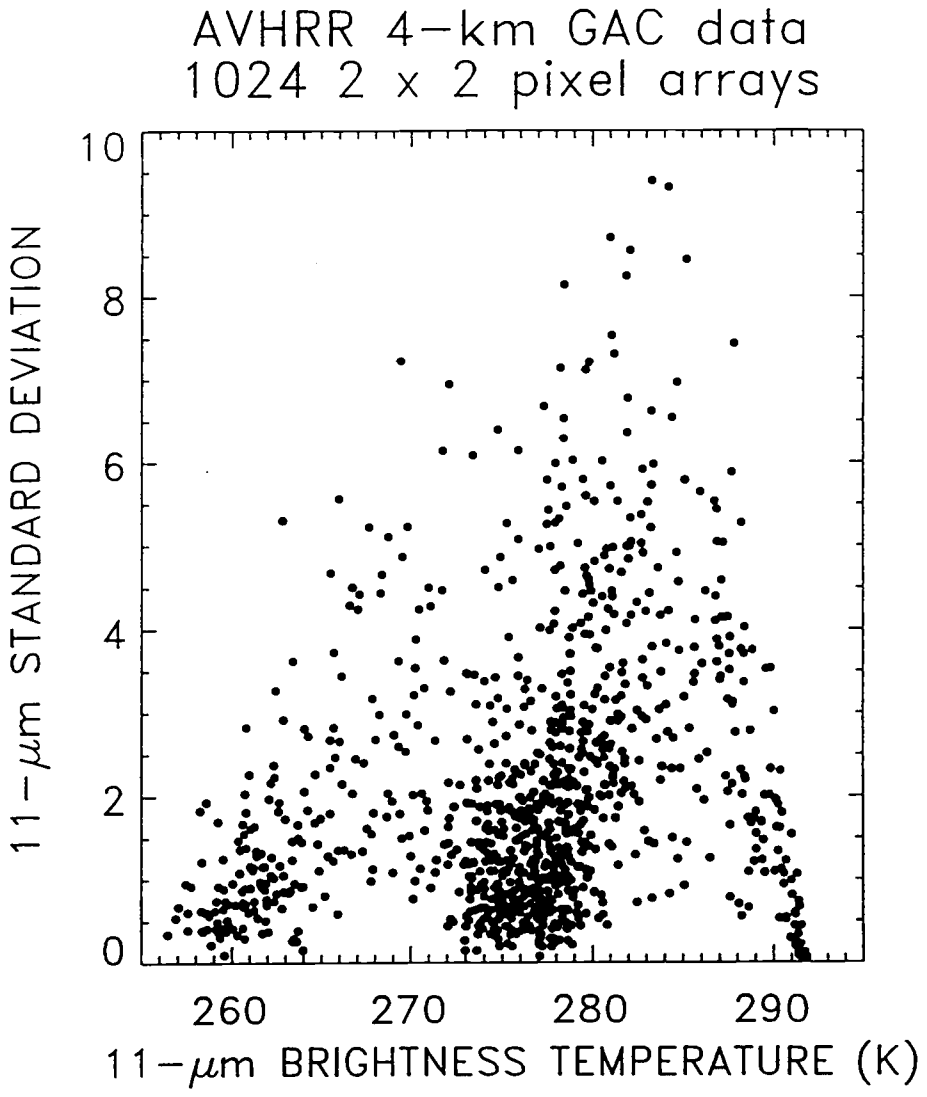

Figure 3.1 Spatial coherence plot for multilayered cloud system over the Pacific Ocean (21.5°S, 176°E; Sept. 11,1994).

Cloud-free radiances for the subframe scale are compared with that of the frame scale to assure consistency. Retrievals of cloud cover information proceed by assuming that the emitted radiance for each pixel is linearly proportional to the cloud cover of that pixel.

For a single cloud layer, the pixel radiance I for a partially filled field of view can be written as

$$I = (1-A_c)B_s + A_cB_c, \qquad (3.1)$$

where A_c is the fractional cloud cover, B_s is the radiance for the cloud-free portion, and B_c is the radiance for the overcast portion. Both B_c and B_s are estimated from the pixels corresponding to the 11-μm arch feet. Inversion of this equation allows estimation of the fractional cloud cover, given by

$$A_c = \frac{I - B_s}{B_c - B_s}, \qquad (3.2)$$

where A_c is the "effective" cloud cover, equal to the product of the emissivity and the fractional area that is overcast. Results include computations of total cloud cover for each $(60\ \text{km})^2$ region as well as composite estimates of cloud cover for each $(250\ \text{km})^2$ frame.

3.3 Computation of Layer Statistics

Layer statistics are compiled for various regions of the globe for $(60\ \text{km})^2$ subframes and for 2.5° latitude × 2.5° longitude frames within 50°S to 50°N. Layer statistics are computed for each 10°-latitude belt over the same area. Regions analyzed include the Pacific, Atlantic, and Indian Oceans as well as areas corresponding to the African, Asian, European, North American and South American continents. One day of satellite coverage for each of these areas is shown in Figure 3.2.

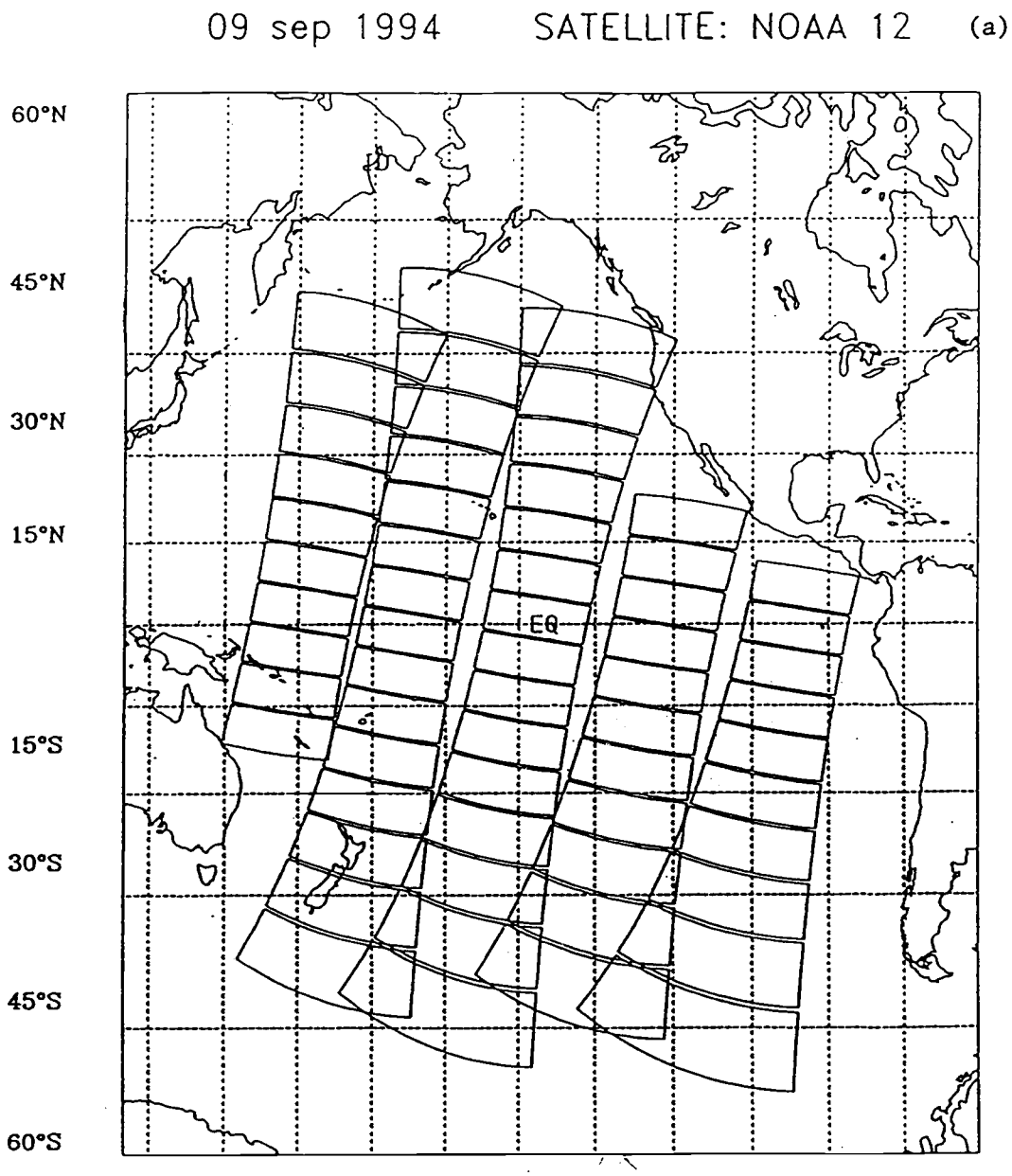

Figure 3.2 Examples of daily satellite coverage for (a) Pacific Ocean, (b) Atlantic Ocean, (c) Indian Ocean, (d) North and South America, and (e) Africa, Europe, and Asia.

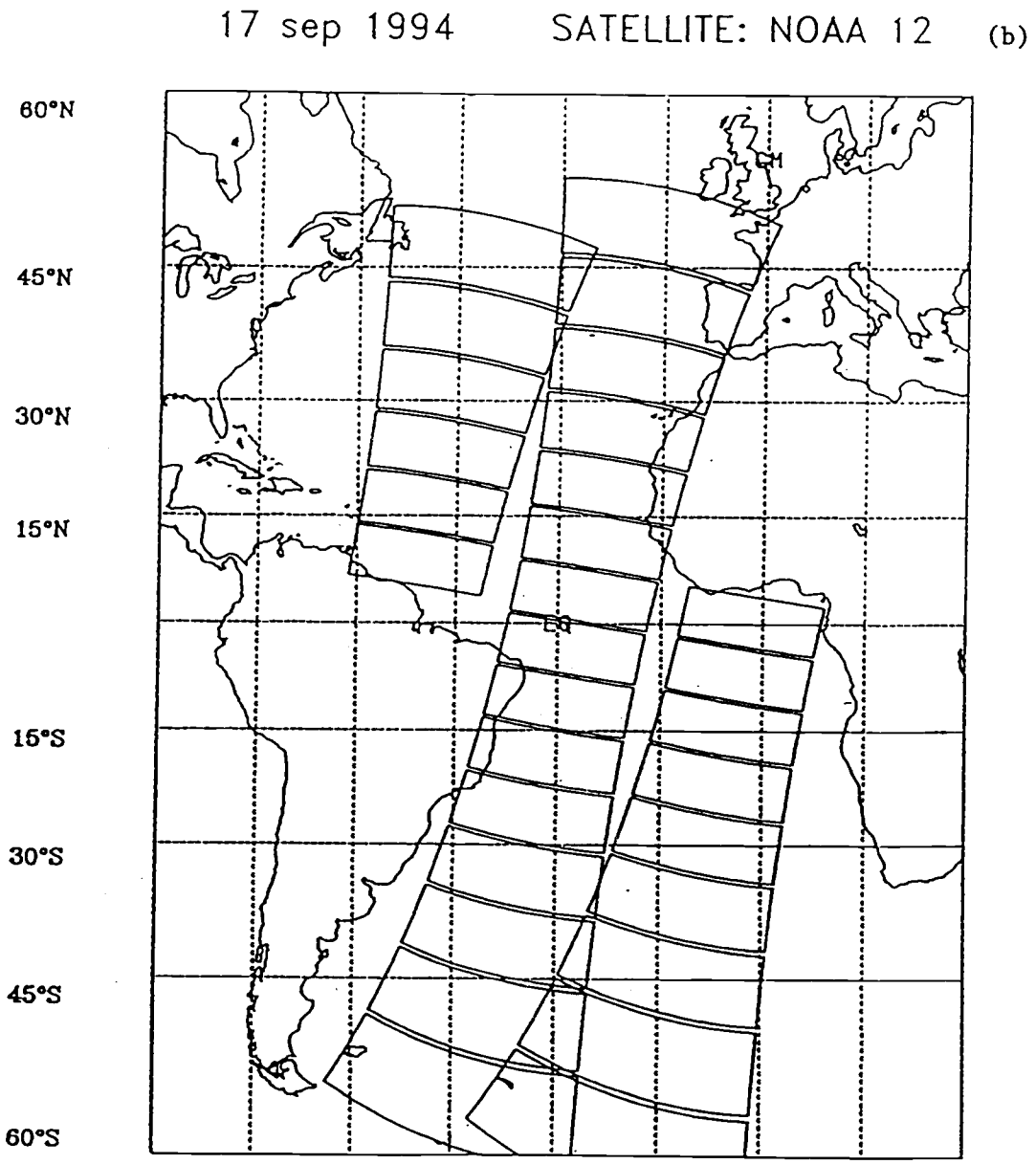
17 sep 1994 SATELLITE: NOAA 12 (b)
60°N
45°N
30°N
15°N
EQ
15°S
30°S
45°S
60°S

11 sep 1994 SATELLITE: NOAA 12 (c)

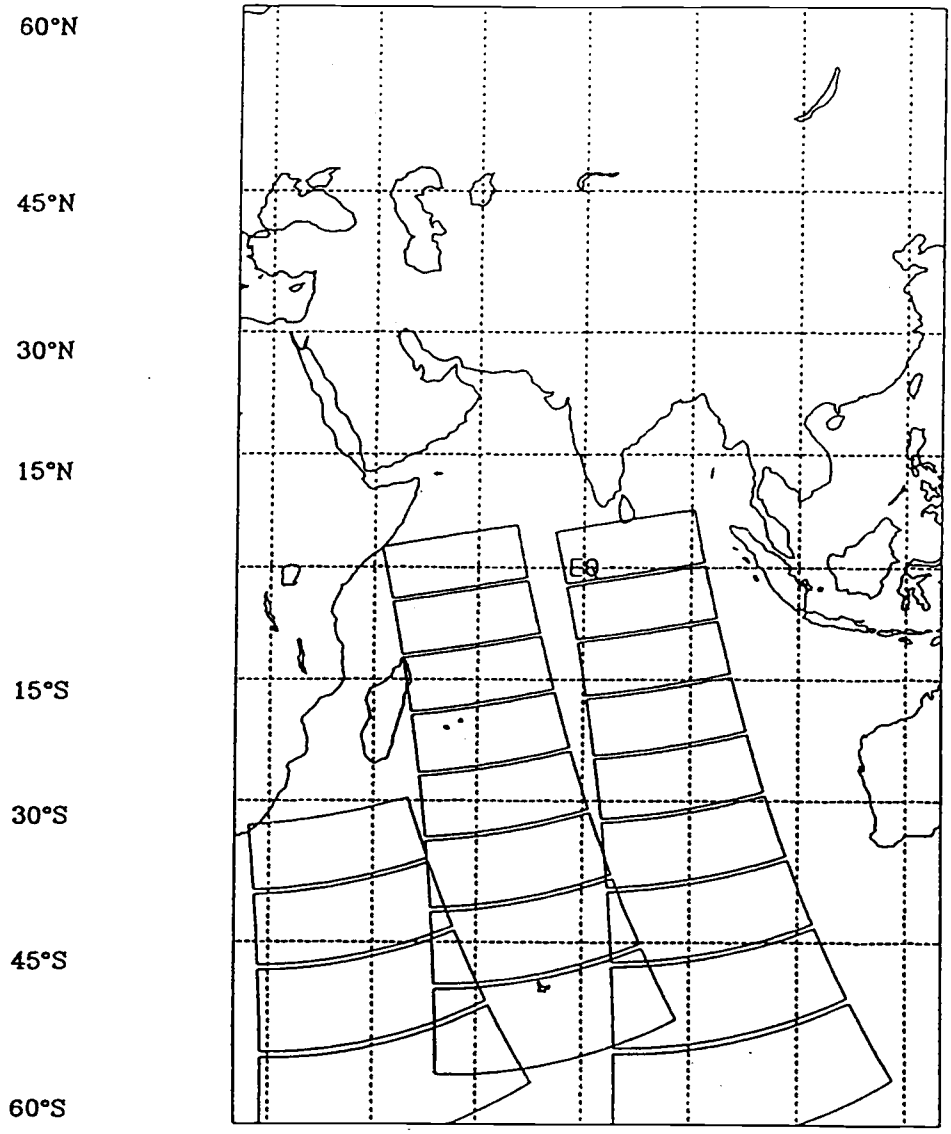

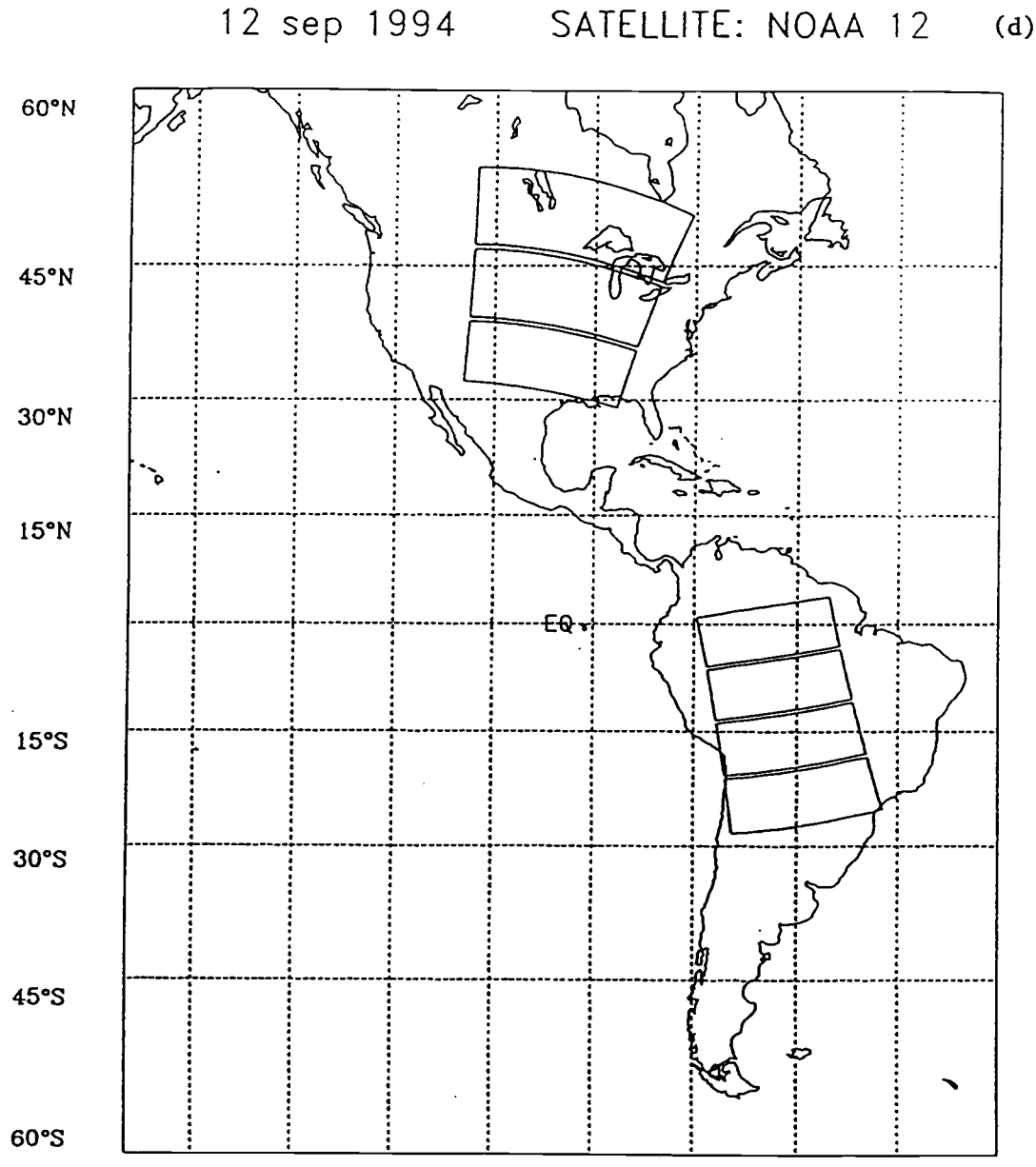
12 sep 1994 SATELLITE: NOAA 12 (d)
60°N
45°N
30°N
15°N
EQ
15°S
30°S
45°S
60°S

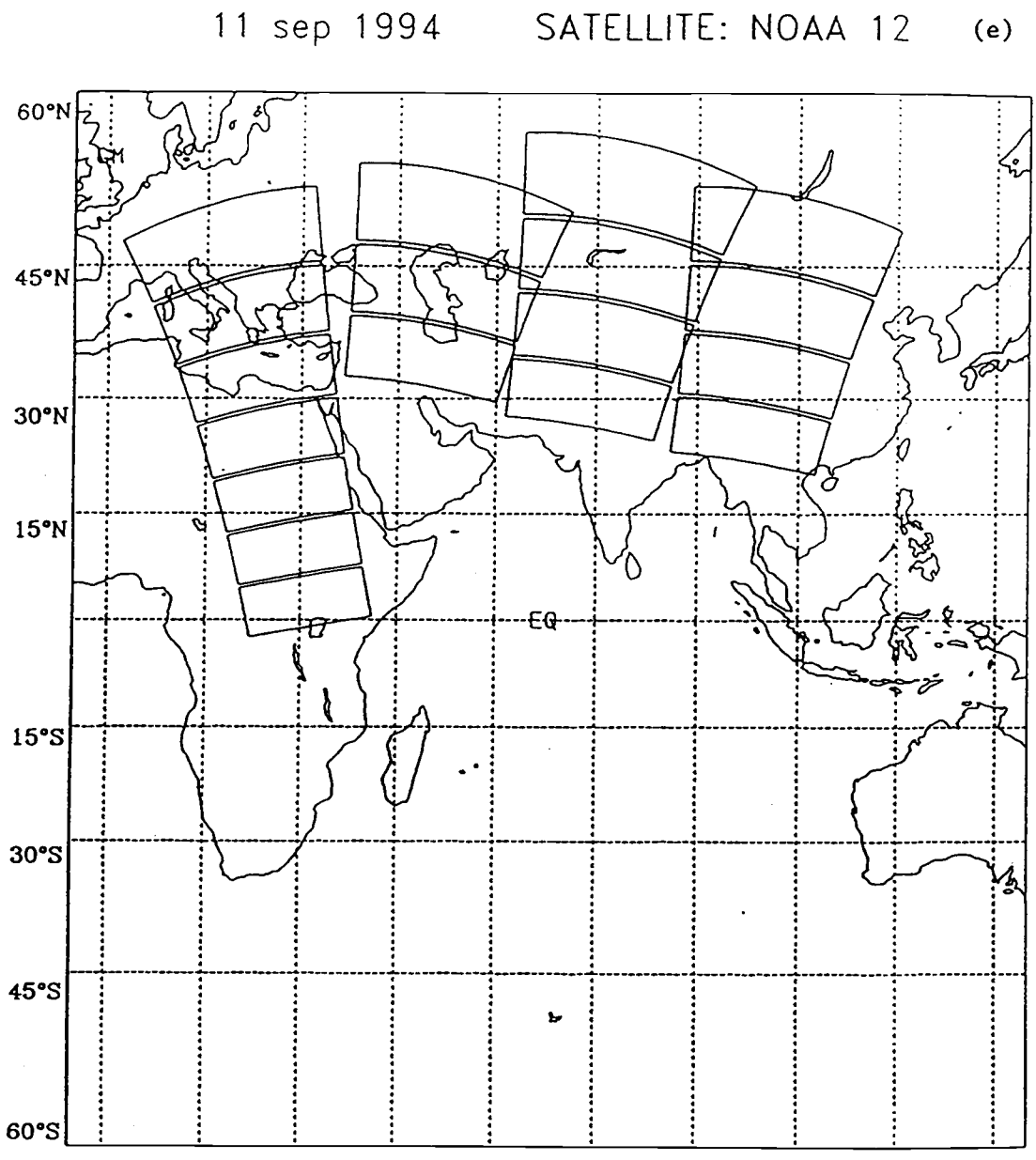
11 sep 1994 SATELLITE: NOAA 12 (e)
60°N
45°N
30°N
15°N
EQ
15°S
30°S
45°S
60°S

A frame or subframe is defined as cloud-free if the total fractional cloud cover (A_c) is less than 10% and there are no layers or overcast pixels within the region and as overcast if A_c is greater than 90% and there are no cloud-free pixels identified within the region. The number of layers is taken to be the number of distinct radiances emitted by pixels exhibiting locally uniform emission within the region or, for cases in which the overcast pixels do not explain the range of radiances, from overcast pixels in neighboring subframes. Comparison of the emitted radiances for the pixels overcast by the highest and thus coldest cloud layer with the tenth percentile of the cumulative distribution of emitted radiances determines whether or not the range of emitted radiances is entirely explained by the cloud layers in the region. If the lowest extreme of the range of radiances is within two standard deviations of the mean radiance for the overcast pixels associated with the coldest layer, then the clouds in the region are considered to reside in the layers identified by the spatial coherence method. A tenth percentile value not within the two standard deviation cutoff indicates contributions from pixels containing clouds at levels above the identified cloud layers. These upper-level clouds may belong to a layer for which none of the AVHRR pixels are overcast by clouds within the layer or the clouds may be distributed in altitude above the lower-level, layered systems. A region is considered cloudy but with no distinct layer structure if the number of identified layers is zero but cloud cover is between 10% and 90%. The nine cloud cover categories defined by these criteria are outlined in Table 3.1.

Cloud cover category	Defining criteria
1. Cloud free	$A_c < 0.10$; No overcast pixels & no layers identified
2. Overcast	$A_c > 0.90$; No cloud-free pixels
3. Cloudy but no identified layers	Layers identified = 0; $0.10 < A_c < 0.90$
4. Single layer only	Layers identified = 1; $I_{10} > I_{c1} - 2\Delta I_{c1}$
5. Single layer with unidentified upper-level cloud	Layers identified = 1; $I_{10} < I_{c1} - 2\Delta I_{c1}$
6. Two distinct layers only	Layers identified =2; $I_{10} > I_{c2} - 2\Delta I_{c2}$
7. Two layers with unidentified upper-level cloud	Layers identfied = 2; $I_{10} < I_{c2} - 2\Delta I_{c2}$
8. Three distinct layers	Layers identified = 3; $I_{10} > I_{c3} - 2\Delta I_{c3}$
9. Three layers with unidentified upper-level cloud	Layers identified = 3; $I_{10} < I_{c3} - 2\Delta I_{c3}$

Table 3.1 AVHRR cloud category criteria.

3.4 Determination of cloud-top altitudes

At infrared wavelengths, the clouds in the pixels identified as being overcast are assumed to be optically thick and therefore emit radiation according to Planck's Law for blackbody emittance given by

$$B_\upsilon = \frac{2hc^2\upsilon^3}{\exp\left\{\frac{hc\upsilon}{kT}\right\}-1}, \qquad (3.3)$$

where ν is the wavenumber,

h = Planck's constant (6.6262×10^{-34} J s)

c = speed of light (2.998×10^{8} m s^{-1})

and k = Boltzmann's constant (1.381×10^{-23} J deg^{-1}).

Inverting this equation to write temperature as a function of radiance yields

$$T = \frac{\left(\frac{hc}{k}\upsilon\right)}{\ln\left(\frac{2hc^2\upsilon^3}{B_\upsilon}+1\right)}. \qquad (3.4)$$

The wavenumber corresponding to the NOAA-12 AVHRR 11-μm channel is given as 927.34 cm^{-1} (NOAA). This formula allows calculation of a brightness temperature corresponding to each measured emitted radiance. These temperatures can then be combined with temperature and pressure profiles (in this case from the National Meteorological Center analyses) for that time and location to obtain an estimate of cloud-top altitude.

Assume that the atmosphere is in hydrostatic equilibrium, experiencing no net force in the vertical direction. Then the vertical pressure gradient exactly balances the

force of gravity and $\frac{\partial p}{\partial z} = -\rho g$. From the ideal gas law, $p = \rho RT$ where R is the gas constant (287 J K^{-1} kg^{-1}. Substituting for ρ,

$$\frac{\partial p}{\partial z} = -\frac{p}{RT} g \qquad (3.5)$$

so

$$\frac{1}{p}\partial p = -\frac{1}{T}\frac{g}{R}\partial z. \qquad (3.6)$$

Then for T dependent on z,

$$\ln(\frac{p}{p_o}) = -\ln(\frac{T}{T_o})\frac{g}{R}\frac{dz}{dT}. \qquad (3.7)$$

For $T(z)=T(z_o)$,

$$\ln(\frac{p}{p_o}) = -\frac{1}{T}\frac{g}{R}(z - z_o). \qquad (3.8)$$

The change of temperature with height is referred to as the environmental or ambient lapse rate, γ, given by

$$\gamma = \frac{dT}{dz} = \frac{-\frac{g}{R}\ln(T/T_o)}{\ln(p/p_o)}, \qquad (3.9)$$

for T a function of z. By integrating,

$$T - T_o = \gamma (z - z_o). \qquad (3.10)$$

Then, for each of 18 pressure levels from 1000 to 0.4 mb, the corresponding altitudes are given by

$$z = \frac{T - T_o}{\gamma} + z_o . \qquad (3.11)$$

For $T(z)=T(z_o)$,

$$z = \frac{-T(z_o)\ln(p/p_o)}{g/R} + z_o . \qquad (3.12)$$

Consecutive temperature estimates from the profile are used to estimate a lapse rate, γ, given by

$$\gamma = \frac{T_0 - T_1}{z_0 - z_1} . \qquad (3.13)$$

A cloud with brightness temperature falling between two consecutive profile temperatures ($T_0 > BT > T_1$) would have an altitude given by

$$z = z_0 + (\frac{1}{\gamma})(BT - T_0) . \qquad (3.14)$$

Chapter 4. Frequency of Occurrence Results

4.1 Layer Statistics for Geographical Regions

4.1.1 Pacific Ocean

A total of 244,992 subframes, corresponding to 87,973 2.5° regions, were analyzed for 11 days of AVHRR data over the Pacific Ocean. For comparison, the LITE data volume for this region totaled 2,204 60-km segments. Frequencies of occurrence for the nine cloud categories previously defined are shown in Figures 4.1.a (AVHRR) and b. (LITE). These percentages indicate the number of regions meeting the criteria for a specific category divided by the total number of regions analyzed.

At the 60-km subframe scale, single-layered systems are found in 35-40% of the AVHRR results and about 65% of the LITE results. Cloud systems composed of more than one layer (1+ or 2) are seen in approximately 25% of the LITE observations and in about 12% of the satellite observations. The occurrences of two or more cloud layers are fewer, on the order of 5% for both LITE and AVHRR. These results confirm the expectation that single-layered rather than more complex systems should dominate the subframe-scale observations, given that the spatial scales of well-organized cloud systems tend to be on the order of 100 km or larger.

At the 250-km scale, the AVHRR results indicate a 25-30% frequency for the occurrence of single-layered cloud systems, while the number of regions corresponding to a multi-layered system increases markedly. Two distinct cloud layers were reported for

about 35% of both the LITE and AVHRR observations, and the occurrences of more than two cloud layers were about 11% for LITE and 16% for AVHRR.

The difference in the scale of the analysis should also lead to a difference in the number of cloud-free or overcast regions, with 60-km scale regions more likely to meet the less than 10% or greater than 90% cloud cover criteria. For the Pacific Ocean, cloud-free frequencies at the 60-km scale were 21% for the AVHRR data but only on the order of 2% for the LITE results. At the 250-km scale, the satellite and lidar cloud-free frequencies were 6% and 1%, respectively. The very small number of LITE observations reported as cloud-free may be attributed in part to effects of the ten-shot averaging. For those data in which cloud-free returns are determined from the surface parameter, if only one of the ten shots corresponds to a cloud return, then the entire composite observation is reported as cloudy. Of the 5,249 one-second composites containing surface flag information for the Pacific Ocean, only 413 or 7.9% show a value corresponding to a cloud-free return. As expected in such a case, overcast frequencies tend to be higher for the LITE data than for the corresponding satellite results: 38% versus 3% for 250-km regions and 45% versus 6% at the 60-km scale. Because overcast regions tend to be composed of one or two layers plus unidentified cloud, they are therefore also counted as layered systems and the sums of the frequencies of occurrence will be greater than 1.

Figure 4.2a shows the frequencies of single layer, more than one layer, and more than two layer observations as a function of latitude for the 60-km scale AVHRR analysis. The maxima in each of the curves at ~5° N corresponds to the location of the ITCZ. The increase in overall cloudiness at this latitude can also be seen in Figure 4.2b, showing the distribution of overcast regions with latitude. Large layer frequencies and an increase in

total cloudiness is also seen in the northern mid-latitudes, corresponding to the autumn equinox and end of the northern latitude summer. Minima in layer frequencies and overall cloudiness are observed in the subtropical latitudes, 20° - 40°. The latitudinal frequencies at the 250-km scale vary slightly from the 60-km distribution, as evidenced in Figure 4.3. At all latitudes, multilayer frequencies are significantly higher for the 250-km results. Both the LITE and AVHRR results show multilayered cloud systems to be most prevalent in the region between the equator and 25°N, with approximately 55% of the observations corresponding to a cloud system composed of more than a single layer. LITE data coverage for this region is sparse however, consisting of 7 days of observations and a total of 12 passes (see Table 2.1).

4.1.2 Atlantic Ocean

Processing of the AVHRR data for the Atlantic Ocean resulted in 77,695 subframes and 18,523 2.5° regions for analysis. The number of 60-km LITE orbit segments for the Atlantic Ocean was 2,982. The results of these analyses are shown in Figure 4.4. The percentage of 60-km areas for which single-layered systems were observed was 72% for the LITE data and 38% for AVHRR. More than one layer or two distinct layers were found in approximately 21% of the LITE observations, and 15% of the satellite observations. The frequencies of occurrence of more than 2 cloud layers were 2% from LITE and 5% from AVHRR.

As stated previously, the number of multilayered cloud systems is expected to increase with spatial scale. The 250-km results indicate a 21% frequency of single-layered

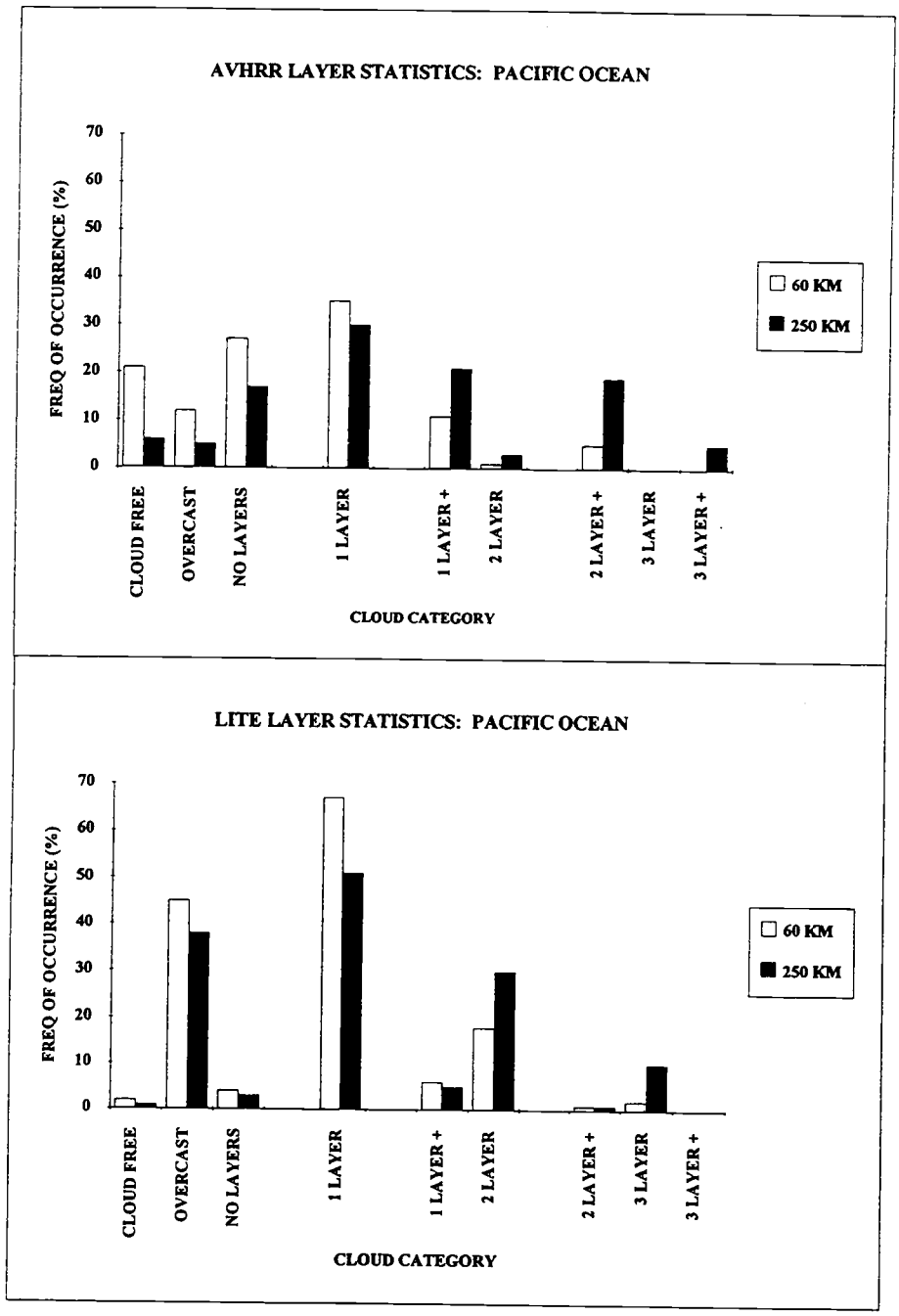

Figure 4.1 Cloud layer statistics from AVHRR and LITE: Pacific Ocean.

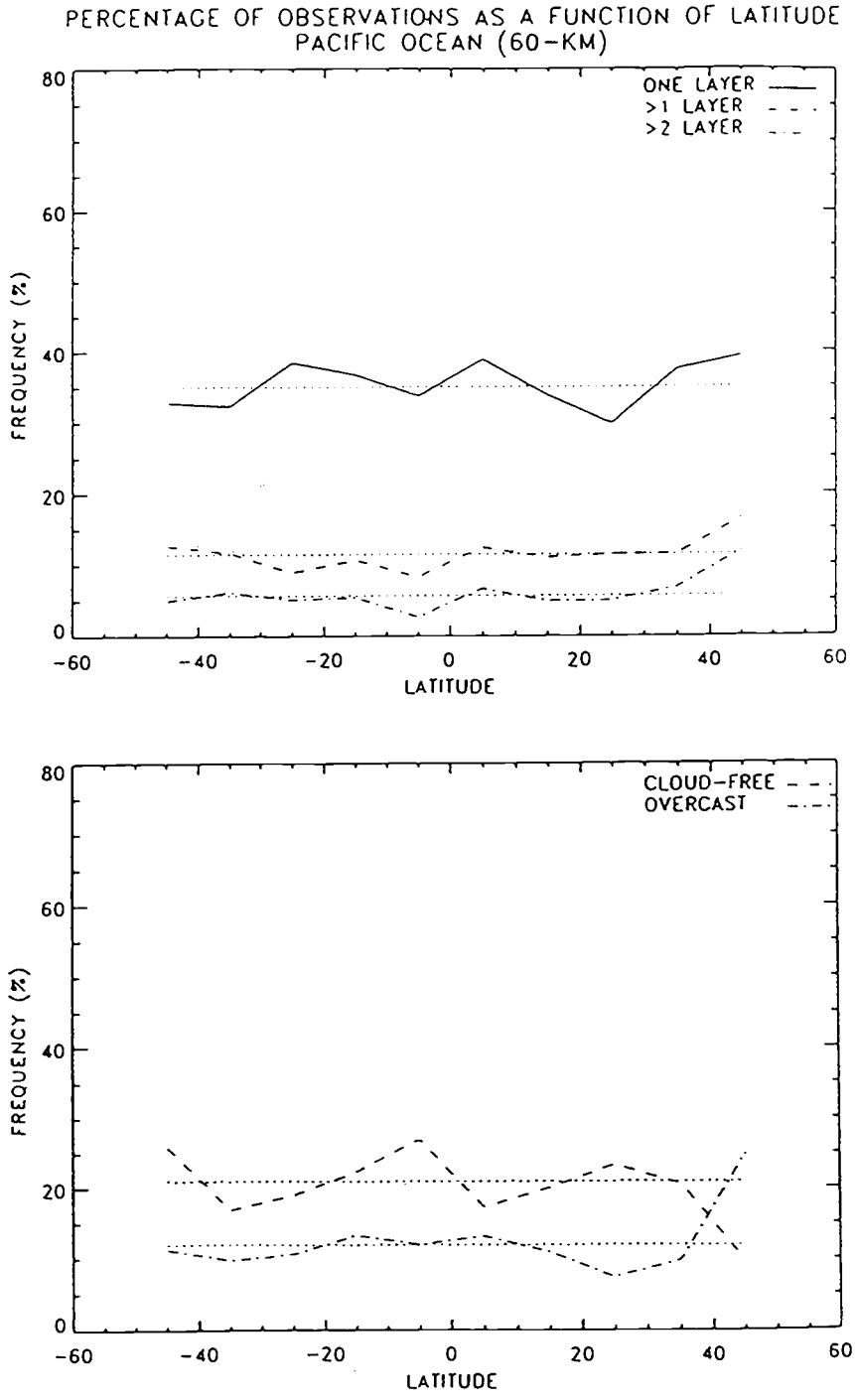

Figure 4.2 (a) Single and multilayered AVHRR occurrence frequencies as a function of latitude, (b) AVHRR cloud-free and overcast frequencies as a function of latitude.

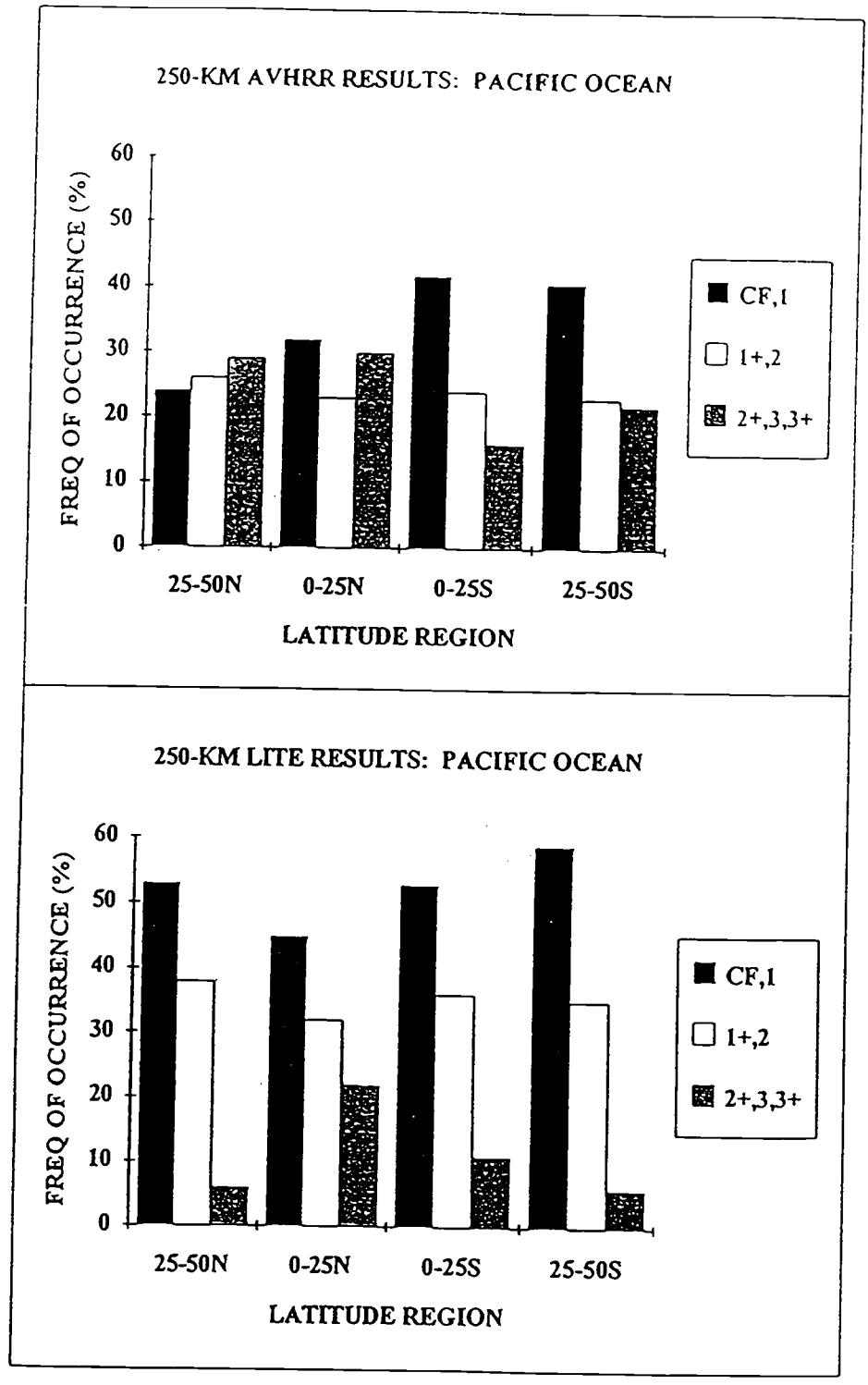

Figure 4.3 LITE and AVHRR layer statistics by latitude zone: Pacific Ocean.

systems from AVHRR compared to a 58% observed frequency in the LITE results. Cloud systems composed of two layers account for 35% of the satellite observations and about 36% of those from LITE. Frequencies of occurrence for systems composed of more than two layers are close to 30% for AVHRR and 4% from LITE.

Cloud-free and overcast frequencies show the expected decrease as the scale of the analysis increases from 60 to 250 km. The AVHRR results show 20% of observations to be cloud-free at the 60-km scale, but only 6% are cloud-free at 250-km. Cloud-free frequencies from LITE are low at both scales while overcast frequencies are high, due to the ten-shot compositing discussed earlier. Overcast frequencies decrease from 32% to 27% for LITE, and 11% to 2% for AVHRR.

AVHRR cloud frequencies as a function of latitude are shown in Figure 4.5. Multilayered systems tend to be more prevalent in the northern hemisphere than in the southern, with a minimum occurring in the southern tropics between 10 and 20°S. This minimum in multilayered cloud corresponds to a maximum in overcast occurrences and also a maximum in single layer observations. By contrast, overcast occurrences are a minimum and cloud-free occurrences a maximum north of 20°N, where the number of multilayered systems is also high.

Figure 4.6 shows 250-km occurrence frequencies as function of latitude. Single-layered systems comprise a higher percentage of observations in the southern hemisphere, as indicated by both the AVHRR and the LITE results. Multilayered cloud systems are prevalent across all latitude zones, with slightly higher frequencies of occurrence in the tropics. The very high number of single-layered systems observed during LITE may be a

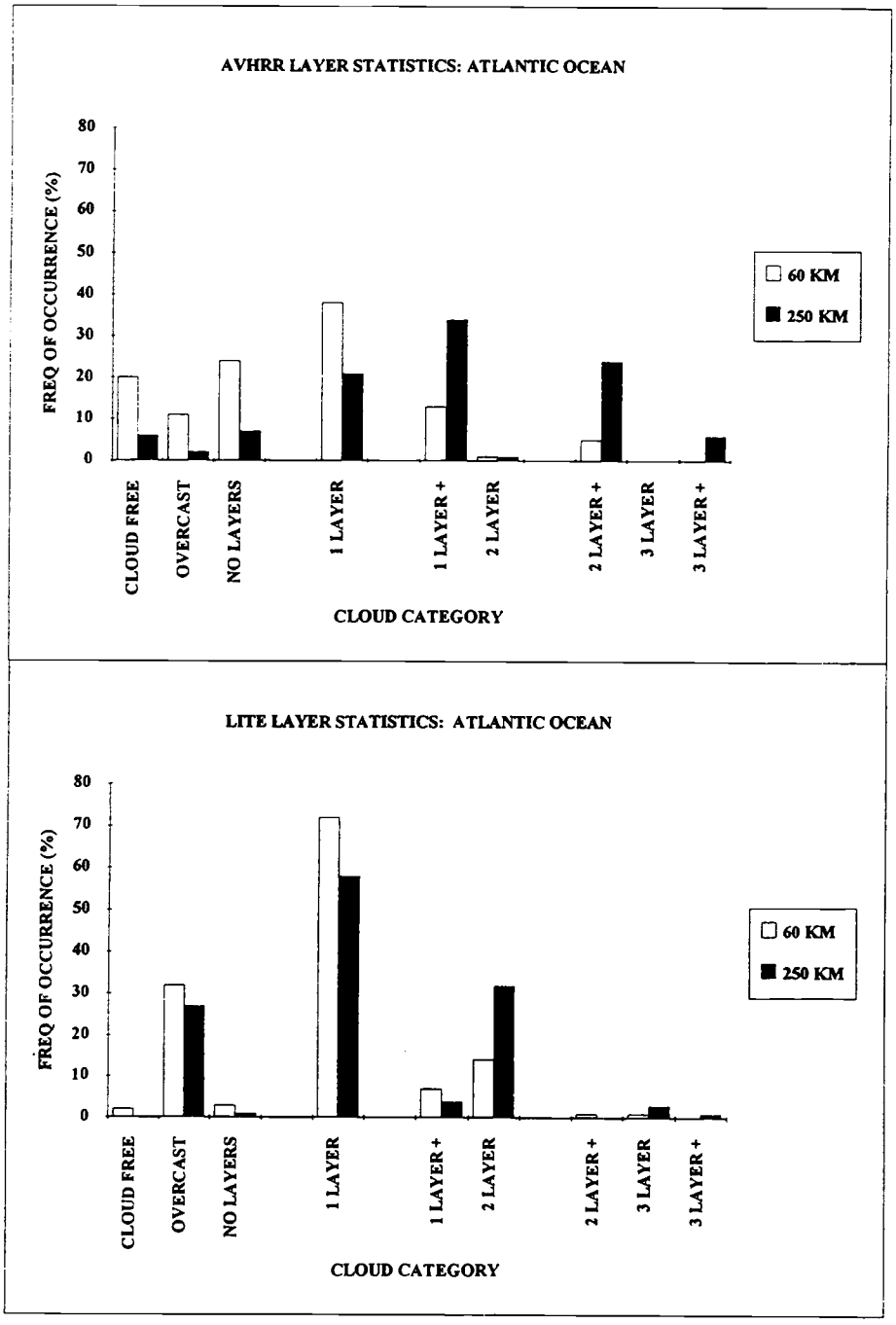

Figure 4.4 Cloud layer statistics from AVHRR and LITE: Atlantic Ocean.

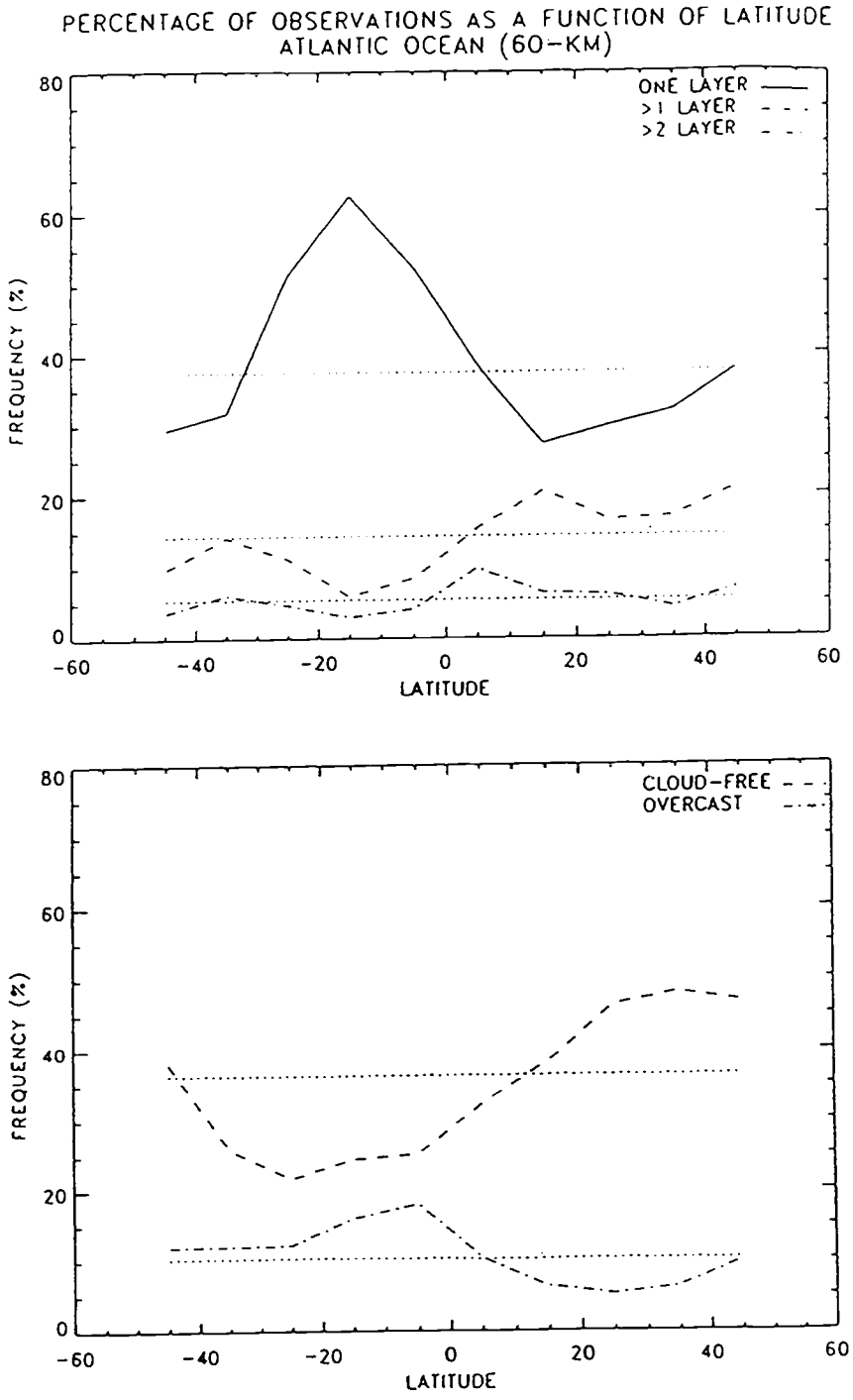

Figure 4.5 (a) Single and multilayered AVHRR occurrence frequencies as a function of latitude, (b) AVHRR cloud-free and overcast frequencies as a function of latitude.

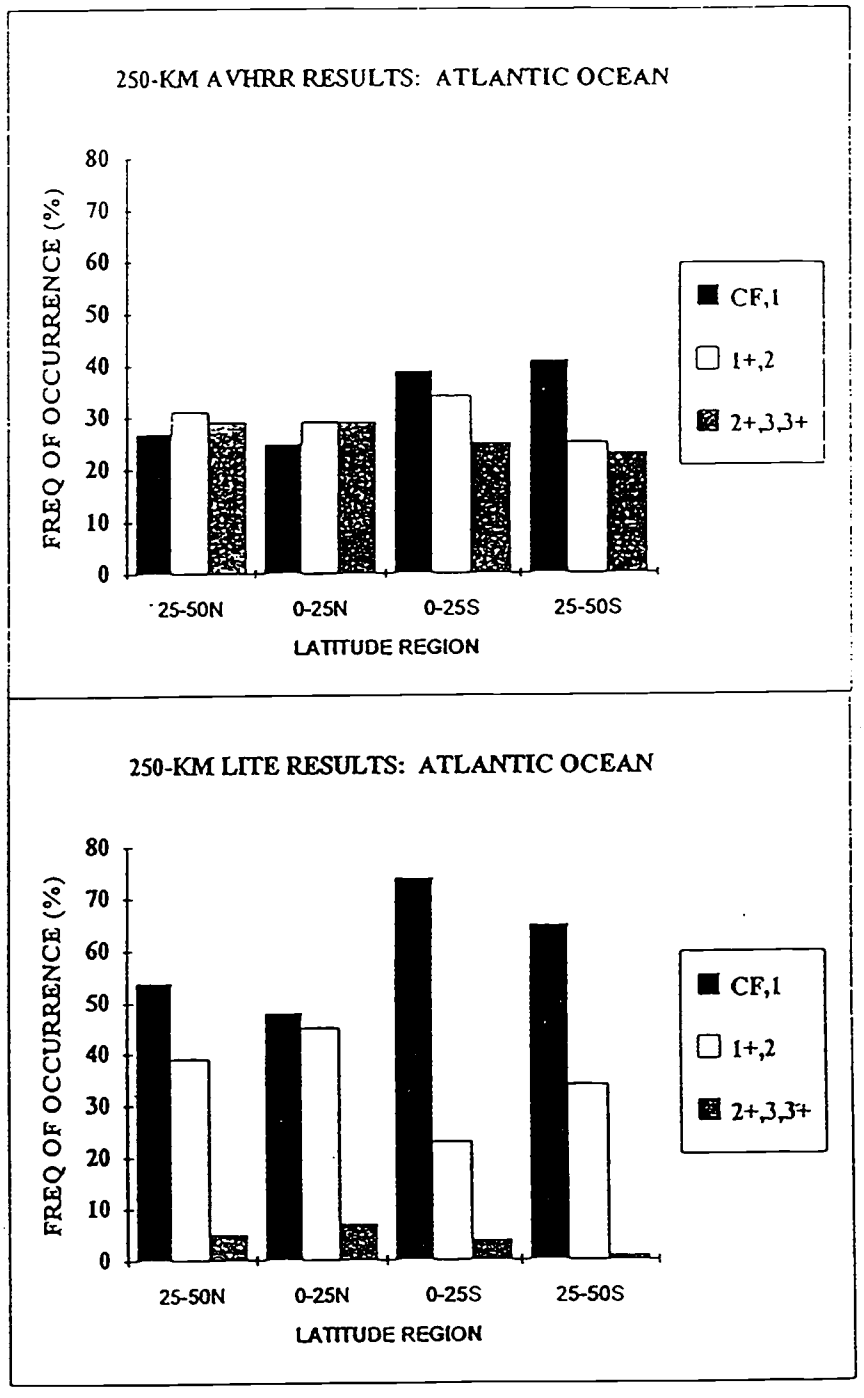

Figure 4.6 LITE and AVHRR layer statistics by latitude zone: Atlantic Ocean.

factor of the LITE data compositing and can also be attributed to the effects of one-dimensional versus two-dimensional spatial analysis, as illustrated in Section 4.2.

4.1.3 Indian Ocean

The data analyzed for the Indian Ocean region included 70,654 subframes of satellite data and 490 60-km LITE orbit segments. The results are shown in Figure 4.7 and indicate single-layer frequencies for the 60-km scale are approximately 72% for LITE and 32% for AVHRR. One layer plus other contributions or two distinct layers are seen in 15% of the satellite and 19% of the lidar results. More than two cloud layers are observed for 5% of the AVHRR observations and in about 7% of those from LITE.

At the 250 km scale, single-layered systems are reported for 64% of the LITE observations and 30% of the AVHRR observations. The frequencies of occurrence for more than one cloud layer are 29% from satellite and 27% from LITE. More than two layers are found to be present in 21% of the satellite observations and 7% of those for LITE.

The LITE and AVHRR results show large discrepancies in the overall cloudiness for this region, with 46% of the 60-km LITE results and only 5% of the satellite results reported as overcast for this region. By contrast, AVHRR cloud-free frequencies were 45% for the 60-km scale and 14% for the 250-km scale while the corresponding cloud-free lidar observations were on the order of 3%. Differences in the amount, including number of days and geographic extent, of the satellite and LITE data may explain some of

these discrepancies. Misidentification of completely overcast regions as cloud-free by spatial coherence analysis may also contribute to the lower cloud cover frequencies observed by AVHRR.

Cloud layer occurrences as a function of latitude based on the satellite results are shown in Figure 4.8 . At the 60-km scale, occurrences of cloud systems composed of more than one cloud layer are highest at about 5°S, the same latitude at which the number of single layered systems is a minimum. The number of overcast regions observed by radiometer is consistently low over the entire basin, with cloud-free occurrences particularly high in the tropical equatorial regions.

Figure 4.9 shows 250-km occurrence frequencies as a function of latitude from the AVHRR and LITE data. Multilayered cloud systems dominate the observations northward of the equator while single-layered systems are most prevalent in the region from 25° to 50° S. As in previous cases, the LITE results show a systematic bias toward single-layer systems when compared to those from AVHRR, however both datasets agree as to the location of maxima and minima in the occurrence frequencies.

4.1.4 North and South America

36,854 subframes and 3,042 2.5° regions of satellite data and 1,585 60-km segments of LITE data were analyzed for the North and South American continent. The results are shown in Figure 4.10. More complexity is expected for cloud systems over land, attributed to orographic forcing, convection, and other mechanisms of cloud formation. At the 60-km, the LITE results report single-layered systems for

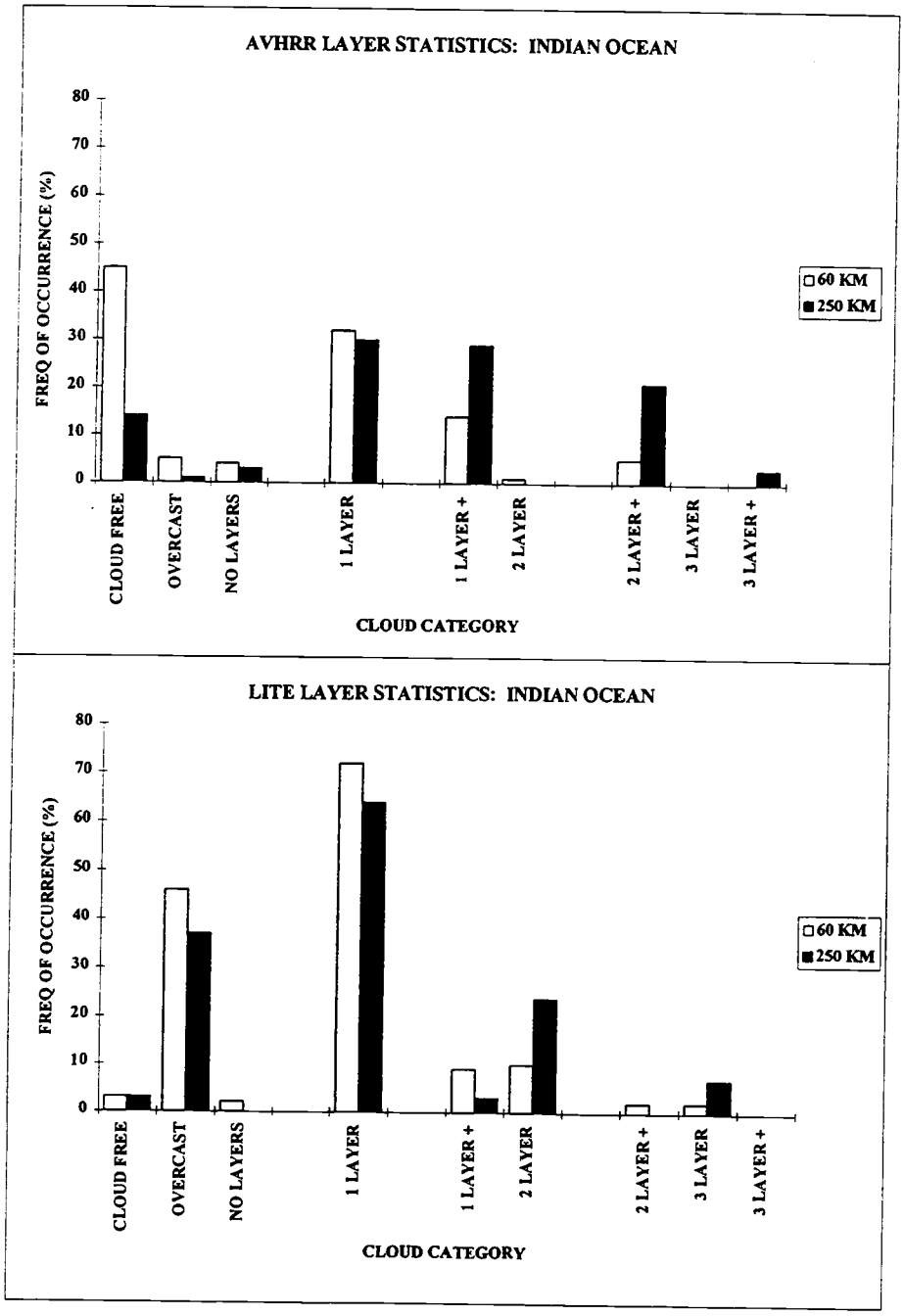

Figure 4.7 Cloud layer statistics from AVHRR and LITE: Indian Ocean.

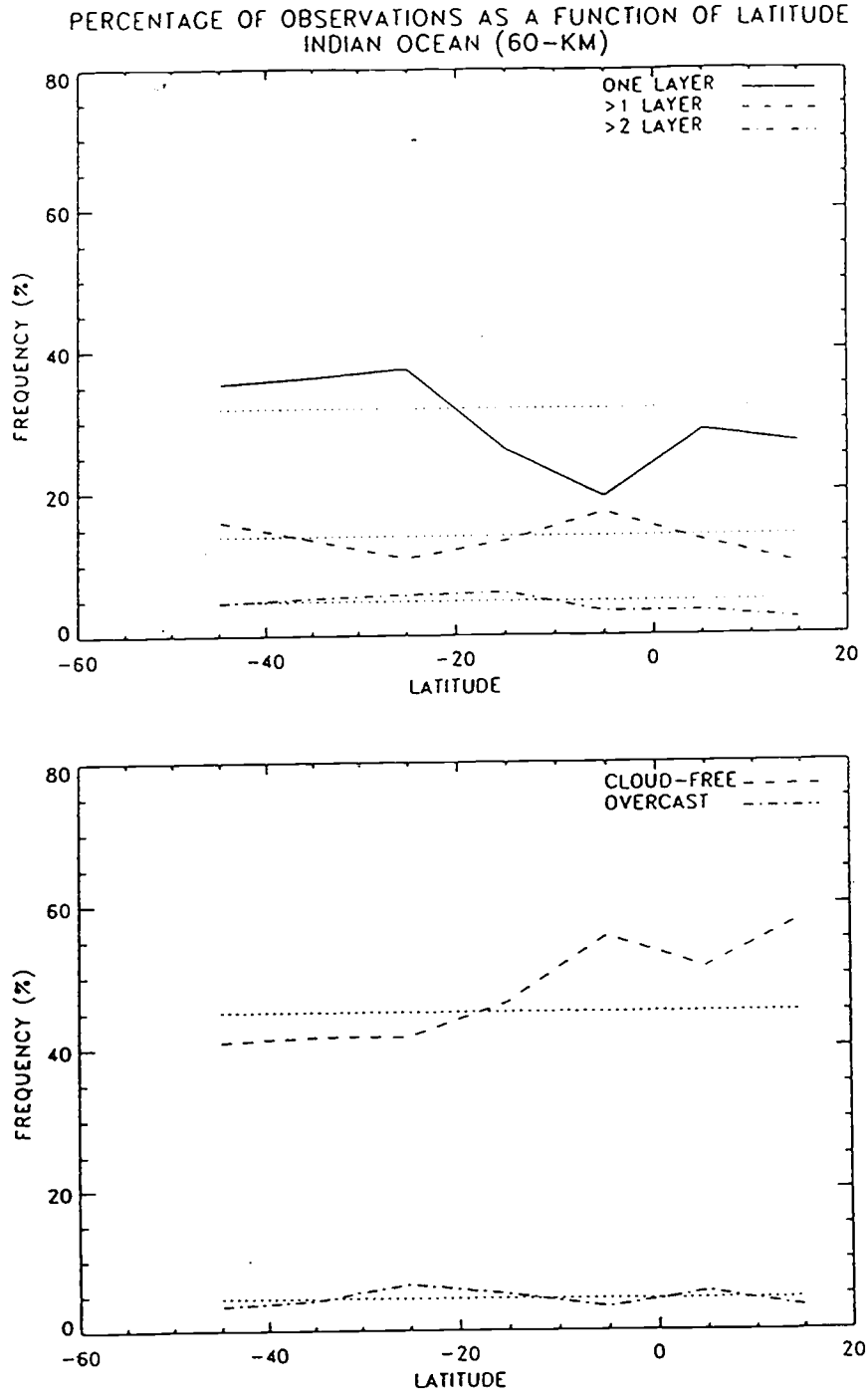

Figure 4.8 (a) Single and multilayered AVHRR occurrence frequencies as a function of latitude, (b) AVHRR cloud-free and overcast frequencies as a function of latitude.

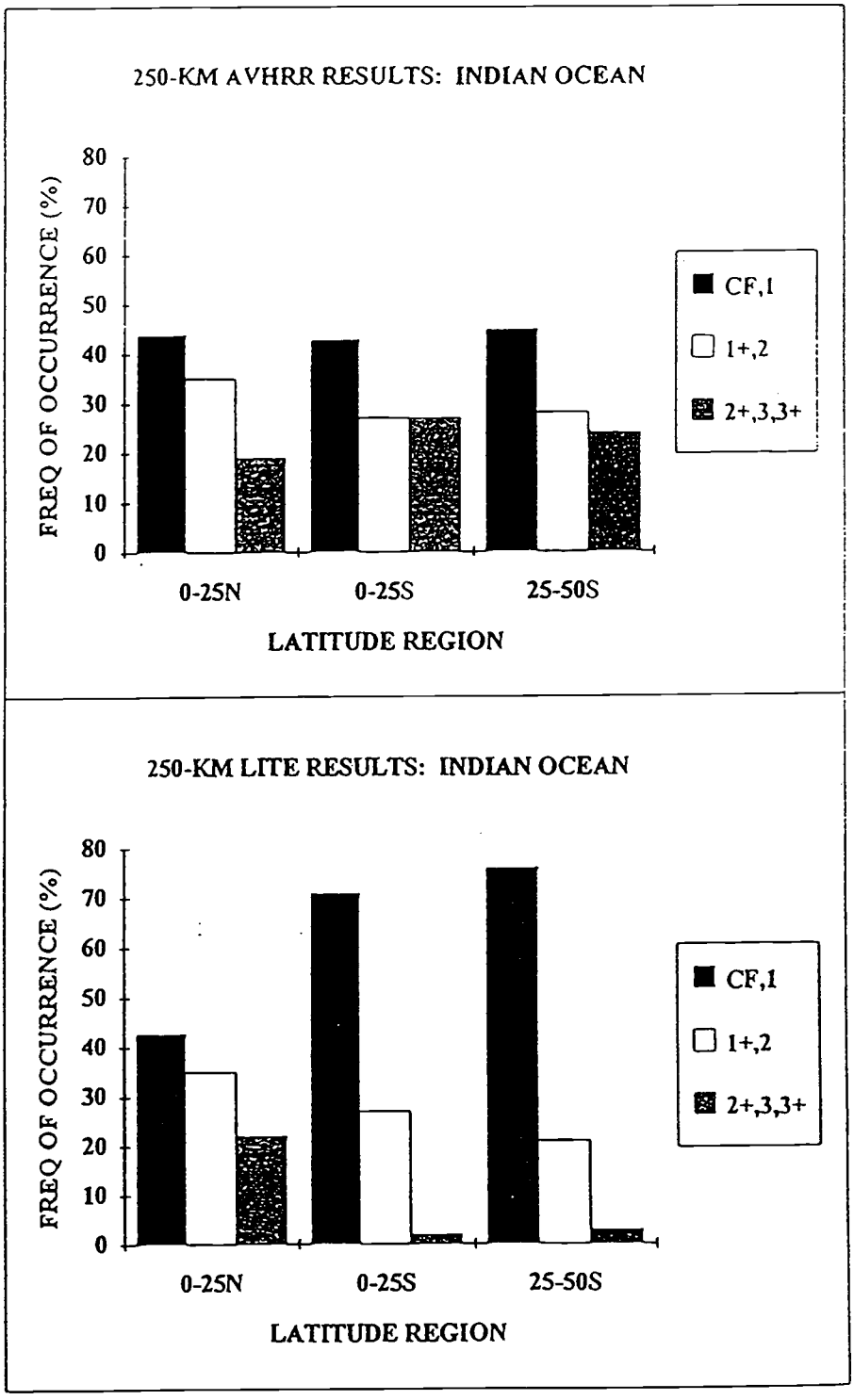

Figure 4.9 LITE and AVHRR layer statistics by latitude zone: Indian Ocean.

approximately 52% of the observations while AVHRR single layer frequencies are on the order of 25%. Two-layered systems occur in approximately 18% of the subframes and 27% of the lidar observations, while cloud systems consisting of more than two layers are present in approximately 5% of both the LITE and AVHRR observations.

The 250-km scale results show larger frequencies for two- and three-layered systems, with two layers found for 35% of the LITE observations and 38% of the satellite regions. The frequencies of occurrence of systems composed of more than two layers were 9% for LITE and 26% for AVHRR. Single-layered systems were reported in only 13% of the satellite observations and 48% of the LITE results.

The number of clear sky regions is higher for the North and South American continents than for the ocean regions examined above. Satellite results show 45% of 60-km subframes and 20% of 2.5° frames to be cloud-free. The corresponding LITE frequencies are 13% for the 60-km scale and 8% at 250 km. Overcast frequencies thus decrease substantially compared to the ocean data, with only 6% of the AVHRR observations meeting the overcast criteria at the 60-km scale. For the LITE data, overcast frequencies are about 25% and 21%, for 60 and 250 km, respectively.

Land-only data for North and South American are severely limited between 10°S and 20°N and below 30°S. From the available satellite data, cloud-free frequencies tend to be high over both the North and South American continents, with the highest values reported for the southern subtropics. Observations of multilayered cloud systems are highest for the northern hemisphere subtropics, from 20-30°N. Complex systems are expected to be most prevalent in the tropics and mid-latitudes. The large number of multilayered systems seen for the South American subtropics may be attributed to a

relative minimum in overcast occurrences for this region, allowing the satellite to observe more than a single cloud layer.

4.1.5 Africa and Europe

Analysis of 49,536 subframes and 10,218 2.5° regions of AVHRR data was completed for comparison with the 1,353 60-km segments of LITE data over Africa and southern Europe. Figure 4.11 shows the 60- and 250-km scale layer frequencies. The numbers are comparable to those observed for North and South America. Fifty-eight percent of the 60-km LITE observations show a single-layered cloud system, compared with about 35% from the AVHRR imagery. Two cloud layers were identified in 22% of the satellite and the LITE observations, while the corresponding frequencies for more than two cloud layers were 3 to 5% for both LITE and AVHRR.

The number of layers present increases at the 250-km scale, with two layers occurring in 40% of the satellite observations and 39% of those from LITE. Cloud systems composed of more than two cloud layers were found in 29% of the satellite observations but only 4% of the LITE results. Single-layer frequencies at this scale were 15% from AVHRR and 46% for the LITE data.

Cloud-free frequencies obtained from the satellite results are high, on the order of 40% at the 60-km scale and 15% at the 250-km scale. By contrast, the number of regions identified as overcast is lower, approximately 5% (60-km) and 0% (250-km) from satellite and 4% (60-km) and 2% (250-km) from the LITE results. LITE observations also reveal comparatively large cloud-free frequencies, about 7% for the 250-km scale and 12% for

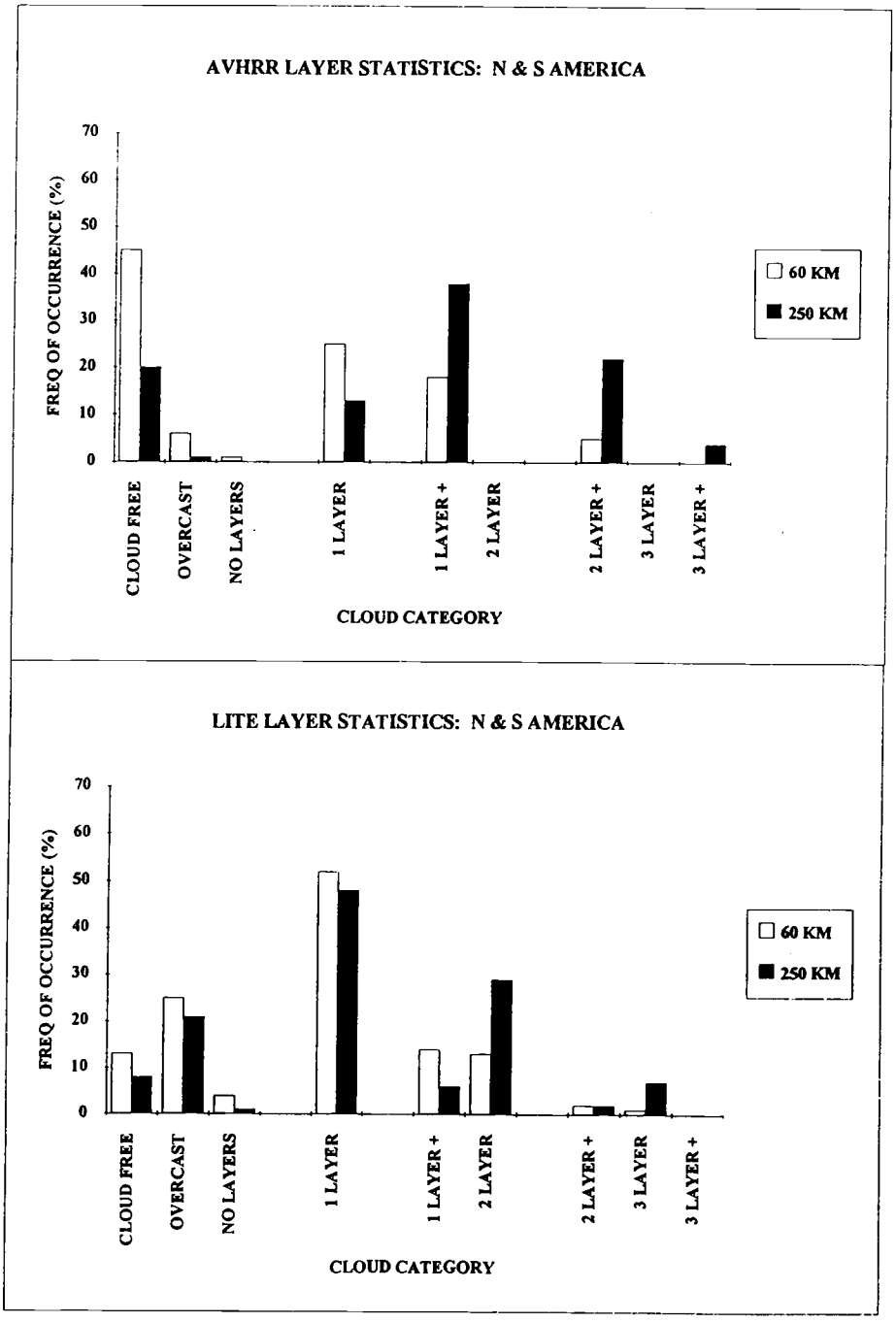

Figure 4.10 Cloud layer statistics from AVHRR and LITE: North and South America.

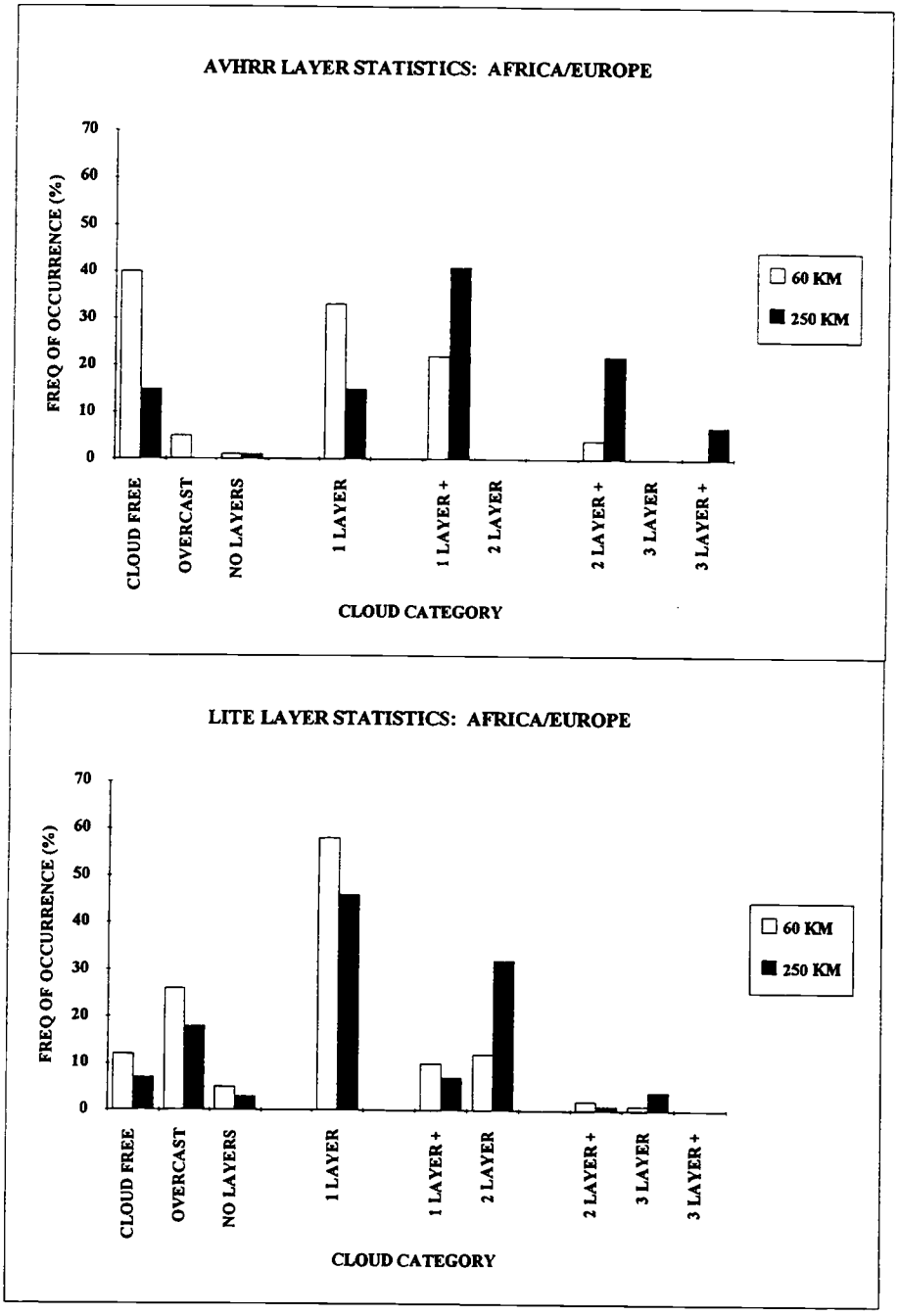

Figure 4.11 Cloud layer statistics from AVHRR and LITE: Africa and Europe.

the 60-km scale. Observed overcast frequencies for the LITE data are 18% at 250 km and 26% for the 60-km scale.

4.1.6 Asia

53,760 subframes and 11,090 2.5° regions of AVHRR data were processed for the region over Asia. Corresponding LITE data for this region amounted to 228 60-km sub-segments. 60-km single-layer frequencies are 30% for the satellite data and about 54% for the LITE results. Results show more than one cloud to be present in about 20% of the total satellite observations, compared to 28% for LITE. The 60-km frequencies for more than two cloud layers are 5% (AVHRR) and 4% (LITE).

Multilayered systems are observed more often at the 250-km, as would be expected and as seen in previous discussions. For the LITE data, more than one cloud layer is observed 38% of the time while for the AVHRR results, the corresponding frequency is 45%. More than two cloud layers are reported in 25% of the AVHRR observations and in 6% of the LITE observations.

Cloud-free and overcast frequencies differ substantially for LITE and AVHRR results for this region. LITE cloud-free frequencies are 11% for the 60-km scale and 6% at 250 km while respective overcast frequencies are 65% and 50%. For the satellite data, cloud-free regions are reported 44% of the time at 60 km and 18% of the time at 250 km. Respective overcast frequencies are 8% and 0.4%.

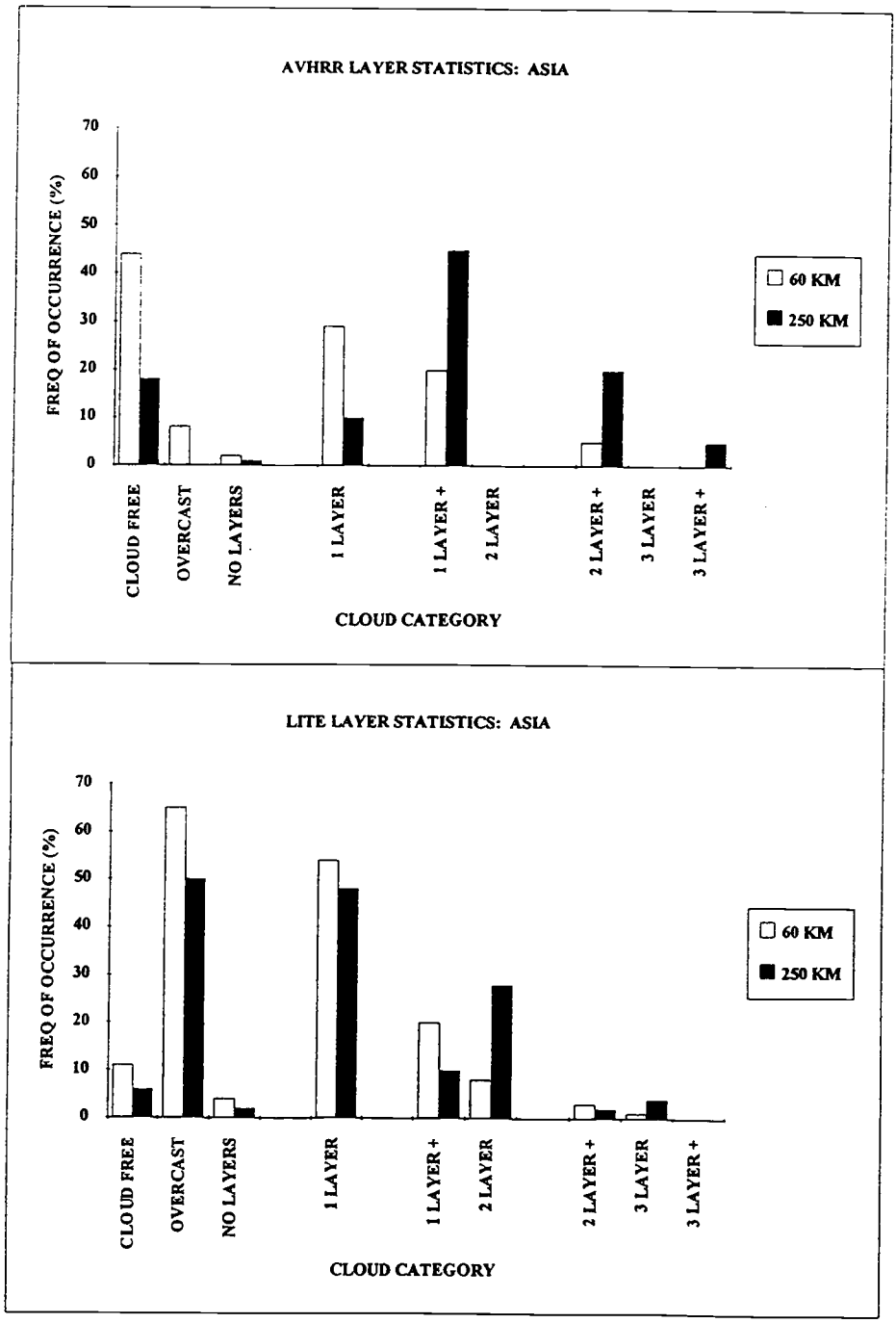

Figure 4.12 Cloud layer statistics from AVHRR and LITE: Asia.

4.1.7 Australia

Continent size and satellite scene coverage pose difficulties for analyzing satellite data over Australia. Analysis was completed for 141 60-km sub-segments of LITE data and results are summarized in Figure 4.13. The results report single-layered systems approximately 50% of the time for 60 km, while more than one layer is present in 26% of the 60-km results and approximately 45% of the 250-km observations. Cloud-free and overcast frequencies are similar to other continental regions, with 19% of 60-km sub-segments and 4% of 250-km sub-segments reported as cloud-free and 26% and 18% of the respective regions determined to be overcast.

4.1.8 Comparison of Land and Ocean Results

Tables 4.1 and 4.2 show the frequencies of occurrence of cloud-free and overcast regions and single- and multilayered cloud systems over land, ocean, and the entire globe. At both scales of analysis, single-layered systems are found more often over ocean than over land, as evidenced by both the AVHRR and the LITE results. Single-layered cloud systems are found in 35% of the AVHRR 60-km results for ocean, and in 31% of the corresponding results for land. LITE single-layer occurrences are 66% for ocean and 54% for land. Multilayered cloud occurrences are observed more often over land, as expected due to the multitude of cloud formation processes at work. At the 250-km scale, the LITE results indicate multilayer frequencies of 44% and 40% over ocean and land respectively. The 250-km AVHRR analysis shows a 70% frequency of occurrence of multilayered systems over land compared to a 48% frequency over the oceans.

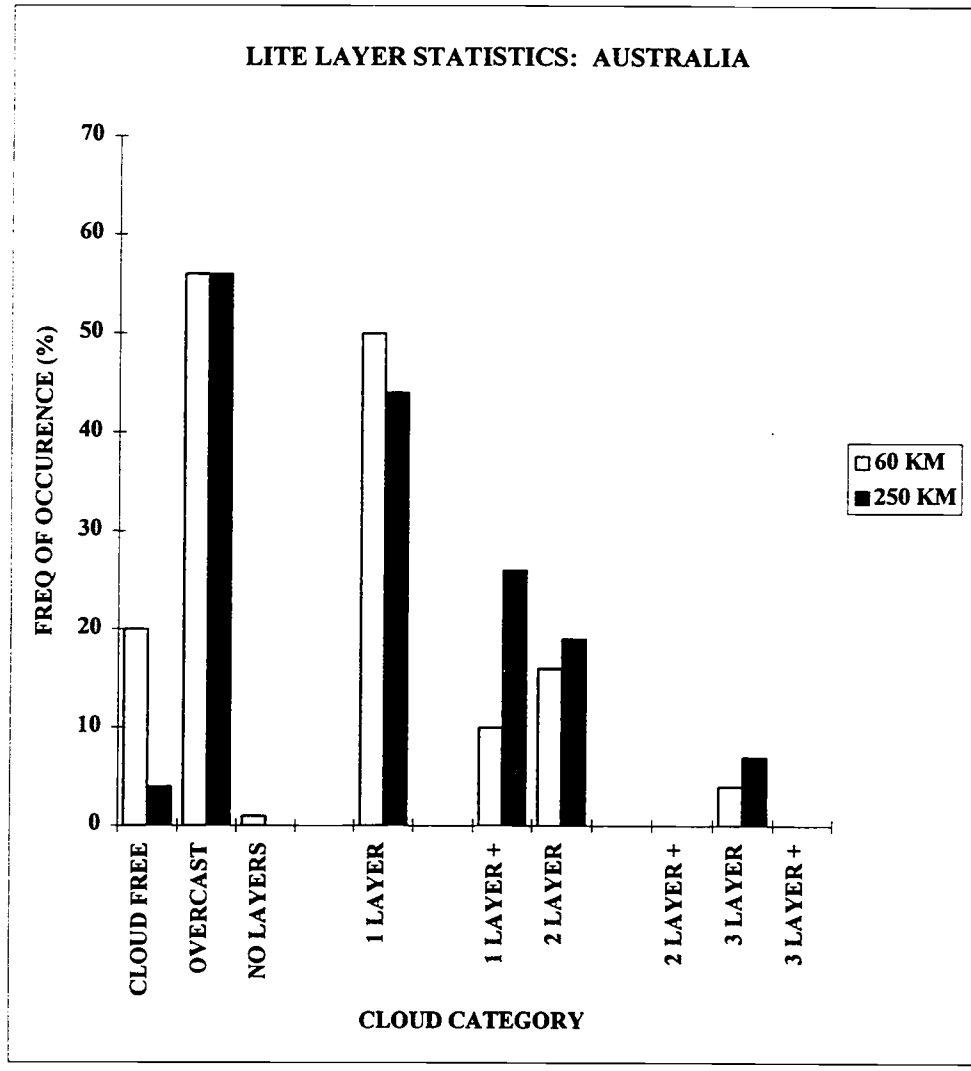

Figure 4.13 Cloud layer statistics from LITE: Australia.

Cloud-free regions are more likely over land than over ocean in both the LITE and AVHRR results. At the 60-km scale, AVHRR cloud-free frequencies are 45% over land and 28% over the ocean. LITE cloud-free frequencies are lower but still on the order of 10-20% greater for land than for ocean.

4.2 One-Dimensional Versus Two-Dimensional Analysis

Differences in the spatial coverage of the LITE and AVHRR instruments impact comparisons of the final layer statistics. The LITE dataset is essentially one-dimensional in horizontal space due to the small footprint of the instrument. The AVHRR observations, on the other hand, provide coverage both along the scan line and in the orbital direction, making a two-dimensional dataset. The effects of the one-dimensional and two-dimensional sampling are illustrated here.

AVHRR subframes corresponding to LITE data locations over the Atlantic Ocean on Day 253 were selected for use in this analysis. Locations of the 60-km subframes are plotted with the corresponding LITE data segments in Figure 4.14. Cloud layer statistics were computed for these subframes using the AVHRR cloud criteria discussed previously. Two cases were considered: the first allowing interpolation from neighboring subframes and the second requiring that the overcast pixels be present within the subframe itself. Analysis of all subframes in the region provides a measure of the two-dimensional statistics. The results are shown in Figure 4.15a and demonstrate the effect of one-dimensional sampling on the overall statistics. The frequencies of occurrence of single-layered systems for subframes only along one-dimensional segments were in both cases

	OCEAN		LAND		GLOBE	
	LITE	AVHRR	LITE	AVHRR	LITE	AVHRR
Cloud-free	2	28	13	45	6	33
Overcast	38	10	30	6	35	9
Single layer	70	35	54	31	64	34
> 1 layer	22	13	25	21	23	15
> 2 layer	3	6	3	5	3	6
num of regions analyzed	5676	377,086	3307	140,070	8983	517,156

Table 4.1 Occurrence frequencies (%) for 60-km regions.

	OCEAN		LAND		GLOBE	
	LITE	AVHRR	LITE	AVHRR	LITE	AVHRR
Cloud-free	1	8	7	17	3	10
Overcast	32	4	23	1	29	4
Single layer	56	32	47	12	53	29
>1 layer	35	20	37	43	36	32
> 2 layer	7	28	7	27	7	27
num of regions analyzed	1182	110,326	705	25371	1887	135,697

Table 4.2 Occurrence frequencies (%) for 250-km regions.

higher than that shown for the two-dimensional AVHRR results. Likewise, frequencies of occurrence of multiple cloud layers decreased for the one-dimensional observations.

Figure 4.15b shows 250-km layer statistics adjacent with the Day 253 Atlantic Ocean LITE data. One-dimensional AVHRR statistics were obtained by $(250\text{-km})^2$ analysis for frames collocated with the LITE data. The results of this frame-scale analysis are denoted "1-D adjacent." One-dimensional AVHRR statistics are also obtained from composites of four $(60\text{-km})^2$ subframes along an orbital segment to obtain an approximately 60×250 km^2 region. This string of subframes is denoted "1-D composite" and provides a closer representation of one-dimensional data. The two-dimensional AVHRR results are obtained from frame-scale analysis over the entire region. The one-dimensional AVHRR statistics are seen to behave similarly to the LITE observations, with one- and two-layered systems comprising significant percentages of the one-dimensional observations, and more complex systems seen less frequently than in the two-dimensional observations.

The effect of scale on the layer occurrence results is demonstrated in Figure 4.16. At the single ("one-dimensional") subframe scale, single cloud layers are observed in approximately 35% of those subframes for which no interpolation was allowed, and in about 55% of the observations after interpolation of overcast pixel radiances from neighboring subframes. Single-layer frequencies are smallest for the two-dimensional and $(250\text{-km})^2$ frame-scale data, where multiple cloud layers comprise close to 50% of the observations. This dependence on the spatial dimension of the data provides useful information concerning the differences in cloud layer statistics obtained from LITE and AVHRR and demonstrates the uniqueness of the LITE observations.

Figure 4.17 shows single and multi-layered cloud occurrence frequencies as a function of the number of subframes used in the analysis. For the one-dimensional data (subframes adjacent to an orbital track), the occurrence frequencies begin to approach a steady value at approximately 2000 subframes. Two-dimensional analysis also shows a leveling out of the statistics at about 2000 subframes, although a steady value does not seem to be approached until > 7000 subframes. This indicates that given enough observations, the one-dimensional results will approach those observed for the two-dimensional analysis. Were more LITE data therefore available, the effects of the one-dimensional sampling would be reduced and better agreement between the LITE and AVHRR results could be expected.

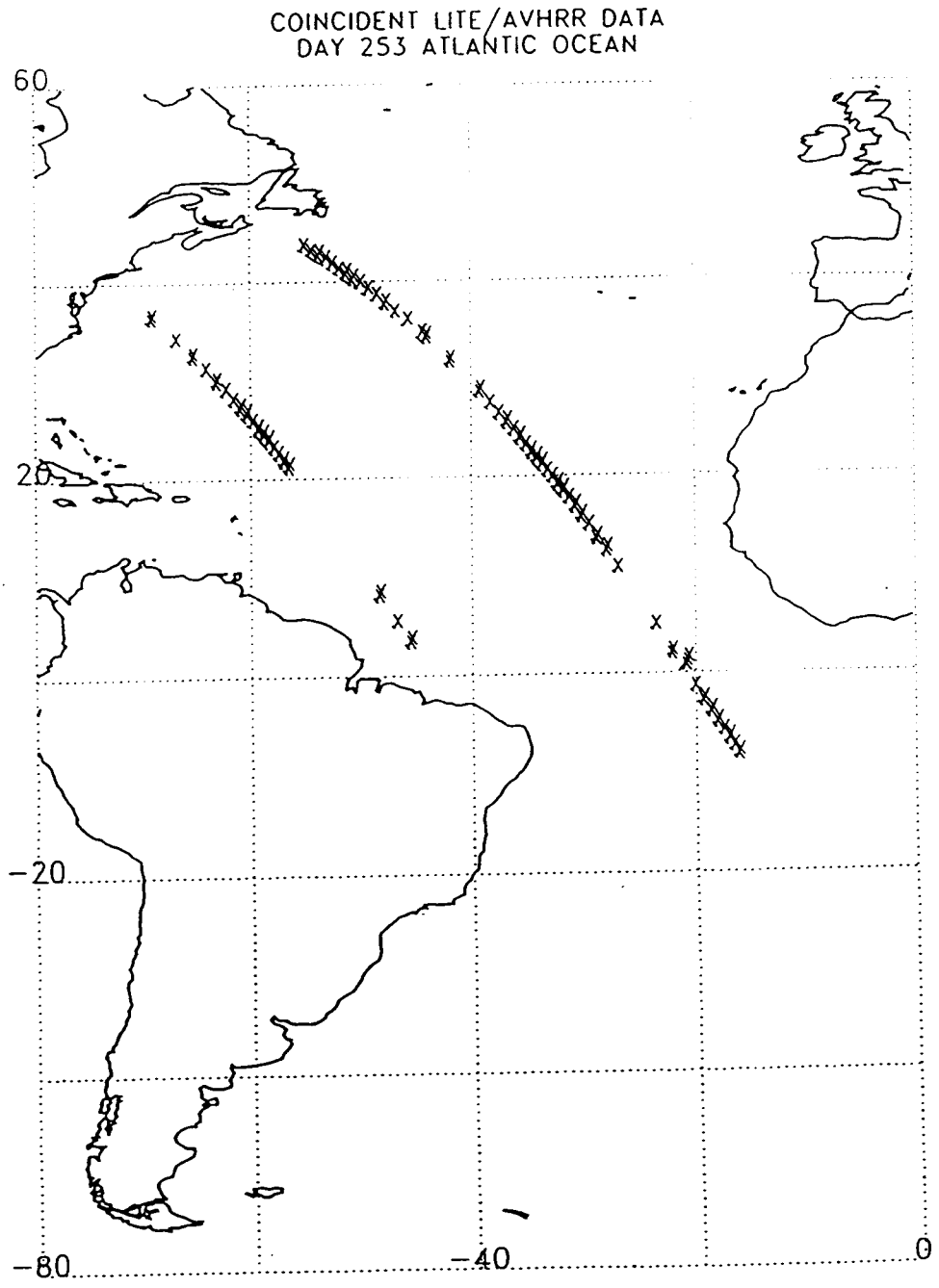

Figure 4.14 LITE ground tracks and coincident AVHRR subframes over the Atlantic Ocean, Julian Day 253

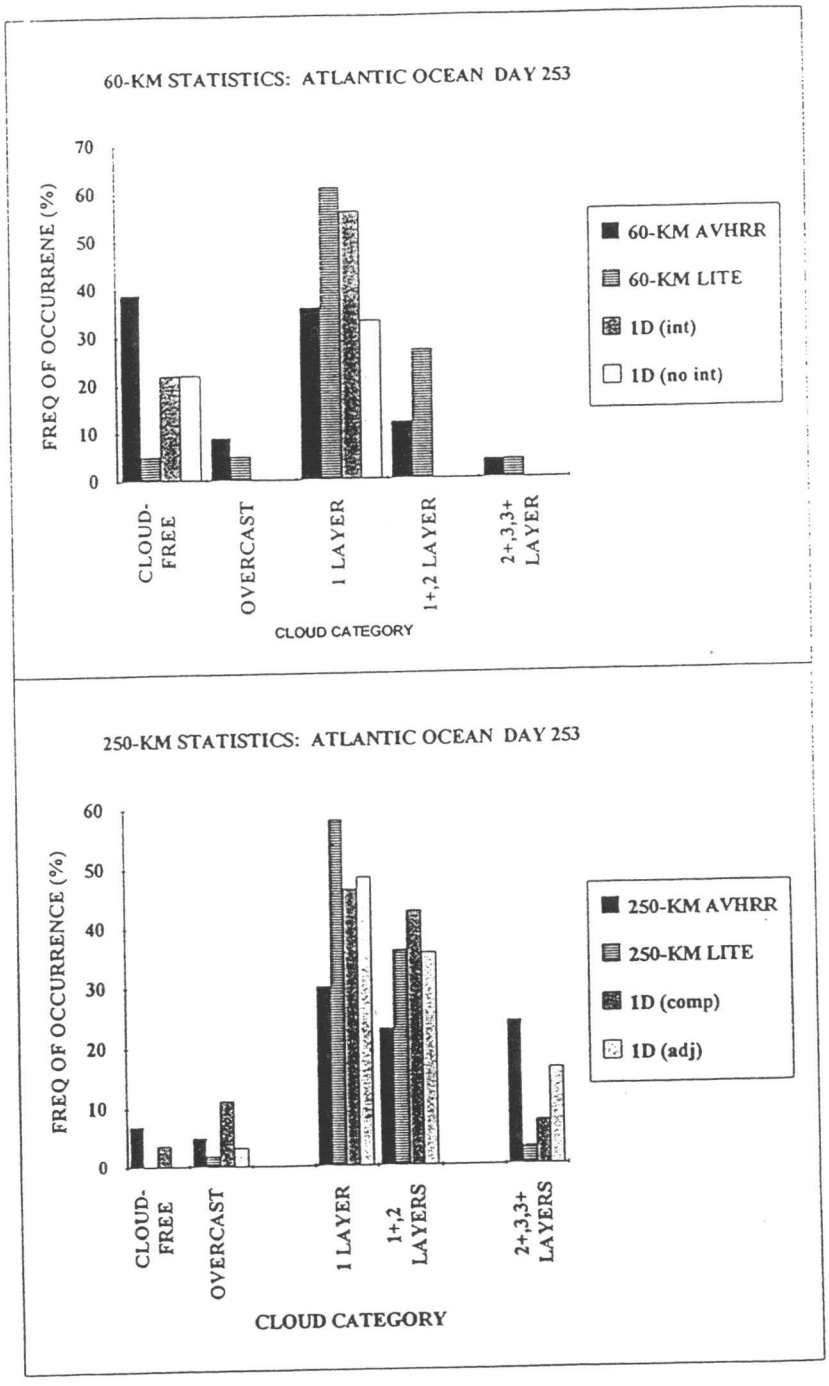

Figure 4.15 One- and two-dimensional cloud layer statistics: (a) 60 km, (b) 250 km.

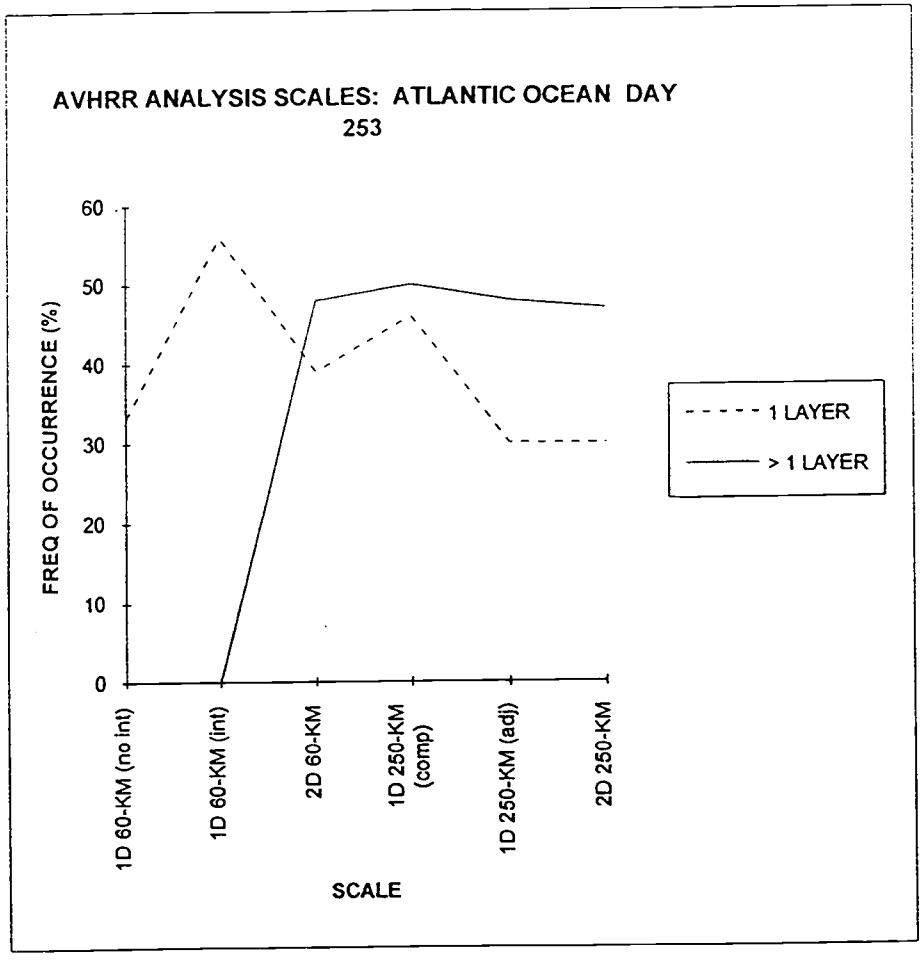

Figure 4.16 Single and multi-layer cloud frequencies as a function of spatial scale and dimension.

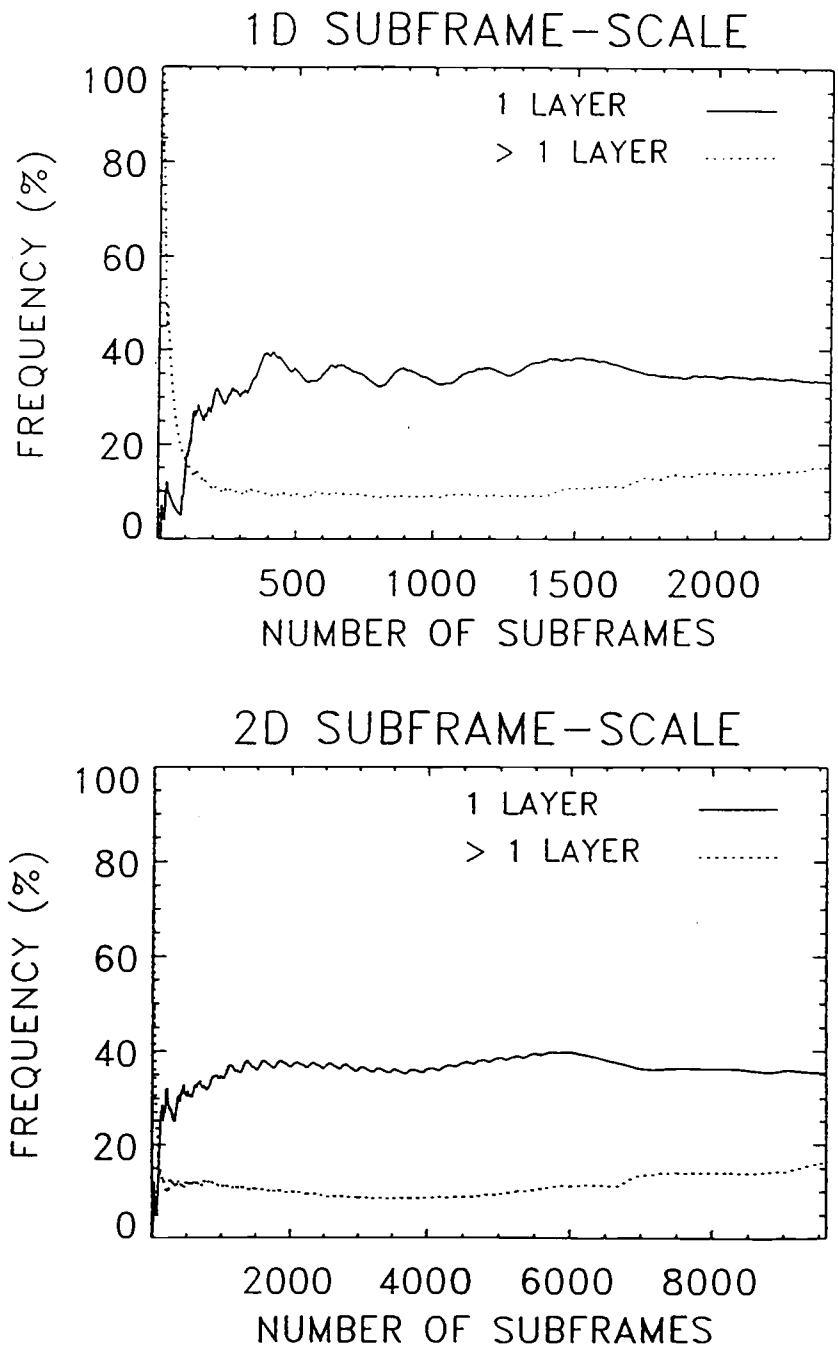

Figure 4.17 Occurrence frequencies of single and multi-layered cloud systems as a function of the number of subframes analyzed.

Chapter 5. Cloud Altitudes

5.1 Cloud Layer Altitudes Over Ocean

5.1.1 Pacific Ocean

Frequency distributions of AVHRR cloud-top altitudes for the Pacific Ocean are shown in Figure 5.1a and corresponding LITE cloud layer altitudes are shown in Figure 5.2a. Low-level layers below 4 km account for approximately 60% of both the LITE and AVHRR observations. Cloud altitudes for single-layered systems are shown in Figures 5.1b and 5.2b and show distributions similar to those for all cloud layers. AVHRR observations for the Pacific basin show the average single layer altitude to be 3.97 km. In the northern tropics, the average single-layer altitude is 7.20 km, within a range of 0.86 km to 16.31 km. This differs substantially from the southern tropical observations, with average layer altitude of 4.07 km and standard deviation of 3.50 km.

Figures 5.1c-d and 5.2c-d show cloud-top altitudes for the lower layers and the separation between layers for two-layered systems. For the AVHRR data, the average lower layer altitude is 2.33 km, while the corresponding LITE value is 3.35 km. AVHRR results indicate that mean upper-layer altitude values are higher in the northern hemisphere than in the southern, 9.13 km compared to 5.38 km, although the range of the layer altitudes is about the same. The overall distribution of cloud altitudes for the Pacific follows expectations: cloud altitudes tend to be highest in tropical regions where the troposphere is deepest, and to decrease gradually with latitude towards the poles.

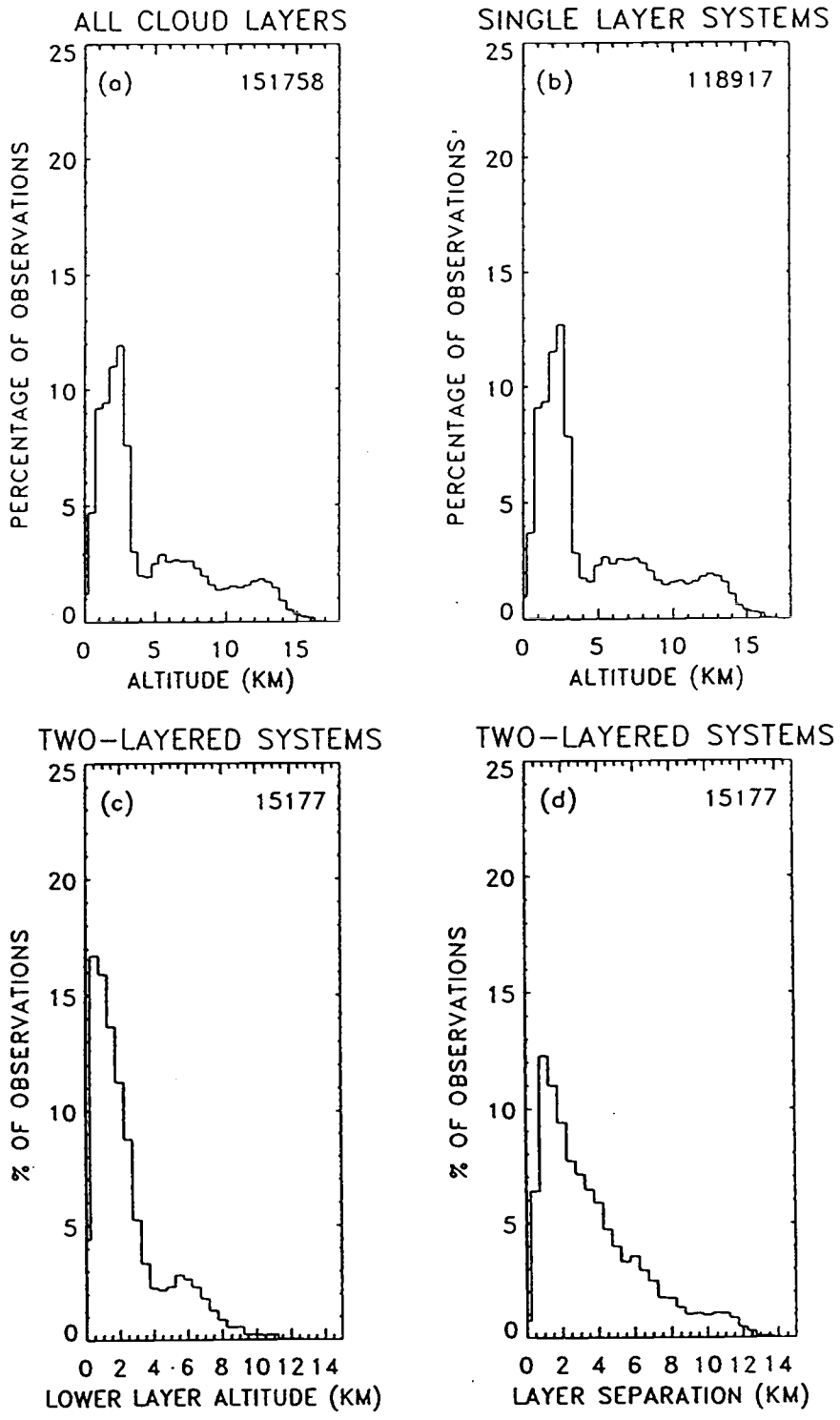

Figure 5.1 Frequency distributions of AVHRR cloud-top altitudes over the Pacific Ocean: (a) all cloud layers, (b) single-layered systems, (c) lower layer of two-layered cloud systems, (d) layer separations for two-layered systems.

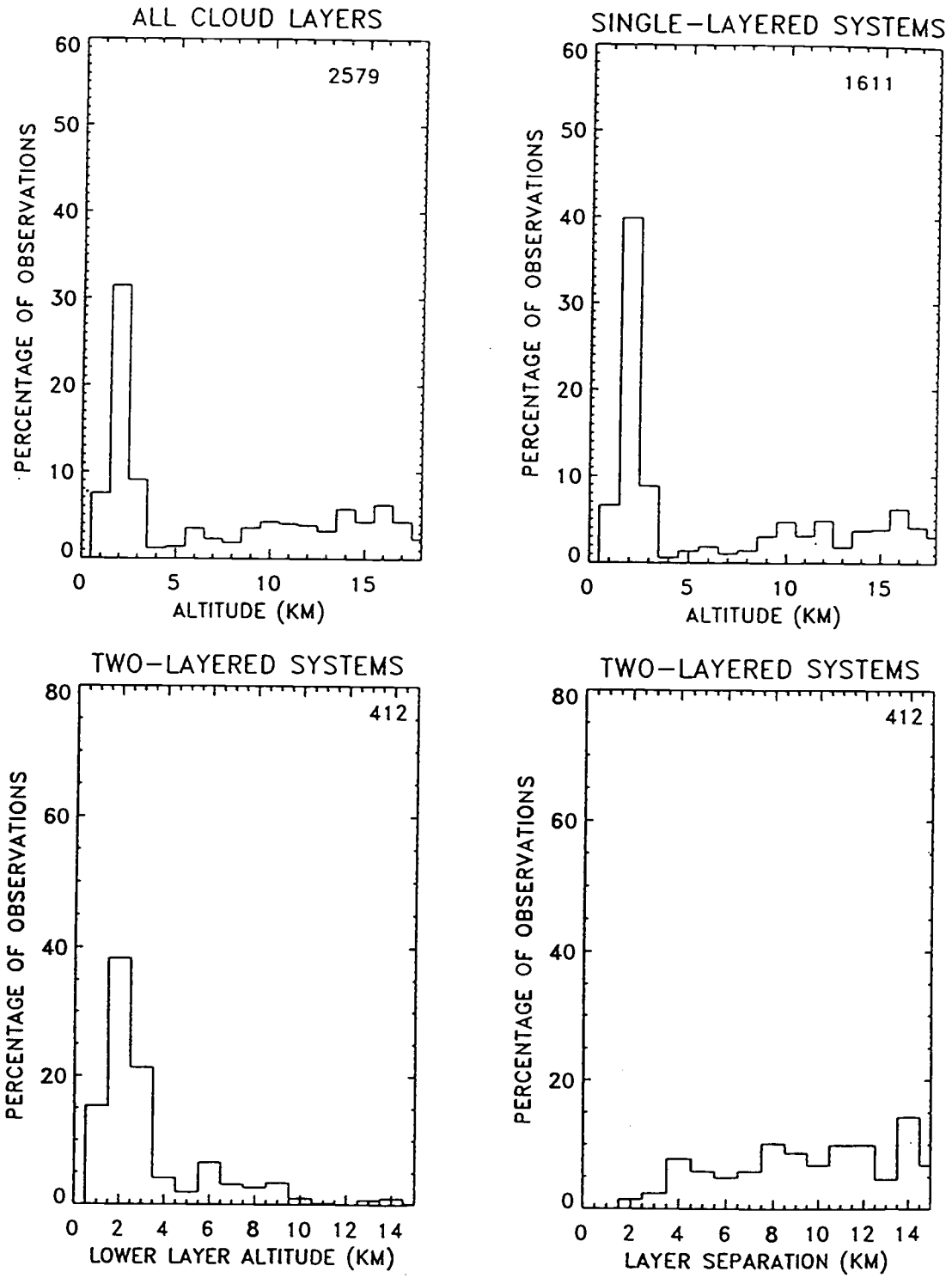

Figure 5.2 Frequency distributions of LITE cloud-top altitudes over the Pacific Ocean: (a) all cloud layers, (b) single-layered systems, (c) lower layer of two-layered cloud systems, (d) layer separations for two-layered systems.

Average layer separations for LITE two-layered systems are on the order of 9 km. For AVHRR the layer separations tend to fall in the 2 to 4 km range, although values of 9 to 10 km were observed for some cases. The larger layer separations for the lidar data are partly an artifact of the LITE processing, which prohibited detection of nearby peaks (see Appendix 1).

5.1.2 Atlantic Ocean

Frequency distributions of AVHRR cloud-top altitudes for the Atlantic Ocean are shown in Figure 5.3a. Low-level systems below 4 km account for 40-65% of the observations, and are found to be especially prevalent in the tropics and at northern latitudes. LITE cloud altitudes for the Atlantic Ocean are shown in Figure 5.4a. Similar to the AVHRR results, low-level systems account for the majority of observations over the region. Upper-level systems comprise a significant percentage of the northern hemisphere observations, with cloud layers distributed over a large altitude range. The limited amount of lidar data available for the southern ocean makes a wholly accurate representation of cloud layer altitudes difficult to attain.

Single layer altitudes are shown in Figure 5.3b and 5.4b. AVHRR results indicate an average cloud-top altitude of 4.06 km while the average value from LITE is 5.53 km. Frequency distributions of cloud-top altitudes for the lower layer and the separation between layers for two-layered systems are shown in Figures 5.3c-d and 5.4c.d. The

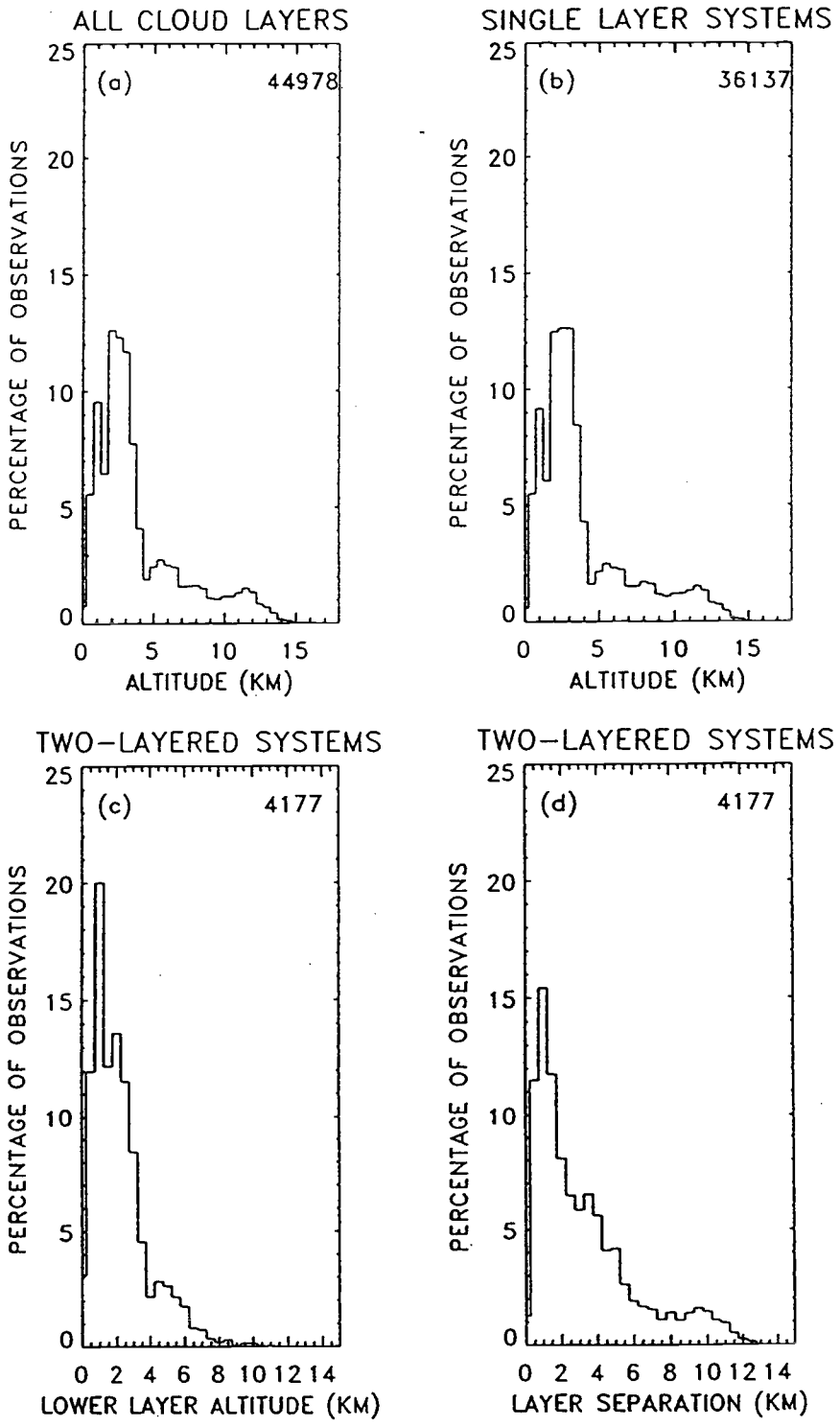

Figure 5.3 Frequency distributions of AVHRR cloud-top altitudes over the Atlantic Ocean: (a) all cloud layers, (b) single-layered systems, (c) lower layer of two-layered cloud systems, (d) layer separations for two-layered systems.

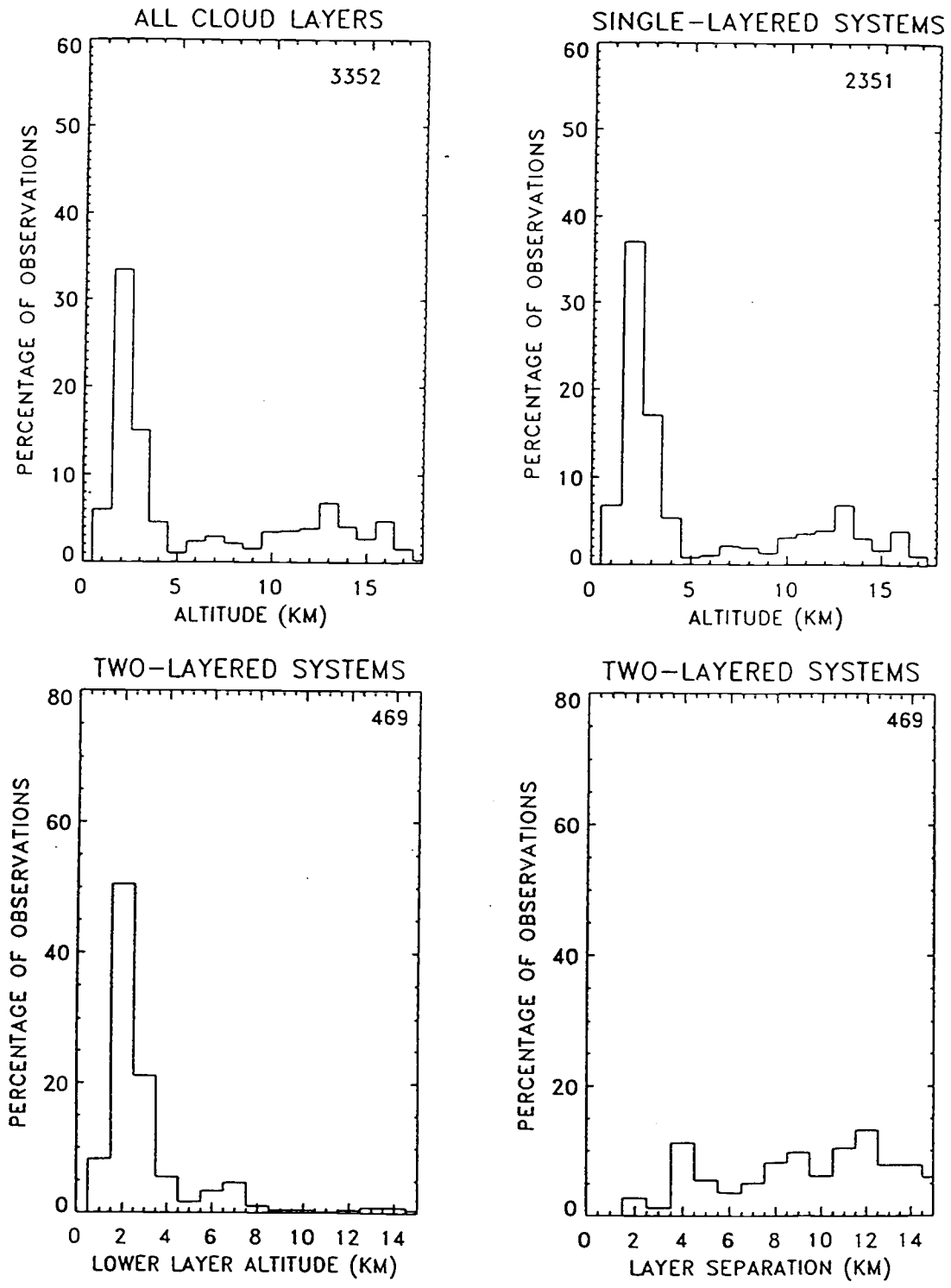

Figure 5.4 Frequency distributions of LITE cloud-top altitudes over the Atlantic Ocean: (a) all cloud layers, (b) single-layered systems, (c) lower layer of two-layered cloud systems, (d) layer separations for two-layered systems.

lower layer altitude averages are 2.29 km for AVHRR and 3.06 km for LITE. Average layer separations are much larger for the LITE data than for AVHRR, most likely due to lidar detection of thin cirrus missed by AVHRR or to LITE processing procedures (Appendix 1).

5.1.3 Indian Ocean

Figure 5.5a shows frequency distributions for AVHRR cloud-top altitudes for the Indian Ocean. Low-level systems comprise the majority of observations, except in the southern midlatitudes where layer altitudes were found to be fairly well-distributed over a range from 0 to 10 km. LITE cloud altitudes are shown in Figure 5.6a. Approximately 76% of the observations correspond to low-level layers below 4 km.

Single layer altitudes are shown in Figures 5.5a and 5.6a. For the AVHRR data, the average single layer altitude over the Indian Ocean is 4.03 km. The corresponding value for the LITE data is 5.73 km. The frequency distributions of lower layer altitudes and layer separations for two-layered cloud systems over the Indian Ocean are shown in Figures 5.5c-d and 5.6c-d. As seen for previous ocean regions, average AVHRR layer separations tend to be on the order of 2 to 5 km. In this case the higher values occur in the northern tropics. LITE layer separations are again much higher, averaging 10.86 km, and may result from the difference between cirrus and low- or mid-level stratus cloud, as compared to the altostratus and stratus layers typically detected by AVHRR. Such differences are again attributable to the LITE layer identification algorithm, which prevents small layer separations from occurring.

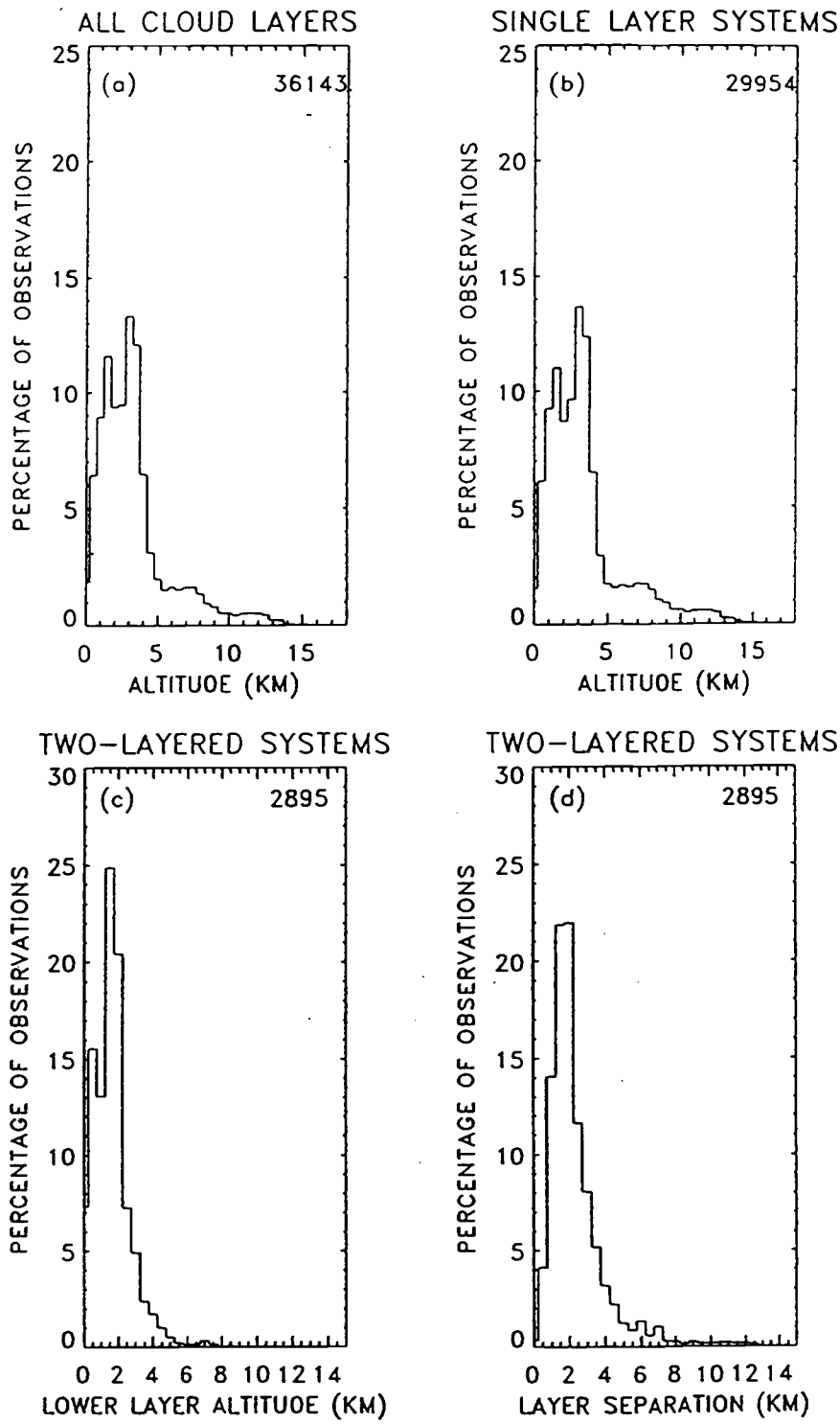

Figure 5.5 Frequency distributions of AVHRR cloud-top altitudes over the Indian Ocean: (a) all cloud layers, (b) single-layered systems, (c) lower layer of two-layered cloud systems, (d) layer separations for two-layered systems.

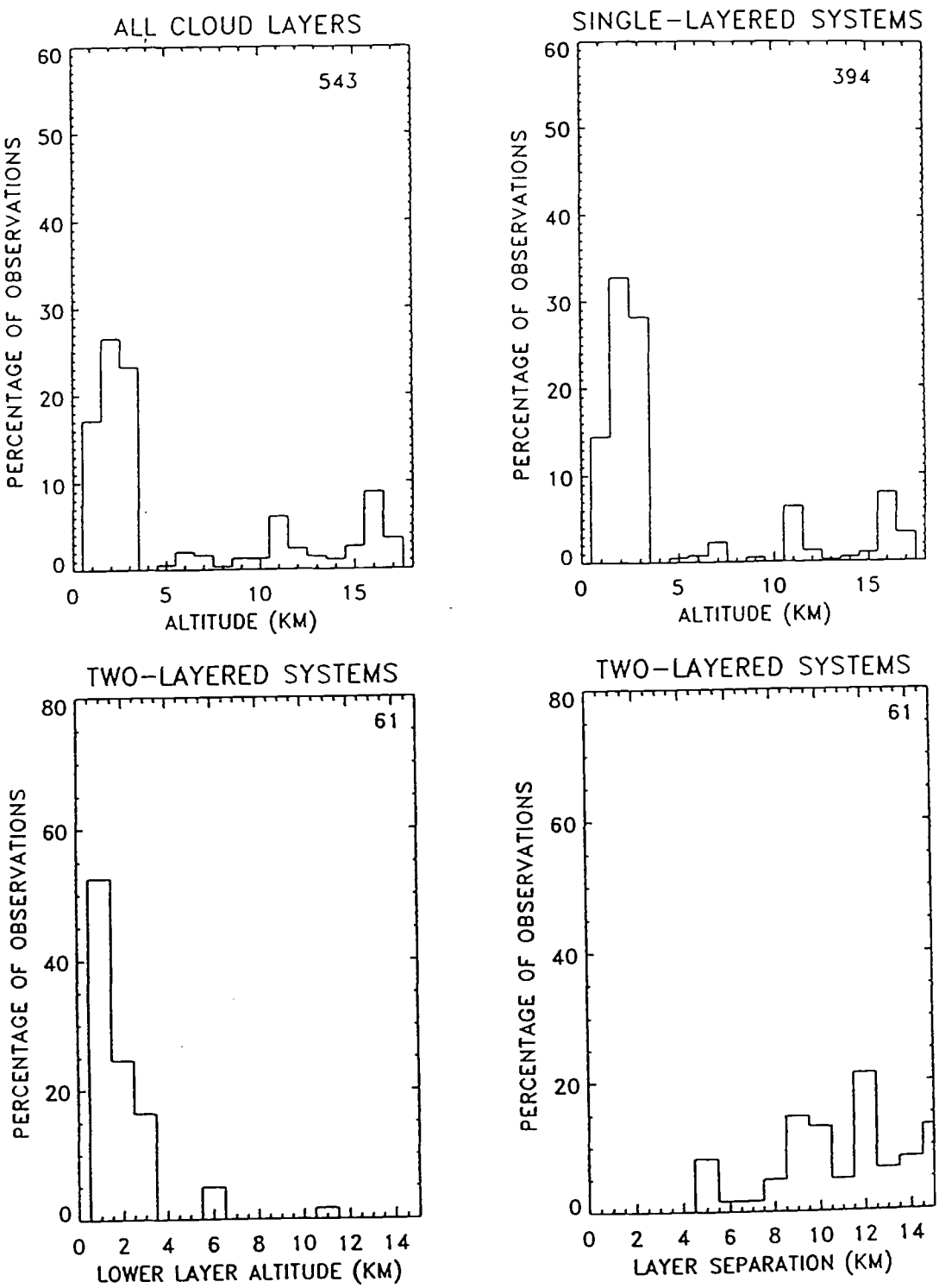

Figure 5.6 Frequency distributions of LITE cloud-top altitudes over the Indian Ocean: (a) all cloud layers, (b) single-layered systems, (c) lower layer of two-layered cloud systems, (d) layer separations for two-layered systems.

5.2 Cloud Layer Altitudes Over Land

Figures 5.7a and 5.8a show cloud-top altitudes for LITE and AVHRR observations over continents. Low-level systems (< 4 km) comprise approximately 65% of the AVHRR observations, with midlevel cloud between 5 and 9 km and upper-level cloud above 10 km also making significant contributions. The data show that 32% of the identified cloud layers have altitudes between 4 and 13 km, while only 3% of the layer altitudes are above 13 km. For the LITE data, approximately 36% of the identified cloud layers have cloud-top altitudes below 4 km. Mid- and upper-level systems can also clearly be seen in LITE data, with cloud layers between 4 and 13 km comprising about 41% of the observations and cloud altitudes above 13 km comprising 23% of the observations. Single layer altitudes, shown in Figures 5.7b and 5.8b exhibit similar distributions. For the AVHRR observations, the average single layer cloud-top altitude is 3.58 km, compared to an average value of 8.64 km for the LITE observations.

Lower layer altitudes and layer separations are shown in Figures 5.7c-d and 5.8c-d. The average LITE layer separation is 8.30 km, compared to an average separation of 5.40 km for two-layered systems identified by AVHRR. Eighty-five percent of the AVHRR lower layer altitudes are below 3.5 km. Lower layer altitudes for LITE are more uniformily distributed across the altitude range with an average value of 4.35 km over a range from 0.75 to approximately 16 km.

Cloud altitude statistics are summarized in Table 5.1. AVHRR results over land are similar to those over ocean, but show a lower percentage of upper-level systems than was detected by LITE, particularly over the world's continents. As indicated previously,

this is thought to be attributable to thin cirrus identified by LITE but missed using passive sensing techniques.

	Oceans		Land	
Altitude	AVHRR	LITE	AVHRR	LITE
≤ 4 km	64%	61%	65%	36%
4 – 13 km	33%	26%	32%	41%
≥ 13 km	3%	13%	3%	23%
TOTAL	232,879	6,474	73,017	3,287

Table 5.1 Distribution of cloud altitudes over the world's oceans and continents.

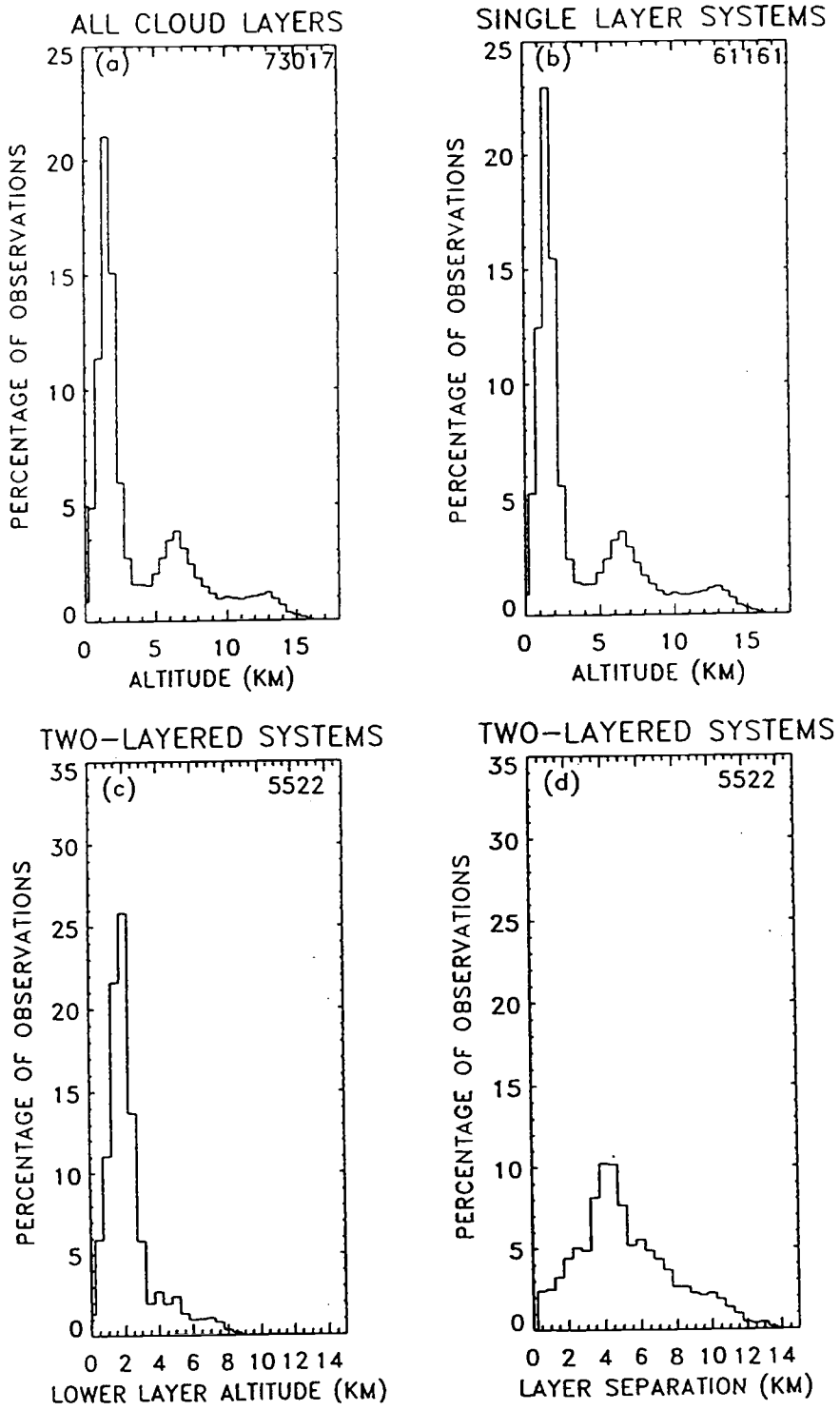

Figure 5.7 Frequency distributions of AVHRR cloud-top altitudes over the world's continents: (a) all cloud layers, (b) single-layered systems, (c) lower layer of two-layered cloud systems, (d) layer separations for two-layered systems.

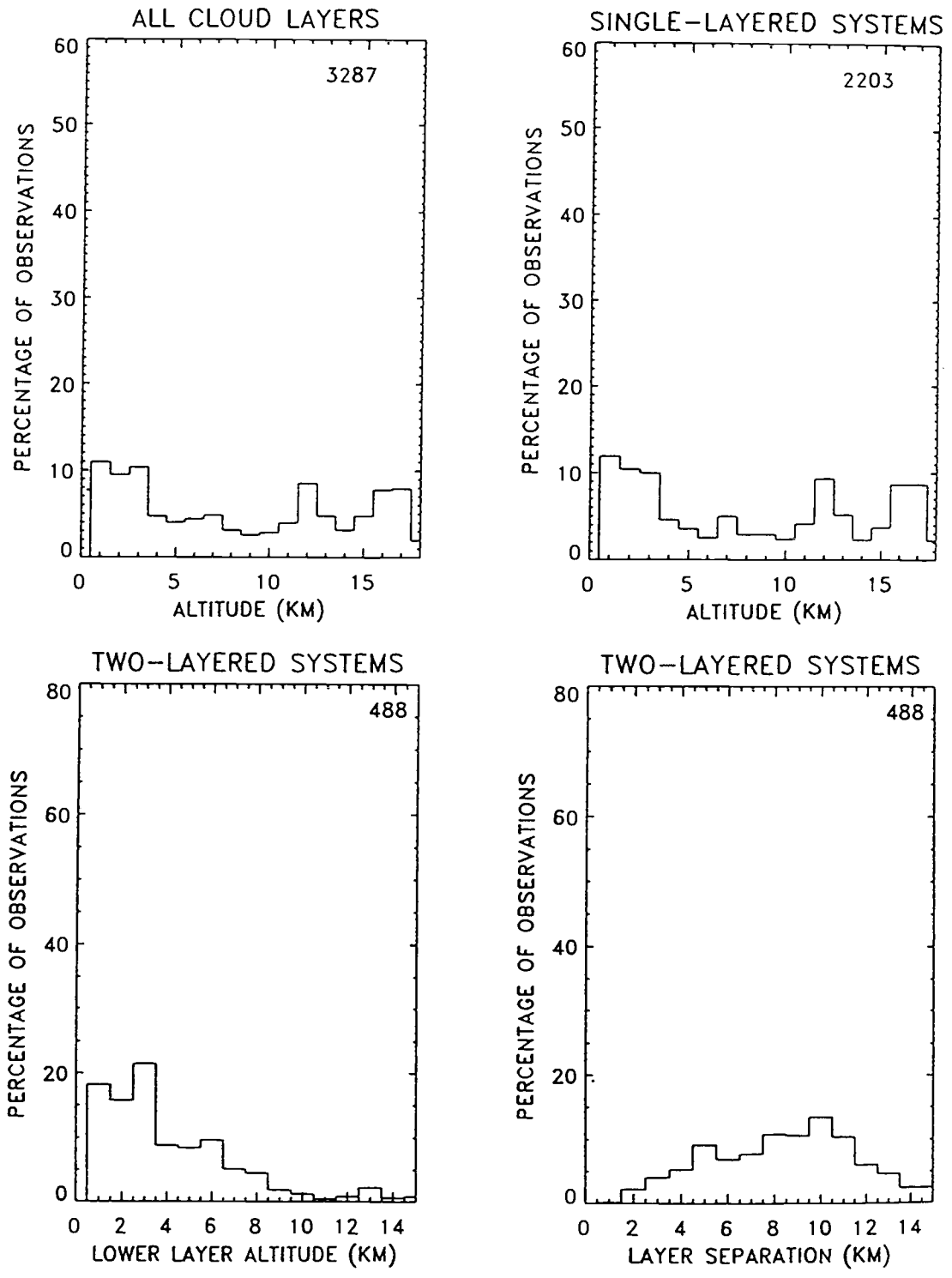

Figure 5.8 Frequency distributions of LITE cloud-top altitudes over the world's continents: (a) all cloud layers, (b) single-layered systems, (c) lower layer of two-layered cloud systems, (d) layer separations for two-layered systems.

Chapter 6. Summary and Conclusion

As shown in Chapter 4, regions that contain a single cloud layer or that are cloud-free account for about two-thirds of the 60-km scale observations for both LITE and AVHRR. Approximately 20 to 28% of the regions observed by satellite and lidar were found to contain more than one cloud layer, with slightly higher numbers of multilayered cloud occurrences for land than for ocean. At the 250-km scale, cloud-free and single-layered regions comprise about 50% of the total observations for LITE and 30% for AVHRR. Multilayered systems are seen in 40 to 45% of the LITE observations, and in about 60% of the AVHRR results. Again, multilayered systems were more often present over land than over ocean, with AVHRR occurrence frequencies of 70% and 50%, respectively. Multilayered systems are also more likely to be seen in the vicinity of the inter-tropical convergence zone and at midlatitudes. Differences in the AVHRR and LITE results can be attributed to the effects of one-dimensional versus two-dimensional sampling, and the ten-shot compositing of the LITE data. The sampling effects were discussed in Section 4.2 and suggest overall agreement between the LITE and AVHRR results for linear scales.

Strategies for further examination of LITE cloud observations would involve use of single-shot profiles rather than the ten-shot composities. Such an analysis may provide a more realistic assessment of cloud-free and overcast frequencies. Complete vertical profiles for each individual laser firing would also allow distinction between overlapping and non-overlapping cloud layers and allow more definitive calculation of the layer thicknesses and layer separations.

Cloud altitudes were examined in Chapter 5 and indicate that low-level layers comprise the majority of the observations. Over the world's oceans, both AVHRR and LITE results show 50 to 80% of the identified cloud layers residing at altitudes below 4 km. Both datasets indicate that low-level layers are especially prominent over the Indian Ocean, accounting for 70 to 80% of all observations and the upper-limit of the range above. The Pacific Ocean results mark the lower limit of this range, with about 50% of both the LITE and AVHRR observations corresponding to cloud layers below 4 km. Over land, cloud layers below 4 km account for about 50% of the AVHRR observations and 35% of those for LITE. Mid-level layers at altitudes between 6 and 9 km and upper-level layers above 10 km are seen to compose significant percentages of both the lidar and satellite results. The higher percentage of the LITE observations above 10 km suggests the effectiveness of lidar in detecting upper-level cirrus typically missed by passive sensing techniques.

Knowledge of the vertical distribution of clouds over the globe is essential for accurate understanding of the earth's radiation budget and overall climate. Human activities continue to change the composition of the atmosphere, increasing the potential for significant and planetwide changes in climate. Awareness of these changes and effects relies on global climate models and their ability to accurately account for the underlying feedbacks involved in the earth-atmosphere system. Clouds represent one such feedback, and currently present a difficult problem to climate modelers. Accurate treatment of clouds in general circulation models requires knowledge not only of cloud amount and height, but also information on cloud properties such as liquid/ice water path and particle size, shape, and phase. Cloud properties for the entire globe can be best obtained from

satellite observations, but current retrieval techniques are limited only to single-layered systems. The results suggest that these methods would fail for approximately 25% of 60-km regions.

It has been pointed out that the applicability of retrieval techniques to single layers only is necessitated by the lack of available measurements as compared to the large number of unknown quantities. As launches of Earth Observing System (EOS) satellites commence, new instruments with many more channels will provide increased information about earth and its atmosphere. One such instrument, the Moderate- resolution Imaging Spectroradiometer (MODIS), is scheduled for launch aboard the EOS-AM and -PM satellites beginning in 1998 and will measure radiances in 36 spectral bands from 0.405 to 14.385 μm. Also scheduled for imminent launch is the CERES (Clouds and Earth's Radiant Energy System) instrument, measuring both reflected and emitted radiation for the determination of the earth's radiation budget.

As demonstrated by LITE, active sensing does have its place among space-borne techniques. Lidar measurements are an excellent source of information for cloud-top and cloud-base altitudes and cloud porosities or transmissivities. Coupled with the global coverage provided by satellite orbit, lidar can provide high resolution vertical profiles of the atmosphere and some of its constituents, including clouds and aerosols. This information is useful on its own or in combination with radiance measurements from a passive imager on the same platform.

Determination of cloud distribution and cloud properties from remote observations depend on robust satellite retrieval algorithms and the availability of large, multispectral datasets. In this study, spatial coherence results are compared with those from a space-

borne lidar instrument to illustrate the effectiveness of this technique for multilayer cloud detection. For scenes containing multiple cloud layers, retrieval of cloud droplet size, phase, and other optical properties presents a challenge which remains to be solved.

Bibliography

Arking A. and J. D. Childs, 1985: Retrieval of cloud cover parameters from multispectral satellite images. J Clim Appl Meteor 24:322-333.

Baum, B.A., R.F. Arduini, B.A. Wielicki, P. Minnis, and S-C. Tsay, 1994: Multilevel cloud retrieval using multispectral HIRS and AVHRR data: nighttime oceanic analysis. J Geophys Res 99(D3):5499-5514.

------ and B.A. Wielicki, 1994: Cirrus cloud retrieval using infrared sounder data: multilevel cloud errors. J Appl Meteor 33:107-117.

Cess, R.D. and others, 1989: Interpretation of cloud-climate feedback as produced by 14 atmospheric general circulation models. Science 245:513-516.

Coakley, J.A., Jr. and F.P. Bretherton, 1982: Cloud cover from high resolution scanner data: detecting and allowing for partially filled fields of view. J Geophys Res 87(C7):4917-4932.

------, 1983: Properties of multi-layered cloud systems from satellite imagery. J Geophys Res 88(C15):10818-10828.

------ and D.G. Baldwin, 1984: Toward the objective analysis of satellite imagery data. J Climate Appl Meteor 23:1065-1099.

Hahn, C.J., S.G. Warren, and J. London, 1982: Atlas of simultaneous occurrence of different cloud types over the ocean. NCAR Tech. Note, NCAR/TN-201+STR.

-------,------,------, R.M. Chervin, and R. Jenne, 1984: Atlas of simultaneous occurrence of different cloud types over land. NCAR Tech. Note, NCAR/TN-241+STR.

Hartmann, D.L., M.E. Ockert-Bell, and M.L. Michelson, 1992: The effect of cloud type on the earth's energy balance: global analysis. J Clim 5(11):1281-1304.

Hughes, N.A., 1984: Global cloud climatologies: a historical review. J Climate Appl Meteor 23:724-751.

Jin Y. and W.B. Rossow, 1997: Detection of cirrus overlapping low-level clouds. J Geophys Res 102(D2):1727-1737.

Kidder S.Q. and T. H. Vonder Haar, 1995: Satellite Meteorology: An Introduction, Academic Press, San Diego, CA.

Kiehl, J.T. and K.E. Trenberth, 1997: Earth's annual global mean energy budget. Bull Amer Meteor Soc 78(2):197-208.

Liou, K-N., 1980: An Introduction to Atmospheric Radiation, Academic Press, San Diego, CA.

McCormick, M.P., D.M. Winker, E.V. Browell, J. A. Coakley, C.S. Gardner, R.M. Hoff, G.S. Kent, S.H. Melfi, R.T. Menzies, C.M.R. Platt, D.A. Randall, and J.A. Reagan, 1993: Scientific investigations planned for the Lidar In-space Technology Experiment (LITE). Bull Amer Meteor Soc 74(2):205-214.

Platt, C.M.R., S.A. Young, G.R. Patterson, and P.J. Manson, 1993: Lidar and radiometer observations of midlevel clouds. Optical Remote Sensing of the Atmosphere Technical Digest 5:114-117.

Ramanathan, V., R.D. Cess, E.F. Harrison, P. Minnis, B.R. Barkstrom, E. Ahmad, and D. Hartmann, 1989: Cloud-radiative forcing and climate: results from the Earth Radiation Budget Experiment. Science 243:57-63.

Reynolds D.W. and T. H. Vonder Haar, 1977: A bispectral method for cloud parameter determination. Monthly Weather Review 105:446-457.

Rossow, W.B. and R.A. Schiffer, 1991: ISCCP cloud data products. Bull Amer Meteor Soc 72(1):2-20.

Schwalb, A., 1978: The TIROS-N / NOAA A-G satellite series. NOAA Tech Mem, NESS 95.

Slingo, A., R.C. Wilderspin, and R.N.B. Smith, 1989: Effect of improved physical parameterizations of cloudiness and the earth's radiation budget. J Geophys Res 94(D2):2281-2301.

Smith, L.D. and T.H. Vonder Haar, 1991: Clouds-radiation interactions in a general circulation model: impact upon the planetary radiation balance. J Geophys Res 96(D1):893-914.

Smith, R.N.B., 1990: A scheme for predicting layer clouds and their water content in general circulation model. Quart J Roy Meteor Soc 116:435-460.

Stone, R.S., G.L. Stephens, C.M.R. Platt, and S. Banks, 1990: The remote sensing of thin cirrus using satellites, lidar and radiative transfer theory. J Appl Meteor 29:353-366.

Tian, L. and J.A. Curry, 1989: Cloud overlap statistics. J Geophys Res 94(D7):9925-9935.

Wang, J. and W.B. Rossow, 1995: Determination of vertical cloud structure from upper-air observations. J Appl Meteor 34:2243-2258.

Warren, S.G., C.J. Hahn, J. London, R.M. Chervin, and R. Jenne, 1988: Global distribution of total cloud cover and cloud amounts over the ocean. NCAR Tech. Note, NCAR/TN-317+STR.

Winker, D.M., R.H. Couch, and M.P. McCormick, 1996: An overview of LITE: NASA's Lidar In-space Technology Experiment. Proc IEEE 84(2):164-180.

APPENDICES

Appendix 1: Algorithm Testing

The method used in the analysis of the lidar data to identify significant peaks in a one-dimensional distribution was tested on simulations of a normally distributed input signal overlying uniformly distributed random noise. A total of 1,600 simulations were performed, varying both the signal-to-noise ratios and the standard deviation of the input signal. The simulations were performed using 100 observations over a domain from 0 to 18. A total of 10 different noise levels, from 0.01 to 1, and 4 standard deviations, from 0.1 to 2.2 were used for the simulated data.

Simulation results are tabulated below and indicate that overall a significant peak was identified for 63.2% of the cases for which an input signal was put in, and in only 7.5% of cases was a peak identified when no signal was input.

		IN		
		Layer	No Layer	Total
OUT	Layer	**910** (a_{11})	**12** (a_{12})	**922**
	No Layer	**530** (a_{21})	**148** (a_{22})	**678**
	Total	**1440**	**160**	

Matrices similar to the one above were obtained by running 40 simulations for each of the 10 noise levels at each of the four standard deviations. From these values, the accuracy is computed, given by

$$Acc = \frac{a_{11} + a_{22}}{N},$$

where N is the number of simulations. The results are shown in Figure A.1 and indicate that when the standard deviation of the input signal is small (0.1 or 0.8), 100% accuracy can be expected for layer fractions of 25-30%. For larger signal standard deviations, an input layer fraction of about 40% is sufficient to attain accuracies greater than 80%.

Figure A.2 shows the fraction of points identified as belonging to a significant peak compared to the number of points expected based on the characteristics of the input signal. For a normal distribution, approximately 95% of the points fall within 2 standard deviations of the mean. The number of points in this range is given by

$$q = 0.95m + \frac{4\sigma}{L}n,$$

where m is the number of normally distributed points, n is the number of random points, and L is the domain of the distribution. When both the simulated layer fraction and the signal standard deviation are small, there is a tendency to overestimate the number of points belonging to the peak. This tendency decreases as the simulated layer fraction is increased. For large signal standard deviations, the number of points belonging to the peak is less than that expected from the input signal, especially for input layer fractions on the order of 50%.

Figure A.3 shows frequency distributions of the noise percentages and layer standard deviations associated with each 1000-km orbital segment in the Atlantic Ocean. The noise percentage tends to be less than 5% and the layer standard deviation below 0.5, well within the range where the accuracy of the algorithm is expected to be very high.

The analysis of cloud layer altitudes discussed in Chapter 5 indicates that small layer separations (< 2 km) were not observed in the LITE data. This was surmised to be

an artifact of the peak finding algorithm used in the layer identification. Figure A.4 shows results of simulations in which two separate Guassian signals were overlaid on uniform random noise. For layer separations less than 2 km, the two separate signals were identified only about 20% of the time. For layer separations on the order of 4 km or greater, identification of both signals was achieved in nearly all the simulations. The dependence of the results on the standard deviation of the input signals and the fraction of input noise are also shown in Figure A.4 and are found to be minor compared to the layer separation dependence.

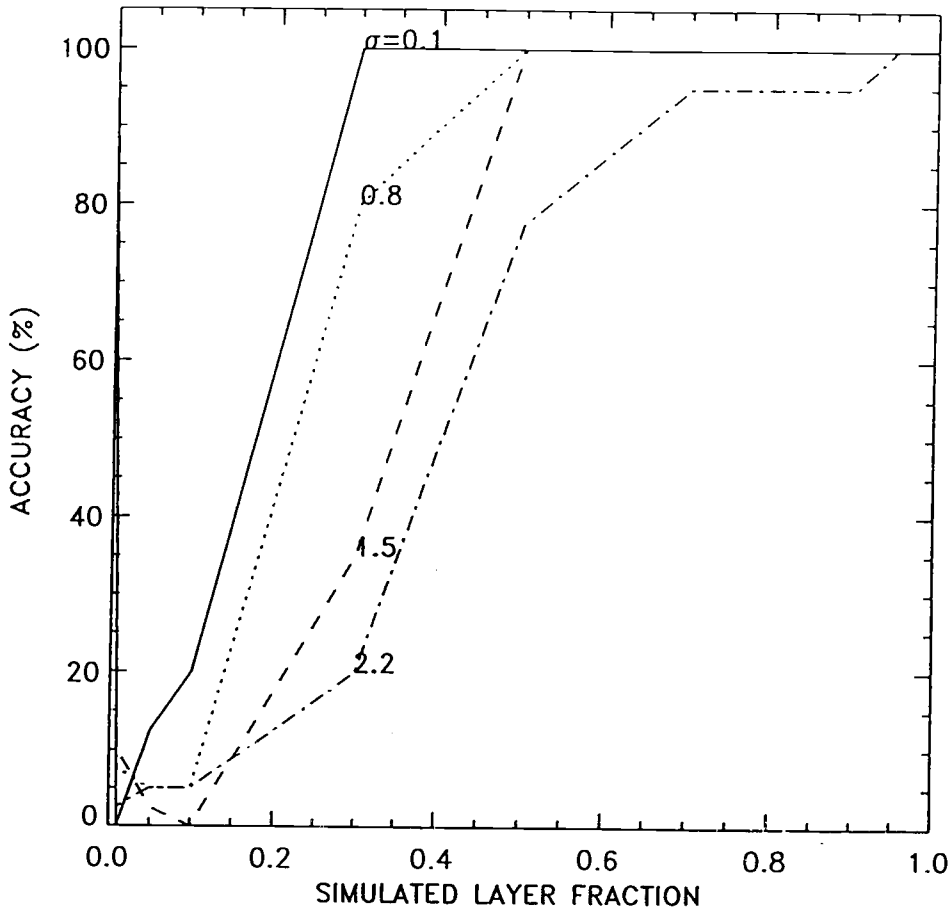

Figure A.1 Accuracies of signal identification algorithm as a function of simulated layer fraction and signal standard deviation.

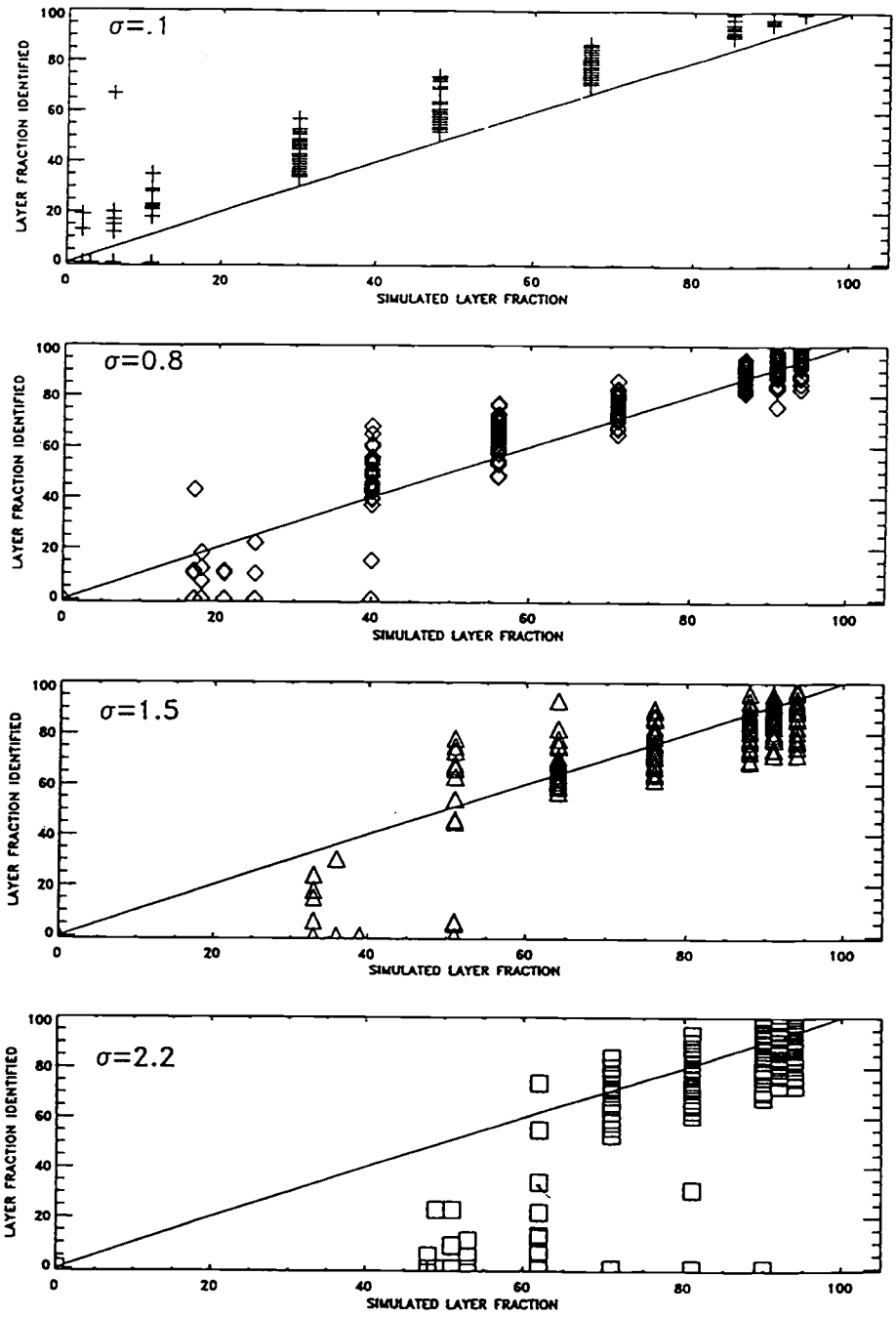

Figure A.2 Layer fraction identified by algorithm versus simulated layer fraction: (a) $\sigma = 0.1$, (b) $\sigma = 0.8$, (c) $\sigma = 1.5$, (d) $\sigma = 2.2$.

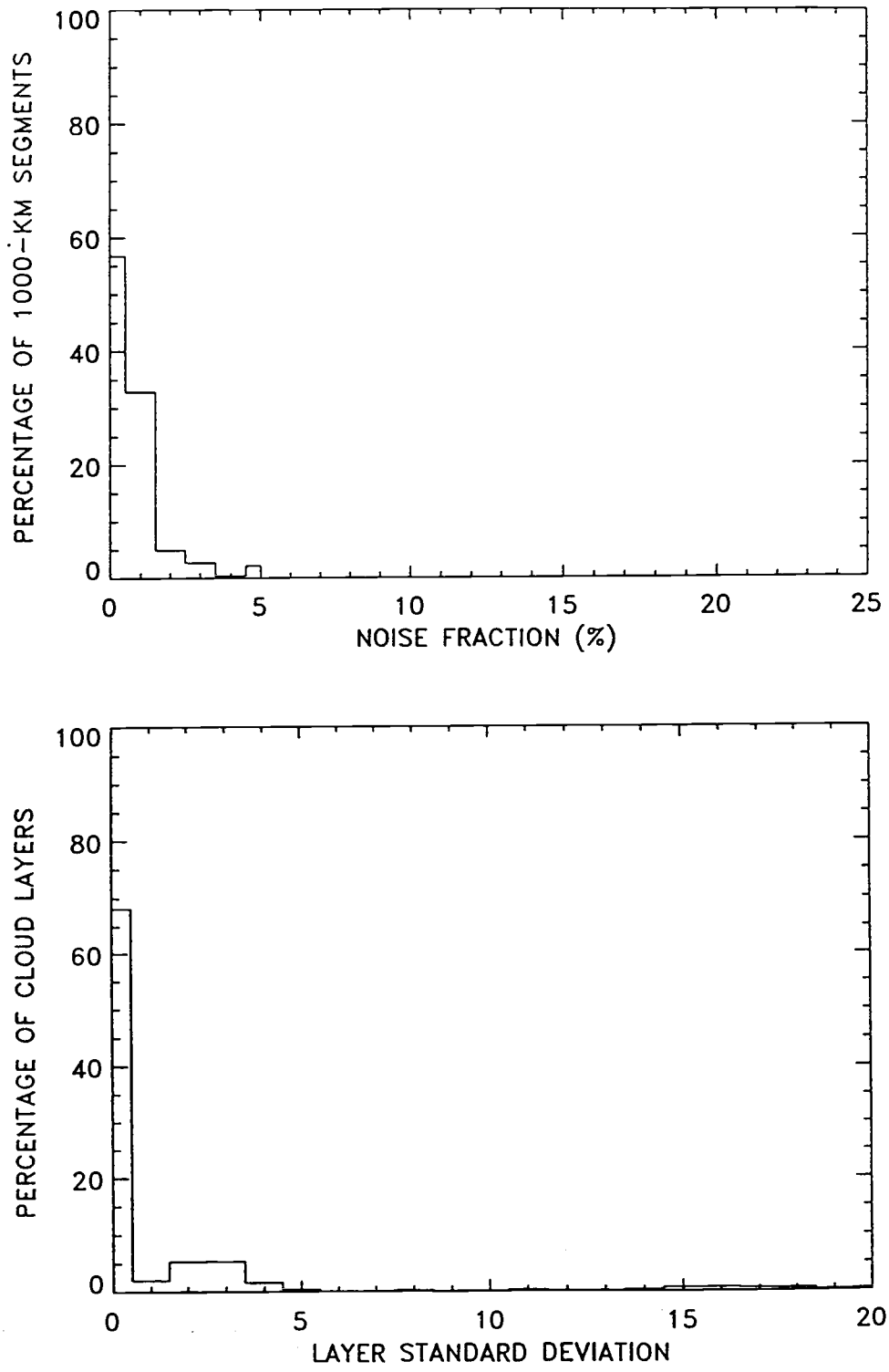

Figure A.3 Frequency distributions of (a) noise fractions and (b) standard deviations for LITE observations along 1000-km orbit segments over the Atlantic Ocean.

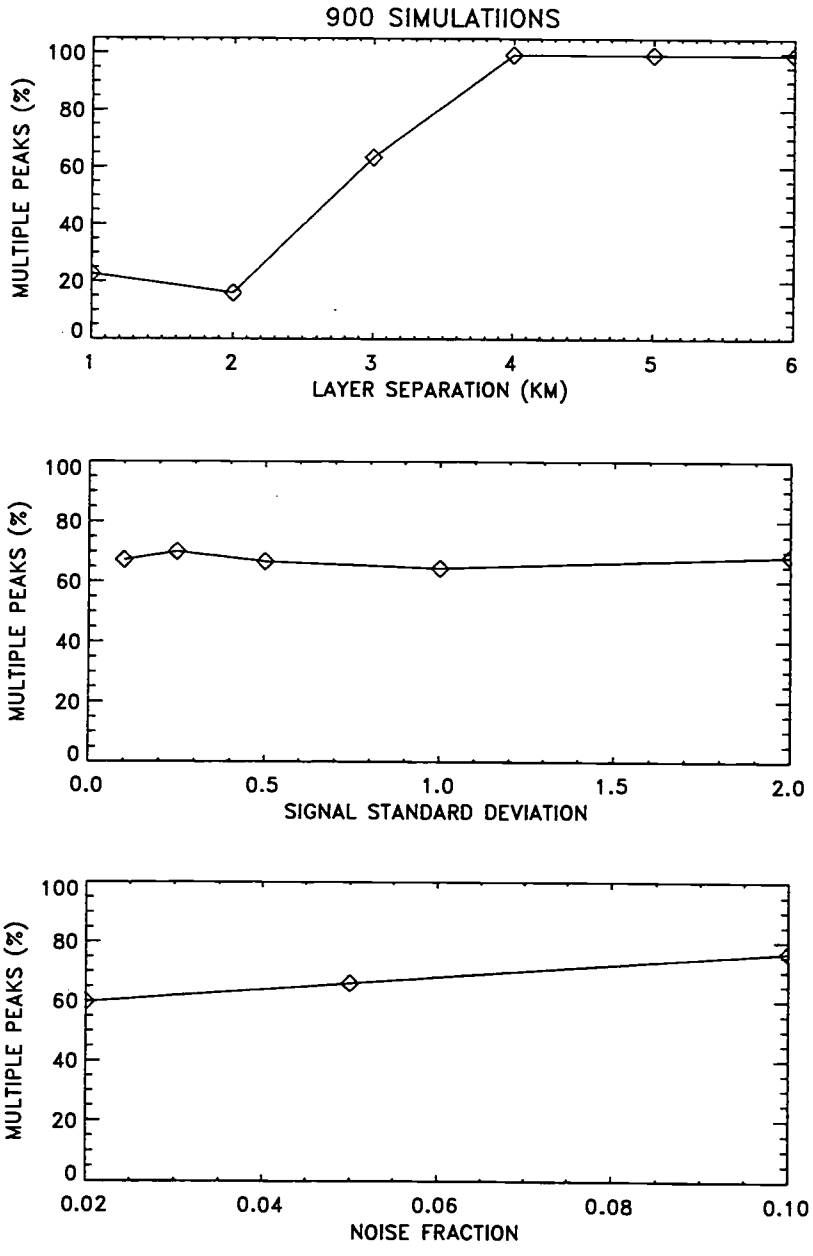

Figure A.4 Percentage of simulations for which multiple peaks were identified as a function of (a) layer separation, (b) signal standard deviation, and (c) noise fraction.

Appendix 2: Cloud Layer Statistics

60 km	PACIFIC		ATLANTIC		INDIAN	
	LITE	AVHRR	LITE	AVHRR	LITE	AVHRR
Cloud-free	2	21	2	20	3	45
Overcast	45	12	32	11	46	5
Single layer	67	35	72	38	72	32
1 layer plus other	6	11	7	13	9	14
2 distinct layers	18	1	14	1	10	1
2 layers plus other	1	5	1	5	21	5
3 distinct layers	2	0	1	0	0	0
3 layers plus other	0	0	0	0	3	0
No identified layers	4	27	3	24	2	4

Table A.1 Occurrence frequencies (%) for Pacific, Atlantic, and Indian Oceans: 60-km scale.

250 km	PACIFIC			ATLANTIC			INDIAN	
	LITE	AVHRR		LITE	AVHRR		LITE	AVHRR
Cloud-free	1	6		0	6		3	14
Overcast	38	5		27	2		37	1
Single layer	51	30		58	21		64	30
1 layer plus other	5	21		4	34		3	29
2 distinct layers	30	3		32	1		24	0
2 layers plus other	1	19		0	24		0	21
3 distinct layers	10	0		3	0		7	0
3 layers plus other	0	5		1	6		0	3
No identified layers	3	17		1	7		0	3

Table A.2 Occurrence frequencies (%) for Pacific, Atlantic, and Indian Oceans: 250-km scale.

60 km	N & S America		Africa/Europe		Asia	
	LITE	AVHRR	LITE	AVHRR	LITE	AVHRR
Cloud-free	13	45	12	40	11	44
Overcast	25	6	26	5	65	8
Single layer	52	25	58	33	54	29
1 layer plus other	14	18	10	22	20	20
2 distinct layers	13	0	12	0	8	0
2 layers plus other	2	5	2	4	3	5
3 distinct layers	1	0	1	0	1	0
3 layers plus other	0	0	0	0	0	0
No identified layers	4	1	5	1	4	2

Table A.3 Occurrence frequencies (%) for major continental regions: 60-km scale.

250 km	N & S America		Africa/Europe		Asia	
	LITE	AVHRR	LITE	AVHRR	LITE	AVHRR
Cloud-free	8	20	7	15	6	18
Overcast	21	1	18	0	50	0
Single layer	48	13	46	15	48	10
1 layer plus other	6	38	7	41	10	45
2 distinct layers	29	0	32	0	28	0
2 layers plus other	2	22	1	22	2	20
3 distinct layers	7	0	4	0	4	0
3 layers plus other	0	4	0	7	0	5
No identified layers	1	0	3	1	2	1

Table A.4 Occurrence frequencies (%) for major continental regions: 250-km scale.